

*(Handwritten: P2)*

DNA 3923T

# DEVELOPMENT AND TESTING OF DAVID: A CLOSE-IN EMP COUPLING CODE FOR ARBITRARILY SHAPED OBJECTS

Mission Research Corporation  
735 State Street  
Santa Barbara, California 93101

7 November 1975

Topical Report for Period 1 February 1975—1 October 1975

CONTRACT No. DNA 001-75-C-0094

APPROVED FOR PUBLIC RELEASE;  
DISTRIBUTION UNLIMITED.

THIS WORK SPONSORED BY THE DEFENSE NUCLEAR AGENCY  
UNDER RDT&E RMSS CODE D323075464 R99QAXEB08853 H2590D.

*(Handwritten: J.C.)*  
D D C  
RECEIVED  
OCT 18 1975  
REGULATORY

Prepared for

Director

DEFENSE NUCLEAR AGENCY

Washington, D. C. 20305

DESTROY THIS REPORT WHEN IT IS NO LONGER  
NEEDED. DO NOT RETURN TO SENDER.



UNCLASSIFIED

SECURITY CLASSIFICATION OF THIS PAGE (When Data Entered)

19 REPORT DOCUMENTATION PAGE		READ INSTRUCTIONS BEFORE COMPLETING FORM	
1. REPORT NUMBER DNA 3923T	2. GOVT ACCESSION NO.	3. RECIPIENT'S CATALOG NUMBER	
4. TITLE (and Subtitle) DEVELOPMENT AND TESTING OF DAVID: A CLOSE-IN EMP COUPLING CODE FOR ARBITRARILY SHAPED OBJECTS.		5. TYPE OF REPORT AND PERIOD COVERED Topical Report for Period 1 Feb 75 - 1 Oct 75	
7. AUTHOR(s) Michael A. Messier, Kenneth S. Smith Robert M. Hamilton		6. PERFORMING ORG. REPORT NUMBER MRC-R-228	
9. PERFORMING ORGANIZATION NAME AND ADDRESS Mission Research Corporation 735 State Street Santa Barbara, California 93101		10. PROGRAM ELEMENT, PROJECT, TASK AREA & WORK UNIT NUMBERS Subtask R99QAXEB088-53	
11. CONTROLLING OFFICE NAME AND ADDRESS Director Defense Nuclear Agency Washington, D.C. 20305		12. REPORT DATE 7 Nov 1975	
14. MONITORING AGENCY NAME & ADDRESS (if different from Controlling Office) DNA-NWED-QAXE		13. NUMBER OF PAGES 138	
16. DISTRIBUTION STATEMENT (of this Report) Approved for public release; distribution unlimited. B088		15. SECURITY CLASS (of this report) UNCLASSIFIED	
17. DISTRIBUTION STATEMENT (of the abstract entered in Block 20, if different from Report)		15a. DECLASSIFICATION/DOWNGRADING SCHEDULE	
18. SUPPLEMENTARY NOTES This work sponsored by the Defense Nuclear Agency under RDT&E RMSS Code B323075464 R99QAXEB08853 H2590D.			
19. KEY WORDS (Continue on reverse side if necessary and identify by block number) Electromagnetic Pulse Computer Code Development Close-in EMP Analysis 3-D Numerical Techniques			
20. ABSTRACT (Continue on reverse side if necessary and identify by block number) This report describes the development and testing of a 3-D, finite difference computer code used to estimate the currents and voltages induced on an arbitrarily shaped object when illuminated by a plane wave gamma source. The application of the code is for performing calculations to aid in the prediction of close-in EMP effects on systems. Included is a descrip- tion of the way the physics of the problem is handled by the code, the methods used to obtain numerical solutions, the results of comparison tests and conclusions and recommendations.			

DD FORM 1473 1 JAN 73 EDITION OF 1 NOV 65 IS OBSOLETE

UNCLASSIFIED

SECURITY CLASSIFICATION OF THIS PAGE (When Data Entered)

406 548 LB

## CONTENTS

ACCESS	
NTIS	<input checked="" type="checkbox"/>
DOC	<input type="checkbox"/>
UNAVAIL	<input type="checkbox"/>
JUSTIFICATION	
BY	
DISTRIBUTION/AVAILABILITY	
Dist.	

**A**

	PAGE
ILLUSTRATIONS	2
TABLES	8
SECTION 1—INTRODUCTION	9
SECTION 2—PROBLEM PHYSICS	11
2.1 CLOSE-IN PHENOMENA	11
2.2 FIELD EQUATIONS	15
2.3 MOMENTUM EQUATIONS	17
2.4 SELF-CONSISTENT (PARTICLE) SOURCES	18
2.5 PRESCRIBED (ANALYTICAL) SOURCES	21
2.6 THE PHOTON FLUX	25
2.7 AIR CHEMISTRY	28
SECTION 3—THE NUMERICAL SOLUTION	33
3.1 OVERVIEW AND PROBLEM GEOMETRY	33
3.2 FIELD EQUATIONS	41
3.3 MOMENTUM EQUATIONS AND AVERAGING TECHNIQUE	49
3.4 AIR CHEMISTRY EQUATIONS	58
SECTION 4—NUMERICAL RESULTS	62
4.1 EX STUDY	62
4.2 GLANC/DAVID COMPARISON	73
4.3 POLE STUDY	86
SECTION 5—CONCLUSIONS AND RECOMMENDATIONS	115
REFERENCES	120
APPENDIX A—AN APPROXIMATION FOR INCLUDING MAGNETIC TURNING EFFECTS IN PRESCRIBED ELECTRON CURRENTS	121
REFERENCES	134

## ILLUSTRATIONS

FIGURE		PAGE
1	Example problem geometry.	12
2	Plot of ratios useful in calculating prescribed currents and ionization rates. Curve-fits are layed over data points.	24
3	Qualitative plot of the $\dot{\gamma}$ time history used in program DAVID.	27
4	a. Electron attachment and avalanche coefficients for dry air.	30
4	b. Electron mobility in dry air.	31
5	General flow pattern of programs DAVID and DAVEJR.	34
6	Coordinate system used in program DAVID. Note the separate coordinate system used below the ground plane.	35
7	Arrangement of cells within a cross section of the calculational volume. The pattern is repeated in the x-direction (out of the page). Note the location of the extra layers of cells, including a layer of air cells below the air/soil interface. The cell numbering system is also shown in two dimensions. A third digit is also used to represent the x-coordinate.	36
8	Unit cell used in program DAVID. Sides are numbered to illustrate the grid boundary numbering system.	37
9	Flow chart of the calculation of electric fields in the air as performed by subroutine fields.	47
10	Flow chart showing the particle motion and current/ionization rate calculation.	50

FIGURE		PAGE
11	Comparison between current distribution calculated with particles and ideal distribution in direction parallel to ground and flux. Time is during rise of pulse. Magnitude of "ideal" distribution is normalized.	57
12	Geometry used in EX study (only cells near boundary are shown).	63
13	a. Approximate contours of constant $E_x$ at $T = 5.0E-9$ sec. (Ambient boundary condition, $\theta = 0^\circ$ , $Y = Y_{MAX}$ ).	65
13	b. Approximate contours of constant $E_x$ at $T = 5.8E-9$ sec. (Ambient boundary condition, $\theta = 0^\circ$ , $Y = Y_{MAX}$ ).	65
13	c. Approximate contours of constant $E_x$ at $T = 9.8E-9$ sec. (Ambient boundary condition, $\theta = 0^\circ$ , $Y = Y_{MAX}$ ).	66
13	d. Approximate contours of constant $E_x$ at $T = 2.9E-8$ sec. (Ambient boundary condition, $\theta = 0^\circ$ , $Y = Y_{MAX}$ ).	66
14	a. Approximate contours of constant $E_x$ at $T = 9.8E-9$ sec. (Ambient boundary condition, $\theta = 20^\circ$ , $Y = Y_{MAX}$ ).	68
14	b. Approximate contours of constant $E_x$ at $T = 2.90E-8$ sec. (Ambient boundary condition, $\theta = 20^\circ$ , $Y = Y_{MAX}$ ).	68
15	a. Approximate contours of constant $E_x$ at $T = 9.8E-9$ sec. (Ambient boundary with shadow, $\theta = 20^\circ$ , $Y = Y_{MAX}$ ).	69
15	b. Approximate contours of constant $E_x$ at $T = 2.9E-8$ sec. (Ambient boundary, with shadow, $\theta = 20^\circ$ , $Y = Y_{MAX}$ ).	69
16	a. Approximate contours of constant $E_x$ at $T = 9.8E-9$ sec. (Perfect conductor boundary condition, $\theta = 20^\circ$ , $Y = Y_{MAX}$ ).	70
16	b. Approximate contours of constant $E_x$ at $T = 2.90E-8$ sec. (Perfect conductor boundary condition, $\theta = 20^\circ$ , $Y = Y_{MAX}$ ).	70

FIGURE		PAGE
17	Variation of HX in the vicinity of the pole, comparing the field seen with the ambient boundary condition and the perfectly conducting boundary condition. The variation is along a line 0.1m above the ground and passing through the pole in the z-direction.	71
18	a. Approximate contours of constant $E_x$ at $T = 9.8E-9$ sec. (Ambient boundary condition, $\theta = 20^\circ$ , $Y = Y_{MAX}$ , <u>no pole</u> ).	72
18	b. Approximate contours of constant $E_x$ at $T = 2.9E-8$ sec. (Ambient boundary condition, $\theta = 20^\circ$ , $Y = Y_{MAX}$ , <u>no pole</u> ).	72
19	Comparison between the ionization rate time histories predicted by the GLANC and DAVID codes.	78
20	Comparison between the conductivity time histories predicted by the GLANC and DAVID codes.	80
21	Comparison between the Compton current time histories predicted by the GLANC and DAVID codes.	81
22	Comparison between the electric fields predicted by the GLANC and DAVID codes.	83
23	Comparison between the magnetic fields predicted by the GLANC and DAVID codes. Note the extra v/m scale on the GLANC curve ( $B(\text{gauss}) = 3 \times 10^4 H(\text{v/m})$ ).	85
24	Geometry used in the pole current calculation. Note the use of two pole sizes. The fat pole has a width ( $\Delta x$ ) of 30 cm and a circumference of 100 cm. The narrow pole has a width of 10 cm and a circumference of 60 cm. The dimensions include the image half of the pole on the other side of the symmetry plane. Cells are shown only near the boundaries.	87
25	Geometry used to compute current running on the "fat" pole (3 cells wide in x-direction, including image).	89
26	Currents generated on fat pole without ground conductivity enhancement. Numbers in parentheses are peak scaled currents (kamps). Air conductivity is also shown. Analytic sources.	92

FIGURE		PAGE
27	Currents generated on narrow pole without ground conductivity enhancement. Analytic sources.	94
28	Current induced on narrow pole (-45 cm) with and without ground conductivity enhancement. Ground drivers are used in each case.	96
29	Comparison between pole currents predicted with non-self-consistent prescribed sources and self-consistent particle sources. Ground drivers are considered, but not ground conductivity enhancement.	97
30	Comparison between pole currents predicted with and without ground currents. Enhancement in problem without currents is 1.5 times greater than in problem with ground currents, explaining difference in late time pole currents below surface. There was no difference in pole current observed at +70 cm. This calculation used particle sources in the air.	99
31	Comparison of currents calculated on the fat and narrow poles by DAVID (particle sources). Both calculations include ground conductivity enhancement.	101
32	Currents predicted for a 10 cm diameter gamma transparent pole at +30 cm and -45 cm. Calculations include effects of ground drivers and ground conductivity enhancement with a $10^{13}$ rad/sec rear flux. Self-consistent particle sources are used in the air.	103
33	Components of current running along sides of the "narrow" pole at +30 cm.	105
34	Components of current running along sides of the "narrow" pole at +70 cm.	106
35	Components of current running along sides of the "narrow" pole at -45 cm.	107
36	a. Variation of magnetic field in z-direction with pole (WP) and without pole (WOP) along a line at +30 cm height on symmetry plane. Particle sources, $T = 10.2$ ns. 1 gauss - 30,000 v/m.	108

FIGURE		PAGE
36	b. Variation of vertical electric field in z-direction with pole (WP) and without pole (WOP) along a line at +30 cm height on symmetry plane. Particle sources, $T = 10.2$ ns.	108
36	c. Variation of magnetic field in z-direction with pole (WP) and without pole (WOP) along a line at +30 cm height on symmetry plane. Particle sources, $T = 20.2$ ns.	109
36	d. Variation of vertical electric field in z-direction with pole (WP) and without pole (WOP) along a line at +30 cm height on symmetry plane. Particle sources, $T = 20.2$ ns.	109
37	Narrow pole currents generated with a peak flux of $10^{13}$ rad/sec at $20^\circ$ .	110
38	Narrow pole currents generated with a peak flux of $10^{13}$ rad/sec at $3^\circ$ .	111
39	Narrow pole currents generated with a peak flux of $10^{12}$ rad/sec at $3^\circ$ .	113
40	Narrow pole currents generated with a peak flux of $4 \times 10^{11}$ rad/sec at $3^\circ$ .	114
A-1	Problem geometry. Gamma wave front is parallel to x-axis. Wave normal makes angle $\theta$ , measured from the horizontal.	123
A-2	Ratio $J_p/J$ as a function of magnetic field intensity for three gamma ray energies (1.0, 1.5, 2.0 MeV). Curves are shown for the DX-DY approximation, the new approximation, and the new approximation fitted to the DX-DY predictions (1 MeV).	127
A-3	Ratio $J_N/J$ as a function of magnetic field intensity and gamma ray energy (1.0, 1.5, and 2.0 MeV). Curves are shown for the DX-DY approximation, the new approximation, and the new approximation fitted to the DX-DY predictions (1 MeV).	128

# FIGURE

# PAGE

- A-4

Ratio  $J_N/J_p$  as a function of magnetic field intensity for three gamma energies (1.0, 1.5, 2.0 MeV). Curves are shown for the DX-DY approximation, the new approximation, and the new approximation fitted to the DX-DY predictions (1 MeV).

129
- A-5

Effect of a surface on the current components generated by magnetic turning.

132

## TABLES

TABLE		PAGE
1	Values of the ratio $R_{mf}/E_{\gamma} R_{\gamma}$ as a function of gamma energy.	22
2	Values of the ratio $S_e/f_{\gamma}$ as a function of gamma energy.	23
3	Air chemistry formulas.	32
4	Types of physical boundary conditions used by DAVID.	39
5	Types of physical boundary conditions each side is presently allowed to assume.	39
6	IBOD/IBODG numbering system.	46
7	Relationship between general equation variables and the specific air chemistry quantities (variables in parentheses are names used in SUBROUTINE AIRCHEM).	60
A-1	$B_A$ as a function of gamma energy ( $E_{\gamma}$ ). These values are calculated using the DX-DY data published in Reference A-2.	131

## SECTION 1

### INTRODUCTION

In this report, we describe a 3-D finite difference code, DAVID, which can be used to estimate the currents and voltages induced on an arbitrarily shaped object, located over a finite conductivity ground plane if desired, when illuminated by a plane wave gamma source. As with all 3-D codes, the spatial resolution that can be obtained is severely limited by the amount of computer storage available and the amount of computer running time that the user can afford. Also, the accuracy of the physics must be compromised.

DAVID (and DAVEJR) was developed as a research code. It was designed to be reasonably accurate, relatively fast, and easy to understand and modify. It is intended to be used frequently by many people. Realizing that the first thing a researcher does when he uses a new code is "improve" it, we have endowed the first version of DAVID with only the most basic physics and many comment cards. The time and spatial steps are constant. Expanding spatial steps are impractical with arbitrarily shaped objects in any case. We try to make up for the loss of an expanding grid by improving the outer boundary condition, which allows it to be closer to the object. By virtue of the Cartesian coordinate system, which allows us to construct an object in a "building block" fashion, the field equations and electron momentum equations are in their simplest form. The object is constructed by designating certain cells of the grid by means of a flag. This flag causes any surface tangential electric fields and normal magnetic fields to be set equal to zero, i.e., a perfect conducting boundary condition. Any fields inside the object are also zeroed.

Normally, when we refer to DAVID in this report, we will also be describing DAVEJR. The only differences are in the source routine. DAVID is a particle pushing code, so that self-consistent effects can be included, while DAVEJR uses a prescribed source routine with a simple modification to approximate electron turning, if desired. Without the particles to store, DAVEJR can be made to run much faster or to perform higher resolution calculations. Each code is useful in its own way. The physics in DAVID is essentially the same as POST3D<sup>1</sup> and the one-dimensional phenomenology code GLANC<sup>2,3</sup>.

In Section 2 we will discuss the basic physics that is involved in the close-in coupling calculation—including those aspects which we do not feel can be handled appropriately in DAVID. In Section 3 the numerical techniques are displayed, and illustrative calculations are shown in Section 4. Our conclusions and recommendations are in Section 5.

## SECTION 2

### PROBLEM PHYSICS

#### 2.1 CLOSE-IN PHENOMENA

The phenomena of importance to close-in EMP coupling are those of EMP environment prediction, plus boundary-layer effects and surface electron emission. The essential physics of close-in coupling to a vertical post is discussed below.

Consider a vertical cylindrical post protruding from a finitely conducting ground, as shown in Figure 1. Assume that the line of sight from the post to a near-surface nuclear burst makes an angle  $\theta$  with the horizontal, and that the burst is sufficiently removed from the post that the gamma wave front seems planar.

As the gammas from the burst interact with the air they produce primary Compton electrons initially moving approximately parallel to the gamma flux. At points well above the ground and well removed from the post, only electric fields are initially present. As time progresses, magnetic fields are generated by the interaction of the electric fields with the boundaries, and the primary electrons are deflected by the magnetic fields. They are also influenced by the existing electric fields, and slowed by the effective drag force due to ionizing collisions with air molecules.

Ionizing collisions of primary electrons with air molecules create substantial numbers of free secondary electrons and positive ions. Some of

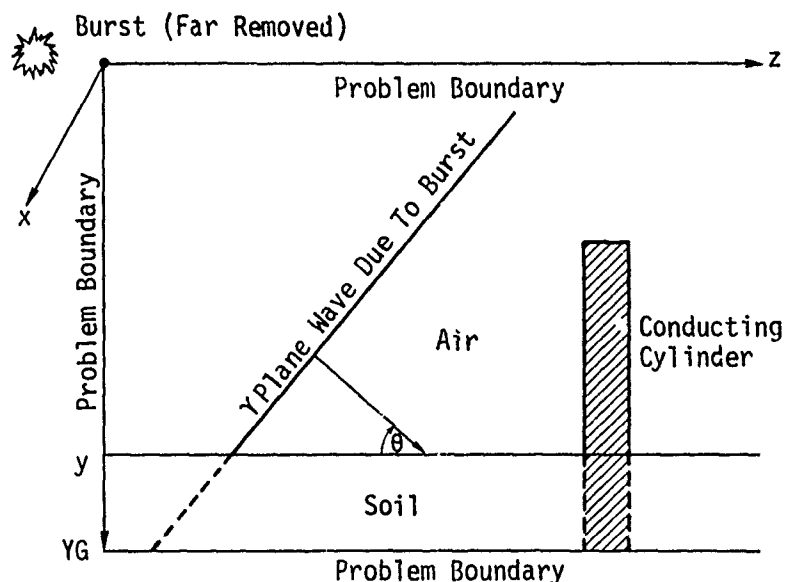


Figure 1. Example problem geometry.

the secondary electrons attach to  $O_2$  molecules to form  $O_2^-$  ions, some free electrons recombine with positive ions, and some positive and negative ions recombine. Large electric fields may cause electron avalanching in the air. The rates of these processes are all distinct, and the electron attachment rate to  $O_2$  depends upon the electric field amplitude. The charged species and the neutral air molecules create a collision-dominated plasma. Secondary electron and ionic currents may thus be incorporated into Maxwell's equations via an ohmic conductivity. Conductivity is calculated using the mobilities of electrons and ions, where electron mobility in turn depends on the amplitude of the electric field.

Electromagnetic fields modify the primary electron trajectories as well as the electron mobility and attachment rates. The overall problem is clearly nonlinear and must be solved by numerical methods.

Self-consistent treatment of the primary (Compton) electron dynamics is the key problem in the present studies. Many of the phenomena outlined above can be included in three-dimensional calculations which do not treat electron dynamics self-consistently. However, there are conditions where even the initial direction of current flow on the object is uncertain due to self-consistent effects. For example, consider a gamma flux incident on the vertical post at an angle of about  $30^\circ$  with respect to the horizontal. Magnetic fields due to conductors tend to deflect the primary electrons away from the conductors. The ground thus tends to deflect the electrons upward and the post tends to deflect them downward. Net deflection is clearly uncertain, as is the initial direction of current on the post which would usually oppose the vertical current in the air.

Relative responses of gamma-thick and gamma-thin conductors may also be greatly modified by self-consistent effects. Self-consistent deflection of the primary electrons may reduce the charge collection by the object. For gamma-thin objects, emitted current may greatly exceed that collected, while for gamma-thick objects the total charge collection may be much less than expected. Emission of electrons by the object plays a pivotal role and must be treated as accurately as possible. We do not feel that a 3-D code, which must store data for thousands of particles being born in the air can be trusted to do a reasonable job with particle emission from an object as well. The problem is compounded by the lack of resolution in the spatial grid. Future calculation may show us wrong, but as far as the first version of DAVID is concerned, we have chosen a different approach for the case of a gamma-thin object in air. Instead of emission specifically from the object's surface, we allow the code to forget that the object is there during normal particle injection and movement processes. Unless the air is very thin, this is a good first order approximation because the current is almost continuous across the boundary. The above procedure gives us a smoothly varying current distribution behind the object. The code is constructed in such a way that it would be almost trivial to include an object

emission scheme, but if it is not done well, the unreal current distribution in the layer of cells behind the pole can give rise to fields which reflect the numerical treatment rather than the physics.

The objects used in DAVID and DAVEJR can be either gamma-thin or gamma-thick, i.e., they can be either completely transparent or completely opaque. If we were limited to a single simple object, e.g., a pole, we could easily allow for an object with a partial shadow (gamma translucent). However, when one part of an object can shade another part or one object can shade another, the logic involved with partial shadowing can take up a significant amount of computer storage.

DAVID uses a particle treatment of the Compton electrons. Particles, representing large numbers of Compton electrons, are injected at appropriate times and spatial locations within the problem geometry; weights are assigned to the particles according to the number of Compton electrons which they represent. All of the particles are advanced in time, using the Lorentz and drag forces appropriate to each individual particle. Based upon particle locations and velocities, current density and ionization rate are calculated for all spatial points in the finite-difference mesh. The air-ion equations are advanced in time and conductivity is calculated for each point in the mesh. This is done using the existing electric amplitudes at that point to evaluate the field-dependent mobility, attachment and avalanche parameters. Maxwell's equations are then advanced in time, using current density and conductivity values as determined above. New particles are injected according to the time and spatial distribution of the gamma flux. The process is repeated cyclically until the desired problem time is reached.

Because of computer time limitations, the present state of the art in EMP environment calculations cannot be realized in three-dimensional close-in coupling calculations. Treatments of gamma-ray energy spectra and initial angles (and angle-dependent energy) of Compton electron ejection lead to

excessively large numbers of primary particles and cause unacceptably long computation time. Instead, monoenergetic gammas must be considered, and the primary Compton electrons must be ejected parallel to the gamma flux (or normal to surfaces in the case of surface emission). The generation of a boundary layer near the surface of the object, wherein positive ions and electrons separate and form a gap under the influence of the normal electric field, has not been treated in the present code. Preliminary estimates indicate that: (1) the high capacitance across the boundary layer reduces its electromagnetic influence; (2) radiation will splash electrons across the boundary, reducing its influence again; and (3) the contamination of any real surface will affect the problem in such a way as to allow electron charge to be drawn off of the surface more easily than in the ideal case, especially with the added influence of the molecular collisions of sea level air.

In the remainder of this section, we present and discuss the actual equations upon which DAVID and DAVEJR are based.

## 2.2 FIELD EQUATIONS

The field equations used in DAVID are Maxwell's equations in Cartesian coordinates. MKS units are used throughout, with the exception that the magnetic field is in volts/meter, i.e., the quantity  $\vec{h} = Z_0 \vec{H}$  is carried, where  $Z_0$  is the impedance of free space ( $\sim 120 \pi$  ohms). For a wave propagating in free space, then, the electric and normalized magnetic fields would be equal. The use of  $\vec{h}$  instead of  $\vec{H}$  helps in studying the physics and diagnosing calculations. In conducting regions, we have  $|\vec{E}| < |\vec{h}|$ . In order to keep units consistent, the current density must also be multiplied by  $Z_0$ .

The equations used in DAVID are, in vector form

$$\frac{\partial \vec{E}}{\partial t} + \frac{\sigma}{\epsilon} \vec{E} = c(\nabla \times \vec{h} - \vec{j}) , \quad (1)$$

$$\frac{\partial \vec{h}}{\partial t} = -c \nabla \times \vec{E} , \quad (2)$$

where

$\sigma$  = conductivity (mho/m)

$\epsilon$  = permittivity (farad/m)

$c$  = speed of light ( $3 \times 10^8$  m/sec)

$\vec{h} = Z_0 \vec{H}$  (v/m)

$\vec{j} = Z_0 \vec{J}$  (v/m<sup>2</sup>)

$\vec{H}$  = magnetic field (amp/m)

$\vec{J}$  = driving (Compton) current density (amp/m<sup>2</sup>)

$Z_0 = \sqrt{\mu/\epsilon}$  (ohm)

$\mu$  = permeability (henries/m)

The boundary conditions at the object are those of a perfect conductor, i.e., the tangential  $\vec{E}$  and normal  $\vec{H}$  are zero (these are not independent conditions). We assume that the problem has mirror symmetry in order to decrease the number of grid cells required. At the symmetry plane, the normal  $\vec{E}$  and tangential  $\vec{H}$  fields are zero. Two types of outer boundary condition are used: the perfect conductor (PC) and a fake ambient environment (FAE) condition. The FAE condition allows one to move the outer boundary much closer than could be allowed with perfectly conducting walls with a given air conductivity. It uses some of the field characteristics that one would see if the object were not present, without actually calculating those fields. This will be discussed in Section 2. The particular treatment used in DAVID can be improved considerably, but has been shown to be reasonably successful even in its primitive form (see Section 4).

Even though a particular boundary condition may not cause the currents running on a single pole to be in great error, it does change the field distribution in space considerably. The pole currents do not change drastically, at early times at least, because the current is limited in large part by the energy stored in local fields located very close to the surface. These fields determine the inductance and capacitance of the pole. The quasi-static fields are not greatly affected by what is happening far away. However, with two objects, or with some convoluted object, the distribution of the fields in space can become quite important, and hence, so do the boundary conditions.

### 2.3 MOMENTUM EQUATIONS

The relativistic Compton electron momentum equation in our system of units ( $\hbar = Z_0 \vec{H} = c \vec{B}$ ) is

$$\frac{d\vec{p}}{dt} = -e(\vec{E} + \frac{\vec{v}}{c} \times \vec{h}) - \frac{dE_e}{dR_{mf}} \frac{\vec{p}}{p}, \quad (3)$$

where

$$p = |\vec{p}|$$

$$\frac{v}{c} = \frac{\vec{p}}{\sqrt{p^2 + (mc)^2}}, \quad (3a)$$

$$\frac{dE_e}{dR_{mf}} = \frac{e \cdot 10^8 \rho}{400} \frac{(E_e + 0.3)^2}{E_e (E_e + 0.6)} \text{ (Newtons)}, \quad (4)$$

$$E_e = mc^2 (\sqrt{1 + (p/mc)^2} - 1) \text{ (MeV)}, \quad (5)$$

$\rho$  = air density ( $\text{kg/m}^3$ )

$m$  = electron rest mass

$mc^2 \approx 0.511$

$e$  = electron charge ( $1.6021 \times 10^{-19}$  coulomb)

The drag term  $dE_e/dR_{mf}$  is obtained by differentiating the fitted mean range-energy relation<sup>3</sup> and converting energy to joules:

$$R_{mf} = \frac{4.0E_e^2}{\rho(E_e + 0.3)} \quad (\text{meters}) \quad (6)$$

Particles are advanced once each time step using previously calculated fields. The previous value of  $P$  is also used in the calculation of the drag force and  $v/c$ .

## 2.4 SELF-CONSISTENT (PARTICLE) SOURCES

The particle motion and energy loss rate must be converted into Compton currents and ionization rates. The Compton currents go directly into the field calculation. The ionization rate is the driver for the air chemistry equation, which generates the electron and ion densities necessary for the conductivity calculation. The conductivity, in turn, is used in the field calculation.

Each particle represents the number of electrons formed within a cell of volume  $dV$  over a period of time  $dt$ . The electron current  $\vec{J}$  is then given by

$$\vec{J} = -eN_c \vec{v} \quad (\text{amp/m}^2), \quad (7)$$

where  $N_c$  is the Compton electron density (particles/m<sup>3</sup>) and  $\vec{v}$  is the particle velocity given by Equation 3a. The density,  $N_c$ , is given by

$$N_c = W/dV \quad (\text{electrons/m}^3), \quad (8)$$

where the weight  $W$  is the total number of particles and is given by

$$W = \mu_c \rho \langle \dot{\gamma} \rangle dV dt \quad (\text{electrons}). \quad (9)$$

Here,  $\mu_c$  is Compton scattering mass attenuation coefficient (m<sup>2</sup>/kg),  $\rho$  is the air density, and  $\langle \dot{\gamma} \rangle$  is the average photon flux (photons/m<sup>2</sup> - sec) over the time interval of interest. Actually, since DAVID uses the same cell size everywhere, the  $dV$  factor is not necessary.

In order to save storage, particles are not injected at every cell so an averaging scheme is necessary. This is discussed in Section 3.4.

The mass attenuation coefficient is calculated as a function of gamma energy from the scattering cross section given by Evans<sup>4</sup>. The cross section is

$$e\sigma_s (\text{cm}^2/\text{elec}) = \pi r_0^2 \left[ \frac{1}{\alpha^3} \ln(1+2\alpha) + \frac{2(1+\alpha)(2\alpha^2-2\alpha-1)}{\alpha^2(1+2\alpha)^2} + \frac{8\alpha^2}{3(1+2\alpha)^3} \right], \quad (10)$$

where

$$\begin{aligned} r_0 &= \text{classical electron radius} \\ &= e^2/m_0 c^2 \approx 2.818 \times 10^{-13} \text{ cm} \\ \alpha &= E_\gamma/m_0 c^2 \approx E_\gamma/0.511 \\ E_\gamma &= \text{gamma energy}. \end{aligned}$$

The advantage to using the mass attenuation coefficient instead of the scattering cross section is that it is essentially independent of the

material or its physical state<sup>4</sup>. We obtain the attenuation coefficient in the following way:

$$\mu_c(\text{cm}^2/\text{gm}) = \sigma_c(\text{cm}^2/\text{electron}) \times 7.2(\text{electrons/air atom}) \times 6.025 \times 10^{23} (\text{atoms/mole})/14.4 (\text{gm/mole}) . \quad (11)$$

The conversion to MKS units is

$$\mu_c(\text{m}^2/\text{kg}) = 0.1\mu_c(\text{cm}^2/\text{gm}) . \quad (12)$$

The total cross section (including both Compton scattering and absorption) is

$$\sigma = 2\pi r_0^2 \left\{ \frac{1+\alpha}{\alpha^2} \left[ \frac{2(1+\alpha)}{1+2\alpha} - \frac{1}{\alpha} \ln(1+2\alpha) \right] + \frac{1}{2\alpha} \ln(1+2\alpha) - \frac{1+3\alpha}{(1+2\alpha)^2} \right\} (\text{cm}^2/\text{elec}) . \quad (13)$$

The absorption cross section is then

$$\sigma_a = \sigma - \sigma_s . \quad (14)$$

The mass absorption coefficient,  $\mu_a$ , for which we will have need for later, is calculated in the same way as  $\mu_c$ .

We only consider Compton-processes in the source calculation. We ignore the photoelectric effect and pair production. This will be reasonable if we confine our photon energies to between 0.5 MeV and 5 MeV.

The initial direction of the Compton scattered electron is taken to be parallel to the direction of the incident gamma rays. The electron is given an energy equal to the average energy of all the recoil electrons

$$T_{av} = E_\gamma (\sigma_a / \sigma) . \quad (15)$$

The electron energy is about  $\frac{1}{2} E_\gamma$  for 1.6 MeV gammas. The initial electron momentum is then given by the inverse of Equation 5:

$$P_0 = mc \left[ \left( \frac{E_e}{mc^2} + 1 \right)^2 - 1 \right]^{1/2} \quad (16)$$

The ionization rate is proportional to the Compton electron energy loss rate, with about 1 conduction electron being created for each 34 eV lost by the Compton electron. The ionization rate necessary for the air chemistry equations is

$$S_e (\text{ion-pairs/m}^3\text{-sec}) = N_c \frac{dE_e}{dR_{mf}} \frac{\vec{p} \cdot \vec{v}}{P} \frac{1.6021 \times 10^{-13}}{3.4 \times 10^{-5}} \quad (17)$$

## 2.5 PRESCRIBED (ANALYTICAL) SOURCES

Under steady state conditions, the Compton current in a medium which is homogeneous over the electron range is proportional to the photon flux. This remains true with a time dependent gamma source so long as the electron life time is short, so that equilibrium is maintained and electromagnetic fields are not strong enough to affect electron motion. These two conditions generally translate into high material density and low gamma flux\*.

When the proper conditions are present, the Compton current is equal to

$$\vec{J} = - e \gamma \frac{R_{mf}}{R_\gamma} \hat{i}_\gamma \quad (18)$$

---

\* In the case of a fast exponentially rising pulse, the deviation from the steady state condition manifests itself as a simple delay. In air, this delay is several nanoseconds. In the ground, it is negligible. Therefore, properly treated prescribed sources would have the ground drivers peaking before the air Compton currents. This delay has not yet been built into DAVEJR. Its absence is obviated by the comparison of Figure 29.

where  $\dot{\gamma}$  is the photon flux (photons/m<sup>2</sup>/sec),  $\hat{i}_\gamma$  is a unit vector oriented in the direction of the photon flux,  $R_{mf}$  is the mean electron range, given by Equation 6, and  $R_\gamma$  is the gamma mean range. DAVEJR uses

$$R_\gamma = (\mu_c \rho)^{-1} \quad (19)$$

where  $\rho$  is the air density and  $\mu_c$  is the mass Compton collision attenuation coefficient as described in Section 2.4.

The ratio  $R_{mf}/E_\gamma R_\gamma$  is a fairly constant function of the gamma energy,  $E_\gamma$ <sup>5</sup>. In terms of this ratio, the Compton current is

$$\vec{J} = -e f_\gamma \frac{R_{mf}}{E_\gamma R_\gamma}, \quad (20)$$

where the gamma energy flux,  $f_\gamma$  is given by

$$f_\gamma = E_\gamma \dot{\gamma}, \quad (21)$$

for a monoenergetic source. Table 1 shows the ratio for various values of  $E_\gamma$ . It is a corrected version of a table used in Reference 5.

A simple two-piece linear fit describes the ratio well over the 1 - 5 MeV range\*. The fit is (see Figure 2)

Table 1. Values of the ratio  $R_{mf}/E_\gamma R_\gamma$  as a function of gamma energy.

$E_\gamma$ (MeV)	$\frac{R_{mf}}{E_\gamma R_\gamma}$ (1/MeV)
1.0	0.0064
1.5	0.0071
3.0	0.0069
5.0	0.0062

\* This curve fit and the one for ionization rate are not used in DAVID/DAVEJR, but are shown because the reader may prefer to use this alternate technique in a code of his own.

$$\frac{R_{mf}}{E_{\gamma} R_{\gamma}} = \begin{cases} 10^{-3}(5.0 + 1.4E_{\gamma}) , & 1 \leq E_{\gamma} \leq 1.69 \text{ MeV} \\ 10^{-3}(7.95 - 0.35E_{\gamma}) , & 1.69 < E_{\gamma} \leq 5 \text{ MeV} \end{cases} \quad (22)$$

The ionization rate is also proportional to  $\dot{\gamma}$ . In DAVEJR, we use the formula

$$S_e \left( \frac{\text{ion pairs}}{\text{m}^3 - \text{sec}} \right) = \mu_a \rho \dot{\gamma} \frac{E_{\gamma}}{3.4 \times 10^{-5}} , \quad (23)$$

where  $\mu_a$  = mass Compton absorption coefficient (see Section 2.4).

The ratio  $S_e/f_{\gamma}$  is also a slowly varying function of the gamma energy over the range  $1 \leq E_{\gamma} \leq 5 \text{ MeV}$ . Table 2 shows values taken from Reference 5 and converted to MKS.

A simple curve-fit describes this ratio. It is

$$\frac{S}{f_{\gamma}} \left( \frac{\text{ion-pairs}}{\text{m} - \gamma - \text{MeV}} \right) = 115 E_{\gamma}^{-0.275}$$

The fit and data points are shown in Figure 2.

Prescribed sources are used for underground currents in both DAVID and DAVEJR. The parameters are the same as in the air (Equations 18 and 19).

Table 2. Values of the ratio  $S_e/f_{\gamma}$  as a function of gamma energy.

$E_{\gamma}(\text{MeV})$	$S_e/f_{\gamma}(\text{ion-pairs/m-}\gamma\text{-MeV})$
1.0	115
1.5	100
3.0	85
5.0	73

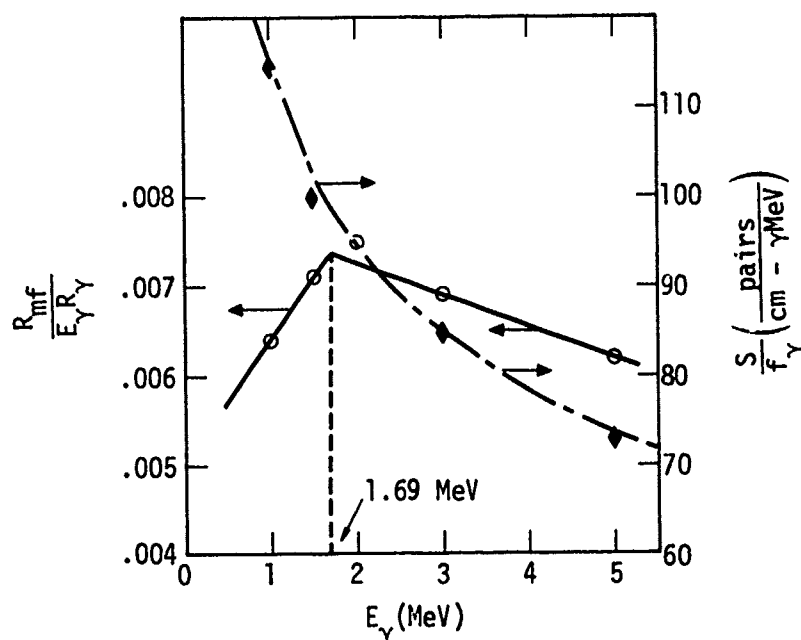


Figure 2. Plot of ratios useful in calculating prescribed currents and ionization rates. Curve-fits are layed over data points.

The photon flux is attenuated considerably by the soil, of course (see Section 2.6). Provision has been made for the inclusion of a time dependent soil conductivity caused by gamma-ray enhancement. There is a large amount of uncertainty as to what the dependence of the enhanced conductivity on the gamma ray flux is. At this time the codes use a function which makes it proportional to  $\dot{\gamma}$ , i.e., the gamma flux (really the dose rate, but the two are proportional with a single photon energy).

An approximation for magnetic field turning effects on the Compton current in the air is described in Appendix A. It is useful only in the presence of small fields, when the electron does not turn too far. Electric fields are neglected. The latter influence could be included with no difficulty using the same principles. At this time, we were simply looking for the first order effect of having a new component of current introduced, which is normal to the radial component. Only the component of  $\vec{H}$  which would ordinarily be present without the existence of an object ( $H_x$ ) is presently considered. The other components could easily be included also.

## 2.6 THE PHOTON FLUX

The gamma flux at a distance  $r$  from the burst is, at the local time  $t' = t - r/c$ ,

$$\dot{\gamma}(\text{photons/m}^2\text{-sec}) = \frac{A(r)}{4\pi r^2} F_0(t') . \quad (25)$$

The function  $F_0(t')$  is the gamma time history, normalized to unit area. The time histories used by DAVID and DAVEJR are different and will be described later.

It is assumed that the variation of the current magnitude with  $r$  is negligible over the calculational volume, except through the variation of  $t'$  and except for attenuation in the soil. The function  $A(r)$ , in the air, is

$$A(r) = Y_{KT} \epsilon_{\gamma} K \exp(-\mu_T \rho r) / E_{\gamma} , \quad (26)$$

where

$Y_{KT}$  = weapon yield (KT)

$\epsilon_{\gamma}$  = gamma efficiency

$K = 2.613 \times 10^{25}$  (MeV/KT)

$\rho$  = air density (l.g/m<sup>3</sup>)

$E_{\gamma}$  = photon energy (MeV)

$\mu_T$  = total attenuation coefficient (m<sup>2</sup>/kg)

$r$  = range over which gammas are attenuated

The function  $A(r)$  for a point in the ground is the same, except that it is multiplied by an extra attenuation term, i.e.,

$$A_{\text{ground}} = A(r) \cdot \exp(-\mu_g \rho_g \Delta r) , \quad (27)$$

where

$\mu_g$  = ground attenuation coefficient ( $m^2/kg$ )

$\rho_g$  = ground density ( $kg/m^3$ )

$\Delta r$  = distance traveled through ground

The codes use  $\mu_g = \mu_c$ , where  $\mu_c$  is the same as that of air. Note that multiple scattering terms are ignored. These are important in determining the current distribution at small incidence angles, i.e., nearly horizontal.

DAVEJR uses the simplest time history of the two codes

$$F_0(t) = \frac{f_0 e^{at}}{1 + \frac{a}{b} e^{(a+b)(t-t_0)}} \quad (28)$$

where  $t_0$  is the time of peak and  $f_0$  normalizes the area to unity

$$f_0 = \frac{1}{\pi} (a+b) e^{-at_0} \sin\left(\frac{\pi a}{a+b}\right) \quad (29)$$

Since  $F_0(t)$  extends back to  $t = -\infty$ , it is necessary to adjust  $t_0$  so that the function is very small at  $t = 0$ . Given the ratio  $R = F(0)/F(t_0)$ , an approximation for  $t_0$  is

$$t_0 = t_1 + t_2 \quad (30)$$

where

$$t_1 = \frac{-1}{a} \ln\left(\frac{R}{1 + a/b}\right)$$

$$t_2 = \frac{1}{a+b} \ln\left[1 + \frac{a}{b} \left(\frac{R}{1 + a/b}\right)^{\frac{a+b}{a}}\right]$$

The code accepts either  $R$  or  $t_0$  as input.

DAVID uses the more complicated four piece function used in GLANC<sup>2</sup>. It is normalized numerically and the time of peak is an input parameter. The function is shown qualitatively in Figure 3. The parts are given by

$$F_0^1(t) = A_1 e^{b_1(t-t_2)}, \quad t \leq t_1, \quad (31a)$$

$$F_0^2(t) = A_2 \frac{\left(1 + \frac{b_2}{b_3'}\right) e^{b_2(t-t_2)}}{1 + \frac{b_2}{b_3'} e^{\frac{b_2}{b_3'}(t-t_2)}}, \quad t_1 < t \leq t_2, \quad (31b)$$

$$F_0^3(t) = A_2 \frac{1 + \frac{b_2'}{b_3} e^{b_2'(t-t_2)}}{1 + \frac{b_2'}{b_3} e^{\frac{b_2'}{b_3}(t-t_2)}}, \quad t_2 < t \leq t_3, \quad (31c)$$

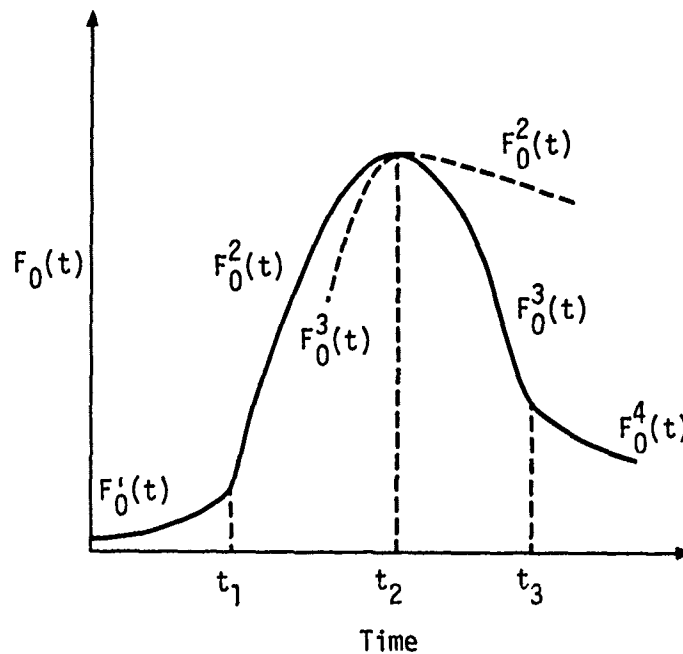


Figure 3. Qualitative plot of the  $\dot{\gamma}$  time history used in program DAVID.

$$F_0^4(t) = A_3 e^{-b_4(t-t_2)}, \quad t_3 < t. \quad (31d)$$

In order to make this function the same as the simple one used by DAVEJR, set the following equalities:

$$b_1 = b_2 = b'_2$$

$$b_3 = b'_3 = b_4.$$

In addition, set  $t_2 = t_0$  and maintain  $t_1 < t_2 < t_3$ .

Both DAVID and DAVEJR have the option of normalizing the  $\dot{\gamma}$  curve to a peak flux ( $\text{MeV/m}^2\text{-sec}$ ) or dose rate ( $\text{rad/sec}$ ). If the yield that is input (YKT) is less than  $10^4$  KT, the code assumes that we have entered a yield in KT, a gamma efficiency (EPG), and an attenuation range (ROB). If  $10^4 < \text{YKT} \leq 10^{19}$ , the input is assumed to be in rads (air)\* per second. If  $\text{YKT} > 10^{19}$ , the input is assumed to be in units of  $\text{MeV/m}^2\text{-sec}$ . When YKT is in rads/sec, the number is first converted to  $\text{MeV/m}^2\text{-sec}$ . The relation between the two is

$$\mathcal{E}(\text{rad/sec}) = 1.602 \times 10^{-12} \mu_a (\text{cm}^2/\text{gm}) F(\text{MeV/m}^2\text{-sec}) \quad (31e)$$

where  $\mu_a$  is the mass Compton absorption coefficient (see Section 2.4). The curve is normalized to unity in the usual manner, but the coefficients  $A_1$ ,  $A_2$ , and  $A_3$  (DAVID) or  $f_0$  (DAVEJR) are then renormalized by the ratio of the desired peak  $\dot{\gamma}$  to the peak  $\dot{\gamma}$  of the function which was normalized to unity.

## 2.7 AIR CHEMISTRY

In order to calculate air conductivity, the densities of free (secondary) electrons, and positive and negative ions must be known. The

---

\* This is essentially rad (Si)/sec for our purposes.

treatment of these quantities is identical to that in the MRC environment codes; we repeat it here for the sake of completeness.

Free electrons and positive ions of density  $n_e$  and  $n_+$  are created at a rate  $S_e$  (ion pairs/ $m^3$ -sec) by the ionizing collisions of primary electrons with the background air. Electrons attach to  $O_2$  with rate coefficient  $\beta$  forming  $O_2^-$  ions, of density  $n_-$ . Electrons recombine with positive ions with rate coefficient  $\alpha$ , and positive and negative ions recombine with rate coefficient  $\Gamma$ . Finally, if the electric field strength is sufficiently high, secondary electrons may gain sufficient energy between collisions to ionize air molecules in subsequent collisions, creating additional secondary electrons at an avalanche rate  $G$ .

We assume that the secondary electrons and ions everywhere maintain local charge neutrality,

$$n_+ = n_e + n_- . \quad (32)$$

The rate equations describing the production of secondary electrons and negative ions are

$$\frac{dn_e}{dt} = S_e - (\beta + G)n_e - \alpha n_e n_+ , \quad (33)$$

$$\frac{dn_-}{dt} = \beta n_e - \Gamma n_+ n_- . \quad (34)$$

The assumption of local charge neutrality is clearly not satisfied in a boundary layer, if indeed a boundary layer does develop. Further, the usual divergence terms are not present in Equations 33 and 34. In Equation 33, a term  $\nabla \cdot n_e v_d$  would normally be present. However, in the present problems, secondary-electron drift velocities are such that the distance of characteristic change in the electron drift current  $n_e v_d$  must be smaller than  $10^{-4}$  meters before the divergence of the secondary electron current

becomes comparable to attachment. Clearly, this term is important only to the formation of a boundary layer and not to other portions of the problem where quantities change characteristically in distances on the order of 0.1-1. meters.

Given the electron and ion densities, the air conductivity is

$$\sigma = e(\mu_e n_e + \mu_i (n_+ + n_-)) \quad (35)$$

The parameters  $\beta$ ,  $G$ ,  $\alpha$ ,  $\Gamma$ ,  $\mu_e$  and  $\mu_i$ , which are required to calculate the air conductivity, are obtained from curve fits to existing data performed by Longley, Longmire, Radasky and others. The parameters are summarized in Table 3. One should note that the attachment rate  $\beta$ , avalanche rate  $G$ , and electron mobility  $\mu_e$  are dependent upon local electric field amplitude, relative air density and water vapor content of the air. The other parameters depend upon relative air density; the electron-ion recombination rate also depends upon the water vapor content of the air. Field-dependent parameters for dry air are plotted in Figure 4.

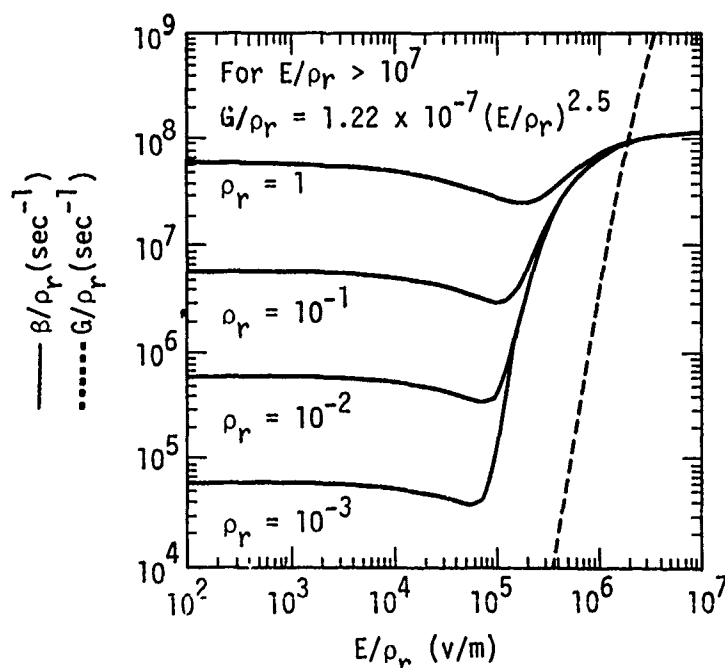


Figure 4a. Electron attachment and avalanche coefficients for dry air.

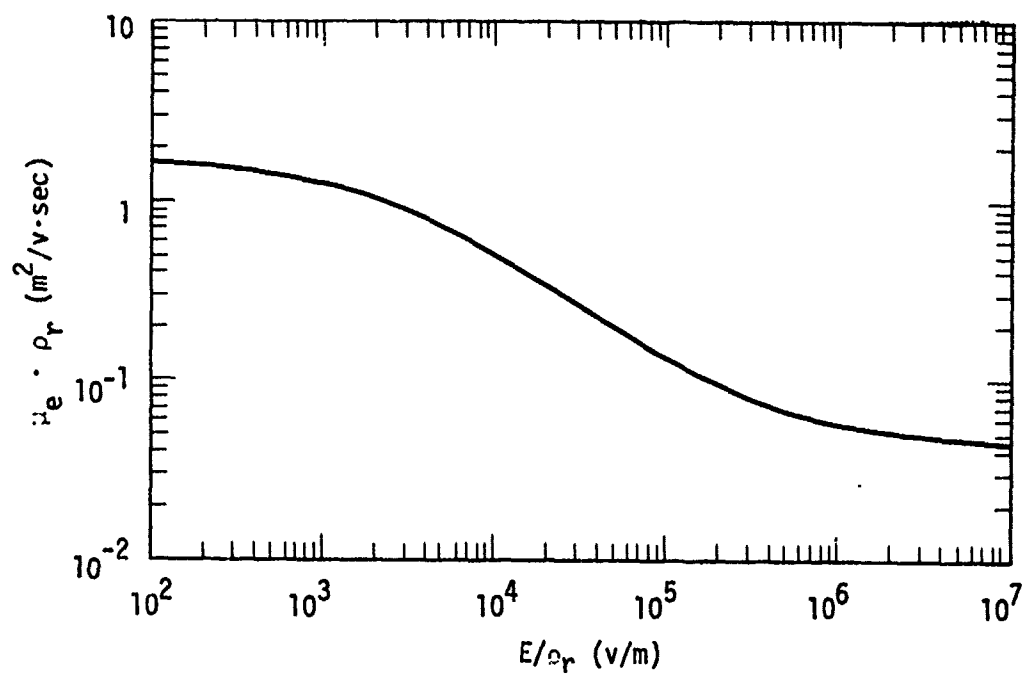


Figure 4b. Electron mobility in dry air.

Table 3. Air chemistry formulas.

DEFINITIONS:

$$\rho_r = \frac{\rho}{1.23 \times \text{kg/m}^3}, \quad E = \sqrt{E_r^2 + E_\theta^2 + E_\phi^2}$$

$$E(\text{esu}) = E(\text{mks}) / (3 \times 10^4)$$

ATTACHMENT RATE:

(E is in esu,  $\rho_r$  is relative air density, P is % water vapor content)

$$\beta (\text{sec}^{-1}) = \frac{6.3 \times 10^7 \rho_r^2}{\sqrt{\frac{E}{\rho_r} + X}} + 1.3 \times 10^8 \rho_r \exp \left( - \frac{25 \rho_r}{E + 10^{-4}} \right)$$

$$X = (6.3 / (6.132 + 1.838P))^2$$

AVALANCHE RATE:

(E is in esu,  $\rho_r$  is relative air density)

$$G(\text{sec}^{-1}) = \frac{5.7 \times 10^8 \rho_r y^5}{1 + 0.3 y^{2.5}}, \quad y = \frac{E}{100 \rho_r}$$

ELECTRON MOBILITY:

(E is in esu,  $\rho_r$  is relative air density, P is % water vapor content)

$$\mu_d \left( \frac{\text{m/sec}}{\text{volts/m}} \right) = \frac{4}{15 \rho_r} \left[ \frac{6 + \left( \frac{E}{\rho_r} \right)^{0.85}}{1 + 6 \left( \frac{E}{\rho_r} \right)^{0.85}} \right]$$

$$R_w = 1.7322 \rho_r P^{0.8}$$

$$\mu_e \left( \frac{\text{m/sec}}{\text{volts/m}} \right) = \frac{\mu_d}{\sqrt{1 + (R_w \mu_d)^2}}$$

RECOMBINATION  
COEFFICIENTS:

( $\rho_r$  is relative air density, P is % water vapor content)

$$\text{Electron-Ion}(+) \quad , \quad \alpha (\text{m}^3/\text{sec}) = 2.0 \times 10^{-13} + 2.8 \times 10^{-12} P^{1/3}$$

$$\text{Ion}(-)\text{-Ion}(+) \quad , \quad \Gamma (\text{m}^3/\text{sec}) = 2.0 \times 10^{-13} + 2.1 \times 10^{-12} \rho_r$$

IONIC MOBILITY:

( $\rho_r$  is relative air density)

$$\mu_i (+) \left( \frac{\text{m/sec}}{\text{volts/m}} \right) = \frac{2.5 \times 10^{-4}}{\rho_r}$$

## SECTION 3

### THE NUMERICAL SOLUTION

#### 3.1 OVERVIEW AND PROBLEM GEOMETRY

Program DAVID is written as a particle moving code with field and air chemistry subroutines. Since the particle calculation dominates the running time requirements, particle information is stored in CDC 7600 small core memory (SCM), while the field and ionization arrays are stored in large core memory (LCM). With the large amount of storage required by the plotting packages, we are limited to about 4000 particles in SCM at one time. This usually proves more than adequate. If necessary, we could buffer groups of 4000 in and out of LCM. The CDC 6600 has twice as much small core, but uses an extended core memory (ECM) which does not allow random access. There would be the usual amount of difficulty in converting from one machine to the other.

Figure 5 shows the basic program flow. Note the separation of events into groups for which numbers appear at half-time steps and integral time steps. Constant time steps are used throughout the entire calculational interval. The program flow for DAVEJR is the same, with only the current calculation being different. The conductivity calculation is shown as a separate block. In the codes, it is included as part of the electric field calculation. This is mostly to save storage (the conductivity is not stored and must be recalculated by the output code), but it is also convenient to do this because of the special calculations one must do near the outer boundary; the fields routine was already designed to handle the boundaries separately.

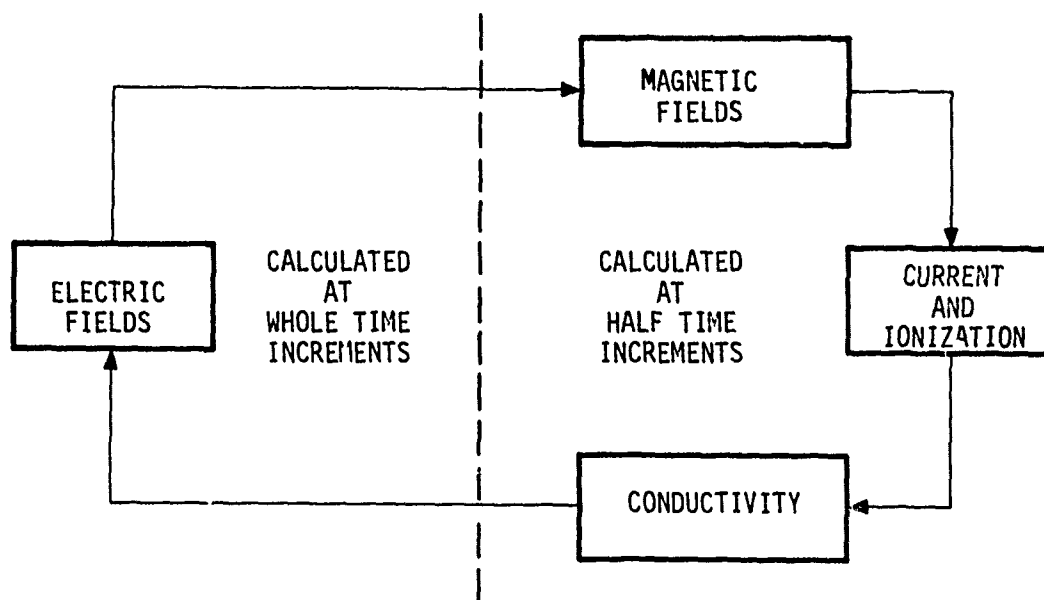


Figure 5. General flow pattern of programs DAVID and DAVEJR.

The coordinate system used in the programs is shown in Figure 6. Two features are unusual. The first is that the vertical coordinate ( $y$ ) is pointed downward (which must be remembered when looking at the calculations of vertical field and current components) and the second is that there are two separate coordinate systems: one in the air and one in the ground. In fact, the entire solution is effectively broken into two regions with the techniques being different in each case. There are numerous advantages to having the coordinate system oriented in the way that it is, and these may become apparent as we discuss the numerical techniques.

The gamma plane wave front is incident from the left and upper sides and travels in the  $+y$  and  $+z$  directions. Real time is used (as opposed to local time) and  $t = 0$  occurs when the wave front reaches the  $y = 0, z = 0$  line. Note that all events occurring along on  $x$ -coordinate happen at the same time.

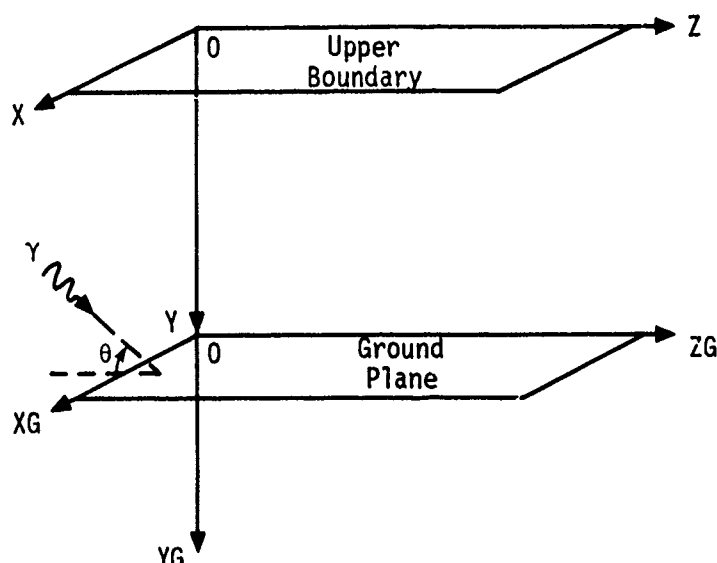


Figure 6. Coordinate system used in program DAVID. Note the separate coordinate system used below the ground plane.

The calculational volume is divided into cells with the dimensions  $\Delta x$ ,  $\Delta y$ , and  $\Delta z$ . Fields, currents, and ionization rates are located by the cell in which they are assigned. Figure 7 shows how the cells are arranged within the grid. Note that there is an extra layer of cells below the ground surface. These extra cells contain the field components necessary for specifying the field boundary conditions, as well as acting as trash cans for particles leaving the grid. In the future they may prove useful for other reasons, such as improved boundary conditions or for holding particles which represent electrons splashing back out of the soil.

Each cell has six field components associated with it, as well as the three current components and the electron/ion densities.  $\vec{J}$  and the densities are located at the center of the cell. The field components are located along the sides, as shown in Figure 8. The electric field components are centered on the edges to which they are parallel. The magnetic field components are centered on the sides to which they are normal. This has obvious advantages when specifying boundary conditions. The  $\vec{E}$  and  $\vec{H}$



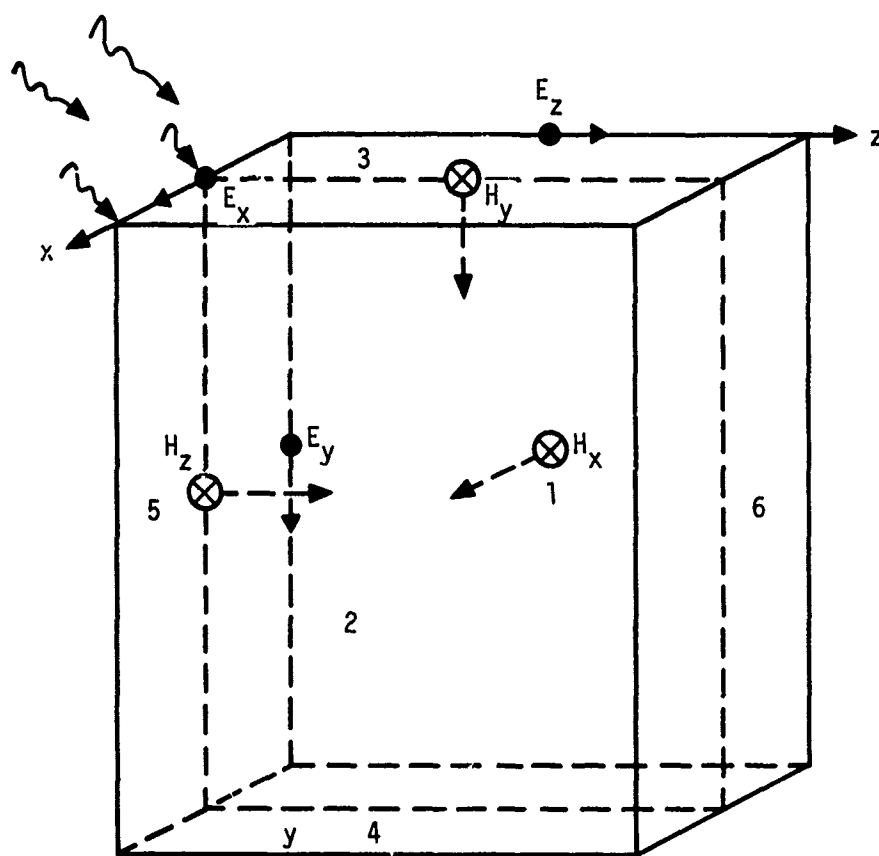


Figure 8. Unit cell used in program DAVID. Sides are numbered to illustrate the grid boundary numbering system.

components are also centered with respect to each other in the curl sense. For example, the calculation of  $E_z$  requires the z-component of  $\nabla \times \vec{H}$ , or  $\partial H_y / \partial x - \partial H_x / \partial y$ . The components of  $\vec{H}$  that are needed to numerically calculate this quantity lie on opposite sides of  $E_z$  so that the curl is automatically centered. The currents must be interpolated between cells in order to center them on the electric field that is being calculated. The same is true of the ion densities for the conductivity calculation.

Figure 8 also shows the system used to number the boundaries of the calculational volume. The system of numbering considers three types of boundaries: sides, edges (junction of two sides), and corners (junction of three sides). Side number 1 is the  $X = 0$  plane; side number 2 is the  $X = X_{MAX}$  plane, etc. Thus, the sixth side is at  $Z = Z_{MAX}$ . Edge 13 is at the junction of planes 1 and 3. Corner 136 is at the junction of edge 13 and side 6, or the junction of planes 1, 3, and 6. This may all seem confusing at first, but the system is very easy to remember and facilitates working with the code—either modifying it or setting up a problem.

Four types of physical boundary conditions are used in DAVID. They are listed in Table 4. The variable which denotes the boundary condition type is IBN (NSIDE) in the air and IBNG (NSIDE) in the ground. NSIDE denotes the side number, as described above, and IBN or IBNG take the values 1 through 4, depending on the physical condition desired. Not all sides can assume any of the boundary conditions. Table 5 shows the types of boundary condition that each side was allowed to assume at the time this report was written. The IBM and IBNG arrays are read as input data. What happens when a forbidden value is read in depends upon which side is involved. We will now briefly describe each boundary condition:

1. Perfect Conductor. Tangent electric fields and normal magnetic fields are zeroed. Note that this is redundant, since one implies the other, and the field components are arranged within the cell in such a way that zero tangent electric fields automatically yield zero normal magnetic fields.

Table 4. Types of physical boundary conditions used by DAVID.

IBN/IBNG	Boundary Condition
1	Perfect Conductor
2	TM Symmetry
3	Ground Plane
4	Ambient Air or Ground

Table 5. Types of physical boundary conditions each side is presently allowed to assume.

Side Number	Allowed Values Of	
	IBN	IBNG
1	2	2
2	1, 4	1, 4
3	1, 4	3
4	1, 3, 4	1, 4
5	1, 4	1, 4
6	1, 4	1, 4

2. TM Symmetry. Also known as "mirror symmetry," this boundary condition effectively doubles the size of a problem with a plane of symmetry. In the future it might be useful to give plane 3 that option also. In this boundary condition, the normal derivatives of the tangent electric field is zero, as is the derivative of the transverse magnetic field. In practice, it is easier to set the TE fields equal to zero, which is what is done in DAVID. In order to do this, the boundary must be placed through the center of the cell rather than tangent to a cell face. Particles must also be handled in a special manner. Whenever a particle tries to cross through the symmetry plane, its normal component of velocity is reversed in order to represent a particle coming back through the opposite direction. Special treatment is also required in the current averaging scheme near the symmetry plane, in order to account for the contribution of electrons on the opposite side of the plane.
3. Ground Plane. Special treatment in the calculation of the tangent electric fields at the air/ground interface is required because derivatives of the magnetic field across the boundary are required, and these derivatives are not continuous. We decided to ignore all that and just take the derivatives across the ground plane. Special handling is still required since the vertical grid sizes in the ground are different from the air and because two different coordinate systems are used.
4. Ambient Air/Ground. The ultimate objective of this boundary condition is to simulate the environment that would exist in the absence of an object. The best way

to do this, in the close-in ground-burst problem, is to use a one-dimensional calculation, such as the one used in GLANC<sup>2</sup>. The boundary condition is important, not only for specifying the electromagnetic field, but for the injection of particles so that we do not have the problem of wasting space near the boundary where a sufficient number of particles must build up to accurately represent the current. At this time, DAVID does not handle the boundary condition in this way. It uses an approximation which exploits several characteristics of the close-in ambient field, e.g., the fact that the TE mode fields are zero and that all derivatives in the x-direction are zero. There is the additional assumption that only the radial (direction of the gamma flux) electric field exists on the top, front, and back boundaries (sides 3, 5, and 6). That is also true on the bottom when no ground is present. The x-component of the magnetic field is allowed to exist on the side (side 2), but its x-derivative is zero. The boundary condition is handled somewhat more primitively in the ground.

### 3.2 FIELD EQUATIONS

The two vector field equations solved by DAVID and DAVEJR in SUBROUTINE FIELDS are (Section 2.2 Equations 1 and 2)

$$\frac{\partial \vec{E}}{\partial t} + \frac{\sigma}{\epsilon} \vec{E} = c(\nabla \times \vec{h} - \vec{j})$$

$$\frac{\partial \vec{h}}{\partial t} = -c \nabla \times \vec{E}$$

where the meaning of the variables is given in Section 2.2. For the purpose of this discussion, we will use capital letters instead of lower case

letters for the normalized magnetic field and current, i.e.,  $\vec{h} \rightarrow \vec{H}$  and  $\vec{j} \rightarrow \vec{J}$ . The reader should remember that the quantities are normalized.

Let  $E_u^n(i, j, k)$  be the  $u^{\text{th}}$  component ( $x, y, z$ ) of the electric field evaluated at the  $n^{\text{th}}$  time step and in the cell whose  $x, y$ , and  $z$  coordinates (cell center) are  $[(i-1/2)\Delta x, (j-1/2)\Delta y, (k-1/2)\Delta z]$ . The notation for the H-field is similar. Remember that  $\vec{E}$  and  $\vec{H}$  are evaluated half a time step apart. Thus  $E_u^n$  is half a time step ( $\Delta t/2$ ) later than  $H_u^n$ . Similarly, the positions of the field components are different, even though they are designated by the same  $i, j, k$  indices. In the code, the solution for the electric field occurs earlier in the loop than the magnetic field  $z$  because  $\vec{H}$  is assumed to be zero during the first pass.

The magnetic field equations are center differenced. They are

$$H_x^{n+1}(i, j, k) = H_x^n(i, j, k) + c\Delta t \left[ \frac{E_y^n(i, j, k+1) - E_y^n(i, j, k)}{\Delta z} - \frac{E_z^n(i, j+1, k) - E_z^n(i, j, k)}{\Delta y} \right], \quad (36)$$

$$H_y^{n+1}(i, j, k) = H_y^n(i, j, k) + c\Delta t \left[ \frac{E_z^n(i+1, j, k) - E_z^n(i, j, k)}{\Delta x} - \frac{E_x^n(i, j, k+1) - E_x^n(i, j, k)}{\Delta z} \right], \quad (37)$$

$$H_z^{n+1}(i, j, k) = H_z^n(i, j, k) + c\Delta t \left[ \frac{E_x^n(i, j+1, k) - E_x^n(i, j, k)}{\Delta y} - \frac{E_y^n(i+1, j, k) - E_y^n(i, j, k)}{\Delta x} \right]. \quad (38)$$

The electric field equations are of the form

$$\frac{\partial E_u}{\partial t} + a_u E_u = c f_u(t) . \quad (39)$$

We use the exponential form of solution, which assumes  $a_u(t)$  and  $f_u(t)$  are constant over the time interval  $\Delta t$ , so that

$$E_u^{n+1}(i,j,k) = E_u^n(i,j,k) e^{-a_u^n \Delta t} + f_u^n(c \Delta t) \left[ \frac{1 - e^{-a_u^n \Delta t}}{a_u^n \Delta t} \right], \quad (40)$$

where

$$a_u^n = \frac{\sigma_u^{n+1}}{\epsilon}$$

$$\sigma_u^n = \text{conductivity at location of } E_u^n$$

$$f_u^n = \nabla \times \vec{H}_u^{n+1} \Big|_u - J_u^{n+1} \quad (\text{normalized}) .$$

The driver functions are

$$f_x^n(i,j,k) = \left[ \frac{H_z^{n+1}(i,j,k) - H_z^{n+1}(i,j-1,k)}{\Delta y} - \frac{H_y^{n+1}(i,j,k) - H_y^{n+1}(i,j,k-1)}{\Delta z} \right] - J_x^{n+1}, \quad (41)$$

$$f_y^n(i,j,k) = \left[ \frac{H_x^{n+1}(i,j,k) - H_x^{n+1}(i,j,k-1)}{\Delta z} - \frac{H_z^{n+1}(i,j,k) - H_z^{n+1}(i-1,j,k)}{\Delta x} \right] - J_y^{n+1}, \quad (42)$$

$$f_z^n(i,j,k) = \left[ \frac{H_y^{n+1}(i,j,k) - H_y^{n+1}(i-1,j,k)}{\Delta x} - \frac{H_x^{n+1}(i,j,k) - H_x^{n+1}(i,j-1,k)}{\Delta y} \right] - J_z^{n+1} . \quad (43)$$

The current components are calculated at the cell centers and must be interpolated to find their values at the position of each electric field component. Similarly, the conductivity must be calculated at each E-field position, so that the electron and negative ion densities must be interpolated. We illustrate the procedure for the case of the current components, but the scheme is the same for the ions.

$$J_x^{int} = \frac{1}{2} [J_x(i,j,k) + J_x(i,j-1,k-1)] , \quad (44)$$

$$J_y^{int} = \frac{1}{2} [J_y(i,j,k) + J_y(i-1,j,k-1)] , \quad (45)$$

$$J_z^{int} = \frac{1}{2} [J_z(i,j,k) + J_z(i-1,j-1,k)] . \quad (46)$$

The conductivity calculation, which takes place in the FIELDS routine, is discussed in Section 3.7.

Note the form in which Equation 40 was written. The term in brackets is

$$\left[ \frac{1 - e^{-a_u^n \Delta t}}{a_u^n \Delta t} \right]$$

should mathematically go to the limit of unity as  $a_u^n \Delta t$  goes to zero. This occurs for very low conductivity. In order to allow the code to operate in the limit of zero conductivity (free space propagation) we add a small constant ( $10^{-4}$ ) to the dimensionless quantity  $a_u^n \Delta t$ . This gives us a

numerical result sufficiently close to unity and does not allow the computer to try to divide by zero.

The field equations are differenced over the entire mesh, regardless of the presence of the object. After each field is differenced, we loop back through the mesh and erase the fields within the cells corresponding to the body and the tangential electric or normal magnetic field components on the surface.

Special interpolations are required to obtain the currents and ion densities for the calculation of fields near a boundary because one cannot interpolate through it. In order to avoid having many "IF" checks, DAVID's field subroutine calculates the fields along each side, edge, and corner explicitly. This requires a lot more programming, but by making the decisions beforehand, instead of letting the computer do it, a significant amount of computer time can be saved.

As will be seen in the next section, particles and current averaging near boundaries must also be treated in special ways. For all these reasons, we have assigned a flag to each cell in the mesh. This array is called IBOD for the air cells and IBODG for the ground cells. Each element of the array has the value 0 through 27. A cell whose IBOD (or IBODG) is 0 is not in an object or next to a boundary. A cell whose array element is numbered 1 through 6 has one side near a boundary (the number tells which boundary it is). Cells numbered 7 through 18 have two sides on a boundary (located on an edge). Cells numbered 19 through 26 have three sides adjacent to boundaries (located in corners). Finally, cells with IBOD or IBODG elements equal to 27 are part of the object. Thus, an object is constructed by setting IBOD and IBODG equal to 27 for all the cells which one wishes to use to describe it. The object takes on the appearance of a model built out of blocks. The IBOD numbering system is summarized in Table 6.

Table 6. IBOD/IBODG numbering system.

IBOD/IBODG	Cell Location
0	Away from boundary and object
1 - 6	Next to side
7 - 18	In two-sided edge
19 - 26	In three-sided corner
27	In object

A flow chart showing the electric field calculation is shown in Figure 9. Note that the conductivity is calculated during the electric field calculation (SUBROUTINE FIELDS) and is not stored. The time output code, DAVEOUT, contains a routine to recalculate the conductivity from the ion densities and the electric field. Thus, the outputted conductivity is somewhat different than the value actually used in the E-field calculation.

With the exception of a relatively thin region near the surface, the conductivity of the ground remains constant. It is only within that same layer that currents of significant magnitude exist. In order to speed the calculation somewhat, the ground is divided into two regions. The one near the surface uses a conductivity array and a current array which change in time. This layer is NRY cells deep. The array is two-dimensional; no x-direction variation is allowed. Prescribed sources are used and the gamma flux is attenuated exponentially with slant range. The field equations for the remainder of the grid do not include a time dependent radiation enhanced conductivity or a Compton current term. The subroutine which calculates the ground electric fields is called GELEC and the magnetic field routine is called GMAG. The names of most variables in the ground, including the coordinates, are the same as in the air, except that the letter "G" is added.

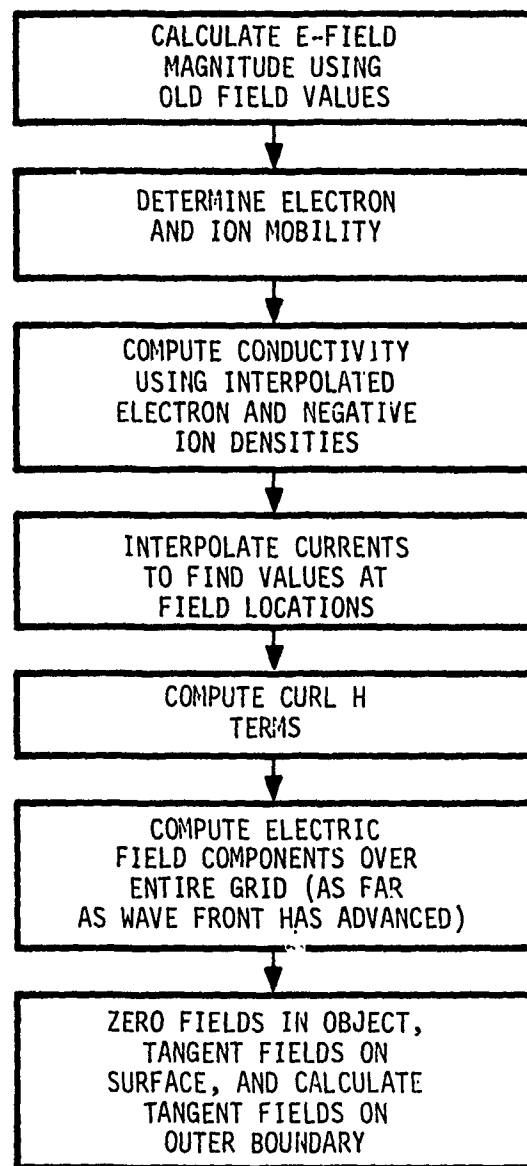


Figure 9. Flow chart of the calculation of electric fields in the air as performed by subroutine fields.

In the future, the code should be modified to allow smaller cells in the radiation deposition layers, than in the remainder of the ground.

A description of the ambient boundary condition, as presently implemented, is in order. See Section 3.1 for definitions and numbering systems. We start with the air calculation.

Plane 1, the TM symmetry plane ( $X = 0$ ), runs through the center of the first cells ( $I = 1$ ). Thus, the field components  $EX(1,J,K)$ ,  $HY(1,J,K)$ , and  $HZ(1,J,K)$  are located on the plane and are equal to zero. The TM fields in these cells are set equal to the fields in the next cell in the x-direction, i.e.,  $EY(1,J,K) = EY(2,J,K)$ ,  $EZ(1,J,K) = EZ(2,J,K)$ , and  $HX(1,J,K) = HX(2,J,K)$ .

The fields on plane 2,  $X = XMAX$  ( $I = NX$ ), are calculated using the full field equations for  $EY(NX,J,K)$  and  $EZ(NX,J,K)$ , except that partial derivatives with respect to  $X$  are assumed to be zero.

On the top plane, plane 3 ( $Y = 0$  and  $J = 1$ ),  $EX(I,1,K) = 0$ ,  $HY(I,1,K) = 0$  and  $EZ(I,1,K)$  are calculated as components of the radial electric field (curl  $H$  terms zero). We impose the condition that  $EZ$  has no variation in the x-direction by calculating  $EZ(2,1,K)$  and using this value for  $I \geq 2$ .

The calculation at plane 4 ( $Y = YMAX$ ,  $J = NY$ ) is the same, if the ambient boundary condition is used. An air/ground interface may also be used, in which case we difference across the ground plane using magnetic fields from the ground field array.

On planes 5 and 6 ( $Z = 0$ ,  $ZMAX$  and  $K = 1$ ,  $NZ$ )  $EX$  is identically zero and  $EY(I,J,1)$  and  $EY(I,J,NZ)$  are calculated components of the radial electric field. As on plane 3, the x-variation is set equal to zero by calculating  $EY(2,J,1$  or  $NZ)$  and using this value for  $I \geq 2$ .

The ambient boundary conditions in the ground are somewhat different because there is no dominant radial electric field. The symmetry plane (plane 1) is treated exactly as it is in the air. The  $EZG(NX,J,K)$  and  $EYG(NX,J,K)$  fields on plane 2 are set equal to those just inside the boundary ( $I = NX-1$ ). The fields on plane 3, the air/ground interface are set equal to those in the air, i.e.,  $EXG(I,1,K) = EX(I,NY,K)$ ,  $EZG(I,1,K) = EZ(I,NY,K)$ ,  $HYG(I,1,K) = HY(I,NY,K)$ .

On planes 4, 5, and 6, a constant of proportionality is used to determine the fields on the boundary from values inside the mesh. The constant, called GUESS, is currently set equal to 0.9. If it were set to 0., it would be equivalent to an infinite conductor boundary condition. The use of GUESS supplements the requirements that partials with respect to  $x$  are zero and that  $EXG$ ,  $HYG$ , and  $HZG$  are zero on the boundary. For example, on plane 5 we have  $EXG(I,J,1) = 0$ . For  $I = 2$ , we set  $EYG(2,J,1) = GUESS * EYG(2,J,2)$  and  $EZG(2,J,1) = GUESS * EZG(2,J,2)$ . Then, to maintain zero derivative in the  $x$ -direction, we set  $EYG(I,J,1) = EYG(2,J,1)$  and  $EZG(I,J,1) = EZG(2,J,1)$  for  $I > 2$ .

### 3.3 MOMENTUM EQUATIONS AND AVERAGING TECHNIQUE

The particle calculation is the most complicated of all those performed by DAVID and forms the main part of the code. The flow of the computation is shown in Figure 10.

The process starts with the injection of new particles in alternating cells, like a 3-D checkerboard. The user can choose whether he wants to inject each time step or to skip one or more. The input variable INCINJ does this ( $INCINJ = 1$  injects every time step). In order to help smooth the current distribution, the cells in which injection occurs alternate each injection time. For example, if injection occurred in the 1<sup>st</sup>, 3<sup>rd</sup>, 5<sup>th</sup>, etc., cells in the  $x$ -direction during the first time, the 2<sup>nd</sup>, 4<sup>th</sup>, 6<sup>th</sup>, etc., cells would be injected during the second time.

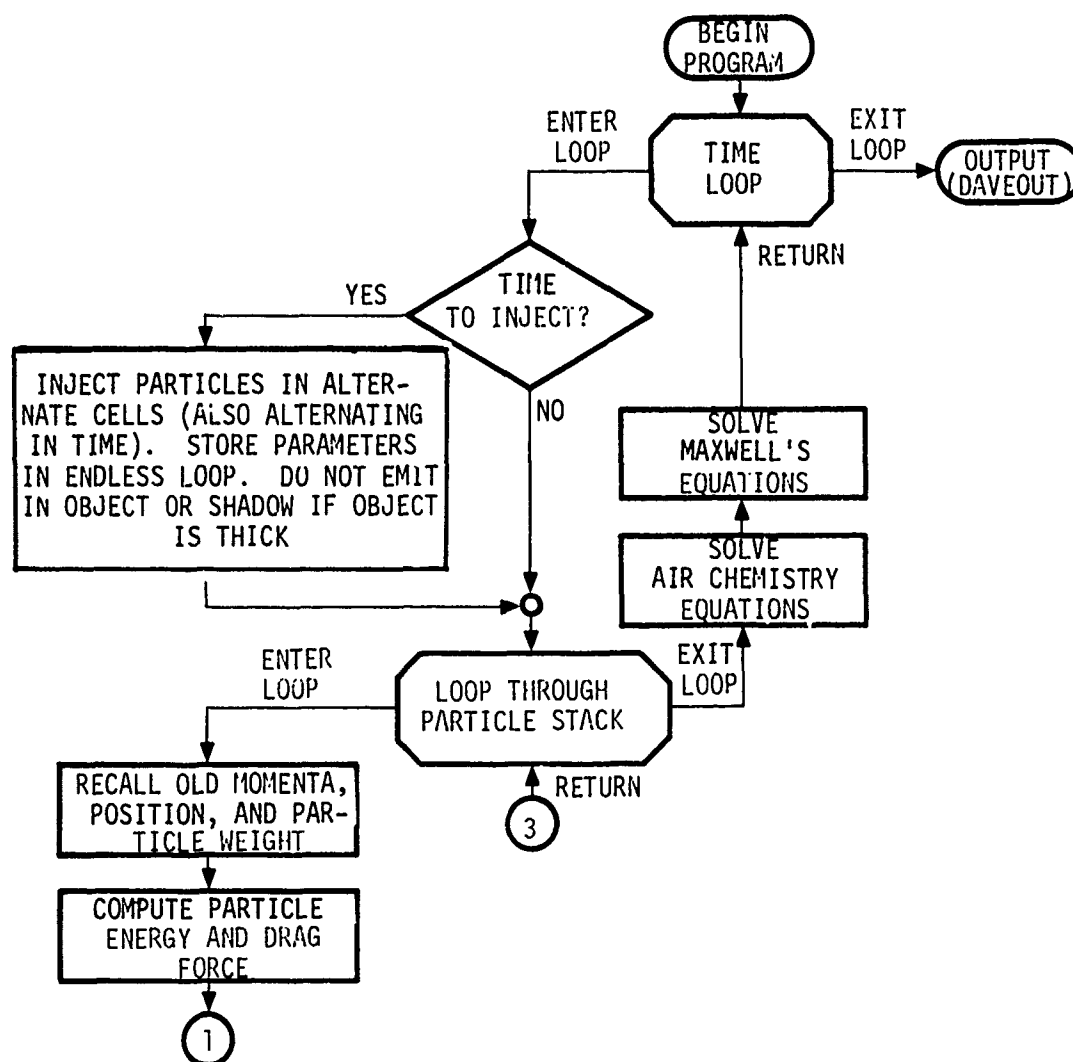


Figure 10. Flow chart showing the particle motion and current/ionization rate calculation.

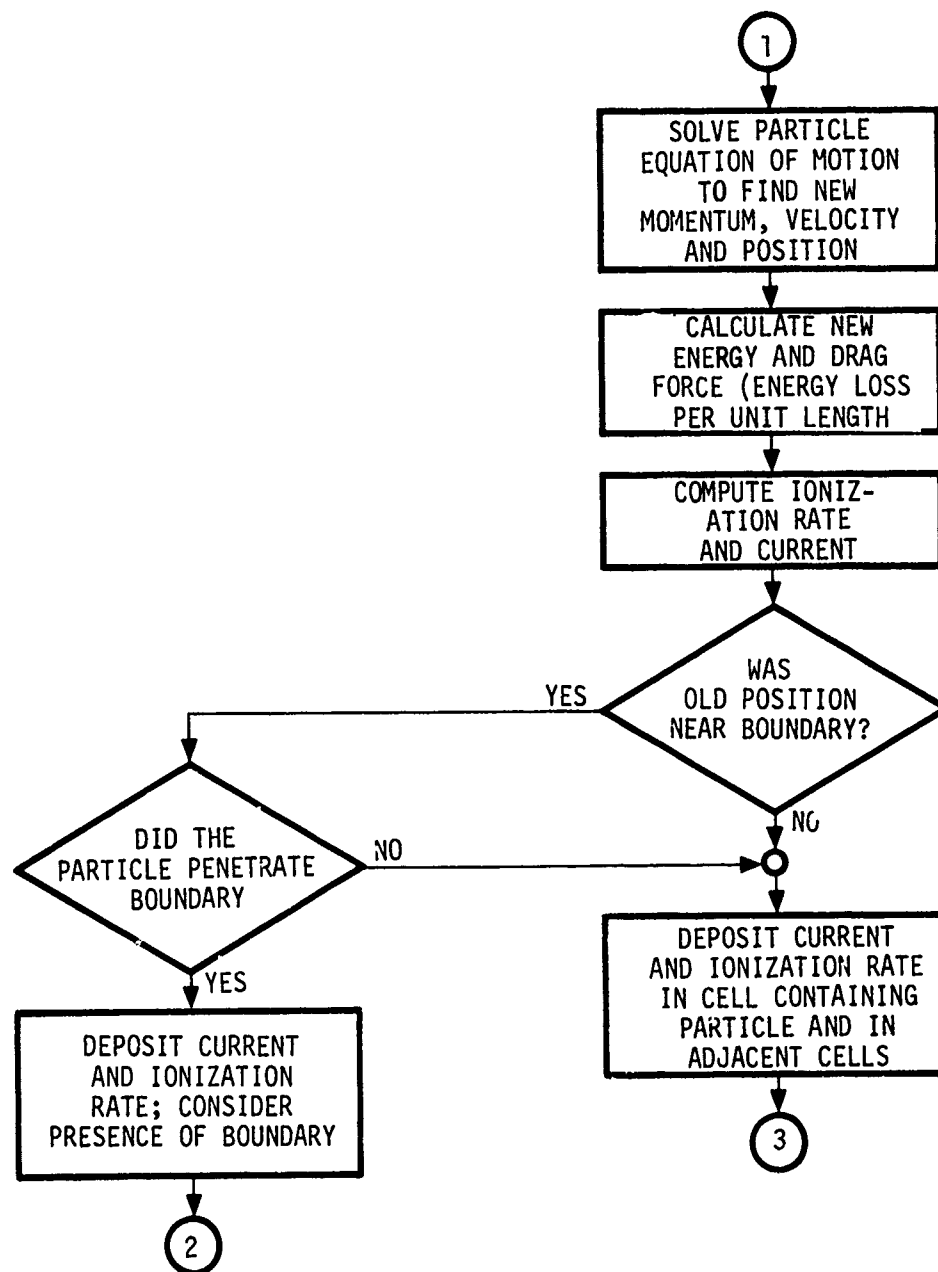


Figure 10 (continued).

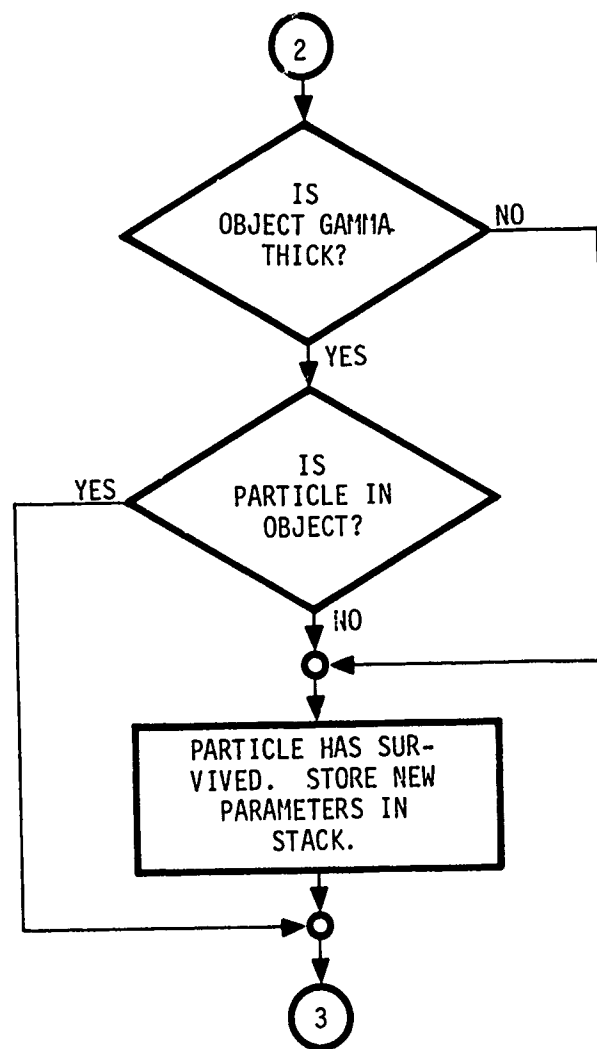


Figure 10 (continued).

Seven quantities are stored in the array PRW(M,N) for each particle. Here M is the number of the quantity ( $1 \leq M \leq 7$ ) and N is the number of the particle. The quantities, numbered 1 through 7 are: PX(x-momentum), PY(y-momentum), PZ(z-momentum), X(x-position), Y(y-position), Z(z-position), and W(particle weight). The initial position of the particle is the center of the cell in which it is injected. The initial kinetic energy of the particle is given by Equation 15 and its momentum is then calculated by Equation 16. The particle weight is given by Equation 9.

The PRW array is circular. When the last particle is entered (4000 are currently allowed), the code writes over the first ones until all new particles are entered. The first ones are usually the older ones. When particles die, the surviving ones are pushed up the stack so that new ones can be entered below. It is only when new ones can no longer be entered there that we replace the old ones at the top. It is not foolproof, but it seems to be the best of the simple schemes.

When the object has been designated as gamma thin (IBLACK = 0), particles are injected everywhere, including the cells inside the pole. They are also allowed to travel through the pole when born outside of it.

If the object is gamma thick (IBLACK = 1) no particles can be born in it or in its shadow. An array called SHADO (I,J,K) in the air and SHADG (I,J,K) in the ground contain a shadow factor for each cell. The shadow factors are calculated in SUBROUTINE SETUP from the object description and the incidence angle of the gamma rays. If the center of the cell is within the shadow, the entire cell is considered to be within the shadow. Ordinarily, the shadow factor either has the value 0 or 1. The value 0 means the cell is completely shadowed and the value 1 means that it is not. When the ambient boundary condition is used, we gradually increase the shadow factor for cells near the boundary which would otherwise be shadowed. If we did not, there would be a contradiction, since a shadow could not exist in the ambient environment. The integer KSTP determines the number of cells over which the shadow will be faded. It is presently set to 3 so that the cell

next to the wall has the value 0.666... and the next one has the value 0.333 and the third one is zero. When the shadow factors value is between 0 and 1, it is used to multiply the particle weight.

Particles are not injected until the incident gamma wave front passes through the cell center. Since the  $\gamma$  waveform rises exponentially from  $t = -\infty$ , we include all of the charge that would be generated over that time period in the weight of the first particle.

After injection, the particle momentum calculation begins. Currents are not calculated until the particle has been affected by drag and fields. Starting with the first particle in the stack, the old electron energy (EE) is calculated using Equation 5. This allows the calculation of the drag force (Equations 4 and 3). The indices of the cell (ICELL, JCELL, and KCELL) are computed from the x, y, and z coordinates. The electric and magnetic fields at the center of the cell are computed by interpolation. Then, the momentum Equation 3 is integrated, using the old value of momentum on the right-hand side in the drag term.

The equations for the three components of momentum can be put in the form of Equation 39 and the exponential form of solution used. This is useful at low altitudes where the drag term is significant. As an example, we write the solution for the x-component of momentum

$$PX^{n+1} = PX^n e^{-A_c} - eF_x \Delta t \left( \frac{1 - e^{-A_c}}{A_c} \right), \quad (47)$$

where we are calculating PX at the  $(n+1)^{th}$  time step and where

$e$  = electron charge

$\Delta t$  = time increment

$$A_c = \frac{dE}{dR} \frac{\Delta t}{P}$$

P = old momentum magnitude

$$F_x = EX + \frac{PY \cdot HZ - PZ \cdot HY}{\sqrt{P^2 + (mc)^2}}$$

HZ, HY = interpolated magnetic field (z and y components)  
(volts/m)

EX = interpolated electric field (x-component)

m = electron rest mass

c = speed of light.

When the new momentum components are computed, the new velocities can be found using Equation 3a, and then the new position can also be computed.

If the particle has penetrated the symmetry plane, its x-momentum is reversed and it is placed an equal distance on this side of the plane (plane 1).

The charge density (QDEN) is calculated from W, and the three components of current are determined as the products of it and the velocity components. The new energy is then computed and the ionization rate (S) figured from Equation 17.

DAVID then determines whether the old position of the particle was near a boundary wall. This is done by inspecting IBOD (ICELL, JCELL, KCELL). If the particle was in the cell near a boundary before moving this time ( $1 \leq IBOD \leq 26$ ) it may have penetrated and must be killed after its current has been spread in a manner appropriate to that particular boundary. Most particles will not be in one of those cells and one should not waste time by dropping out of the loop or doing special checks. That is why the IBOD array is used. If IBOD = 0 or 27 the particle was clear or in a pole away from the boundary (transparent pole only, since the particle would already have been killed if it had run into a thick pole). If IBOD

does not have these values, we drop out of the loop. A 26 position computed GO TO uses the value of IBOD (ICELL, JCELL, KCELL) to send the pointer to the part of the program that will handle the particle at the particular side, edge, or corner. Ordinarily, the code will enter directly into the current smearing phase.

Because constant spatial step sizes are used, a rather unsophisticated averaging scheme can be used to smear the current and ionization rate in space; one does not have to remember what the volume of the cell was that the particle was born in. Each particle represents electrons that were born in two cells, since they are injected in alternating cells. Therefore, we count the current (and ionization rate) contribution of each particle twice. If the current due to a single particle is  $\vec{J}$ , for example, we assign this value to the cell in which the particle stops at the end of a time step. In addition, the particle contributes an amount  $\frac{1}{6} \vec{J}$  to the current in the six adjacent cells. Between this spreading and the alternation of injected cells, a very smooth distribution in both space and time can be achieved, even when we inject every other time cycle.

Problems arise near boundaries because of the lack of particles to make their  $1/6^{\text{th}}$  contribution. This is partially compensated by allowing a particle to penetrate the boundary and spread its charge back before killing it. The same is true when a particle enters a gamma thick pole. They are not killed at all when they enter a gamma thin pole.

An additional problem arises near the top and front boundaries, where the gamma rays enter the box. Without a particle injecting boundary condition, we must allow a reasonable distance for the particle distribution to build up. For gamma energies of about 1.5 or 2 MeV, a reasonable distance is 1.2 meters. This is illustrated in Figure 11. Here we plot the spatial distribution of the horizontal current parallel to the gamma flux ( $J_z$ ) as a function of  $z$ . The time is during the period when the flux is

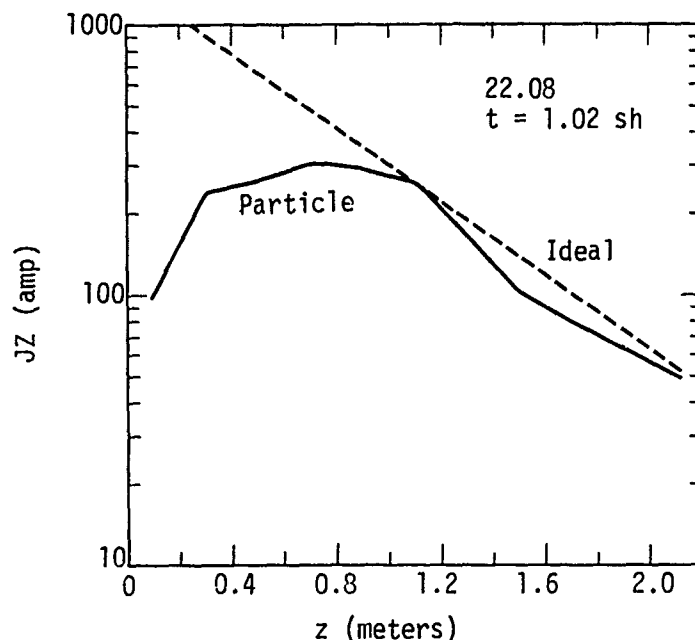


Figure 11. Comparison between current distribution calculated with particles and ideal distribution in direction parallel to ground and flux. Time is during rise of pulse. Magnitude of "ideal" distribution is normalized.

rising exponentially. The dashed line indicates the manner in which the current should be falling as a function of  $z$  (it is normalized and is not meant to show that the magnitude of the current is close to the "real" magnitude). Note the way in which the current builds up as we move away from the front boundary. The flux angle of incidence is  $20^\circ$  from the horizontal, so there is a similar problem as we move downward from the top boundary; however, the buildup occurs over a distance of only 0.4 meters, in this case, because of the shallow incidence angle.

The fields predicted in this region are complicated by the fact that a radiated field generated by the air/ground interface is also building up.

### 3.4 AIR CHEMISTRY EQUATIONS

From Section 2.7, the air chemistry equations solved by DAVID and DAVEJR are

$$\frac{dn_e}{dt} = S_e - (\beta + G)n_e - \alpha n_+ n_e, \quad (48)$$

$$\frac{dn_-}{dt} = \beta n_e - \Gamma n_+ n_-, \quad (49)$$

$$n_+ = n_e + n_-, \quad (50)$$

where

$n_e$  = electron density

$n_-$  = negative ion density

$n_+$  = positive ion density

$S_e$  = ionization rate

$\beta$  = electron attachment rate

$G$  = electron avalanching rate

$\alpha$  = electron-ion recombination rate

$\Gamma$  = ion-ion recombination rate.

These equations are solved in a manner that is more sophisticated and time consuming than necessary, but is consistent with the exponential solution used in the field and momentum equations. This will allow the code to use larger time steps, when other factors allow, than could be used with simple differencing.

Let  $\beta_T = \beta - G$ . Then eliminating the positive ion density from Equations 48 and 49, we have the following two equations to solve

$$\frac{dn_e}{dt} + (\beta_T + \alpha n_-)n_e + \alpha n_e^2 = S_e, \quad (51)$$

$$\frac{dn_-}{dt} + (\gamma n_e)n_- + \Gamma n_-^2 = \beta n_e. \quad (52)$$

These equations are both of the form

$$\frac{df}{dt} + Bf + Af^2 = -D. \quad (53)$$

The solution of this equation is given by integrating the expression

$$\frac{df}{Af^2 + Bf + D} = -dt.$$

Now

$$\int \frac{df}{Af^2 + Bf + D} = \begin{cases} \frac{1}{\sqrt{q}} \log \frac{2Af + B - \sqrt{q}}{2Af + B + \sqrt{q}}, & q > 0 \\ \frac{1}{\sqrt{-q}} \tan^{-1} \frac{2Af + B}{\sqrt{-q}}, & q < 0 \end{cases} \quad (54)$$

where  $q = B^2 - 4AD$ . Now  $D < 0$ , so that  $q \geq 0$ . Using  $d = -D$ ,  $q = B^2 + 4Ad$  and

$$\frac{2Af + B - \sqrt{q}}{2Af + B + \sqrt{q}} = K_0 e^{-\sqrt{q} t}. \quad (55)$$

We assume that the drivers ( $S_e$  and  $\beta n_e = d$ ) are constant over a time step  $\Delta t$ . Let  $f_0$  be the value of  $f$  just before the new interaction. Then

$$f = \frac{\left(\frac{B + \sqrt{q}}{2A}\right) K_0 e^{-\sqrt{q} \Delta t} - \left(\frac{B - \sqrt{q}}{2A}\right)}{1 - K_0 e^{-\sqrt{q} \Delta t}}, \quad (56)$$

where  $K_0 = (2Af_0 + B - \sqrt{q}) / (2Af_0 + B + \sqrt{q})$ . Multiplying numerator and denominator by  $2A$ , yields the form used in SUBROUTINE AIRCHEM:

$$f = \frac{(\sqrt{q} + B)K_0 e^{-\sqrt{q}\Delta t} + (\sqrt{q} - B)}{2A(1 - K_0 e^{-\sqrt{q}\Delta t})} \quad (57)$$

Table 7 shows how these variables relate to the air chemistry quantities.

It should be noted that because of numerical difficulties in the limit of small electron-ion densities, the density arrays must be seeded with an initial value of  $10^6 \text{ m}^{-3}$  ( $1 \text{ cm}^{-3}$ ). A larger value may be needed with computers carrying fewer significant figures than the CDC 7600 (60 bit word). This point is not very important, since we initialize the densities the first time that they are calculated in a cell and these initialized values are generally in excess of  $10^6 \text{ m}^{-3}$ .

The initialization of the electron and ion densities takes advantage of the fact that the source is rising exponentially from  $t = -\infty$ . It also assumes that only attachment is important. The initial values are

Table 7. Relationship between general equation variables and the specific air chemistry quantities (variables in parentheses are names used in SUBROUTINE AIRCHEM).

Generalized Quantity	Electron Equation	Negative Ion Equation
$f$	$n_e(\text{NE}(\text{I}, \text{J}, \text{K}))$	$n_-(\text{NM}(\text{I}, \text{J}, \text{R}))$
$A$	$\alpha(\text{ALPHA})$	$\Gamma(\text{GAM})$
$B$	$\beta_T + \alpha n_-$	$\Gamma n_e$
$d$	$S_e(\text{S}(\text{I}, \text{J}, \text{K}))$	$\beta n_e(\text{BETA} * \text{NE}(\text{I}, \text{J}, \text{K}))$

$$n_e^0 = \frac{S_e}{\beta + b} , \quad (58)$$

$$n_-^0 = \beta n_e^0 / b , \quad (59)$$

where  $b$  is the e-fold rate of the rising  $\dot{\gamma}$  curve ( $\dot{\gamma} \sim e^{bt}$ ) and  $S_e$  is the first value of the ionization rate calculated by the particle routine.

In AIRCHEM, the electron equation is solved first and the average value of the new and old electron density is used in the driver function for the negative ion density.

## SECTION 4

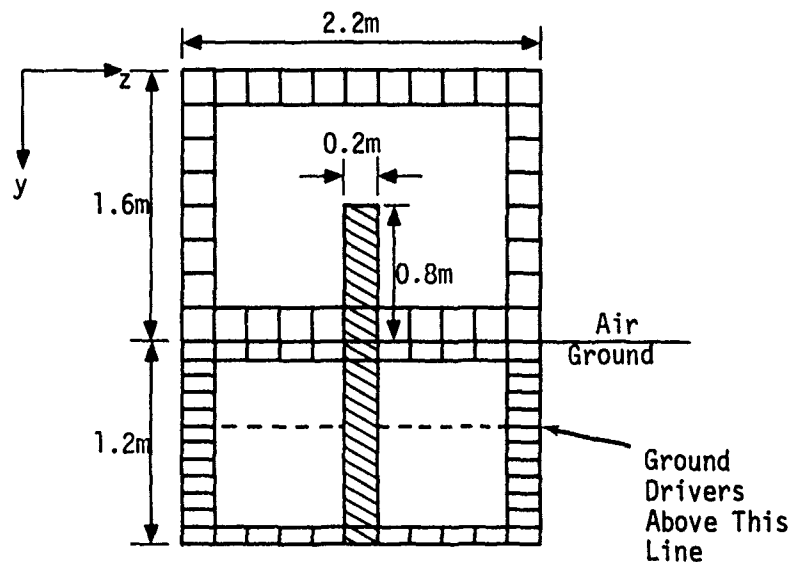
### NUMERICAL RESULTS

In this section we will review some of the numerical calculations that were used to verify the operation of DAVID and DAVEJR. Many tests were made with the individual subroutines before they were placed in the main program. The results shown here are a sampling of those which were made when the codes were fully assembled.

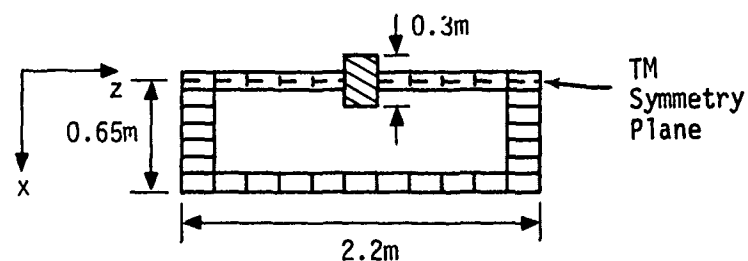
When discussing the calculations, we will have occasion to refer to two sets of fields: transverse magnetic (TM) and transverse electric (TE). The TM fields ( $E_y$ ,  $E_z$ , and  $H_x$ ) are those which would exist in the absence of any object in the mesh. The TE fields ( $E_x$ ,  $H_y$ , and  $H_z$ ) are generated by the object. Ideally, they are zero in the absence of the object and form a very sensitive test of how well boundary conditions and other aspects of the computation are going. One must be careful when looking at parameter studies of TE field behavior because they often grossly exaggerate small problems.

#### 4.1 EX STUDY

A series of investigations was made to look at the contours of  $E_x$  on the air/ground interface. Parameters that were varied are (1) the presence and absence of a pole, (2) the angle of incidence ( $0^\circ$  and  $20^\circ$ ) and (3) the use of the ambient boundary condition compared to a perfectly conducting outer boundary. The geometry and dimensions of the problem are shown in Figure 12. There are seven 0.1 m cells within the mesh in the x-direction ( $NX = 8$ ) and eleven 0.2 m cells in the z-direction ( $NZ = 12$ ). In the air, the vertical step size is 0.2 m ( $NY = 9$ ) while in the ground the vertical step size is 0.1 m



a. Side View



b. Top View

Figure 12. Geometry used in EX study (only cells near boundary are shown).

(NYC = 13). Ground drivers are used in the first five layers of ground (NRY = 5). DAVEJR was used for these calculations.

The pole is four cells high in the air (0.8 m) and reaches down to a perfectly conducting plate at the bottom of the ground mesh (1.2 m). It is one cell wide in the z-direction (0.2 m). Including its image on the opposite side of the TM symmetry plane, the pole is three cells wide (0.3 m)

in the x-direction. Remember that the symmetry plane passes halfway through the first cell.

If the current on the pole was vertical and evenly distributed around its circumference, the  $E_x$  field that we would expect to see would be the x-component of a radial electric field caused by the accumulation of charge along the pole.  $E_x$  would then peak in the x-direction and go to zero in the  $\pm z$  direction, behaving as  $\cos\phi$  in between, where  $\phi$  is measured from the x-axis.

If the pole current flows around the pole from front to rear ( $-z$  to  $+z$ ), we would expect a distribution of  $E_x$  which is zero in both the  $z$ - and  $x$ -directions. It would be negative in one quadrant and positive in the other (looking at just one side of the symmetry plane). If the pole has a circular cross section, the peaks would occur at  $\phi = \pm 45^\circ$ , but with a rectangular cross section, the distribution will be shifted.

The figures that follow, show contours of constant  $E_x$  computed at the air-ground interface. They were hand drawn from printed data and so are not very accurate. The general distributions should be representative, however. All of the figures have one error, which does not affect our analysis. The contours are drawn in such a way that the field goes to zero at the side of the pole.  $E_x$  does not do this, of course, but should appear to emanate from here ( $+x$  side). It does go to zero on the front and back ( $-z$  and  $+z$  sides).

Figures 13a - 13d show the  $E_x$  contours which are generated when the pole is excited by a source incident horizontally ( $\theta = 0^\circ$ ). The peak dose rate is  $10^{13}$  rad/sec and peaks near  $4 \times 10^{-8}$  second. The contours are shown at  $5 \times 10^{-9}$ ,  $5.8 \times 10^{-9}$ ,  $9.8 \times 10^{-9}$ , and  $2.9 \times 10^{-8}$  second. The ground conductivity is  $10^{-2}$  mho/m. The "ambient" boundary condition is used (see Section 3.1). The field contours are clearly characteristic of a current running around the side of the pole at early times (Figures 13a,b). Note that

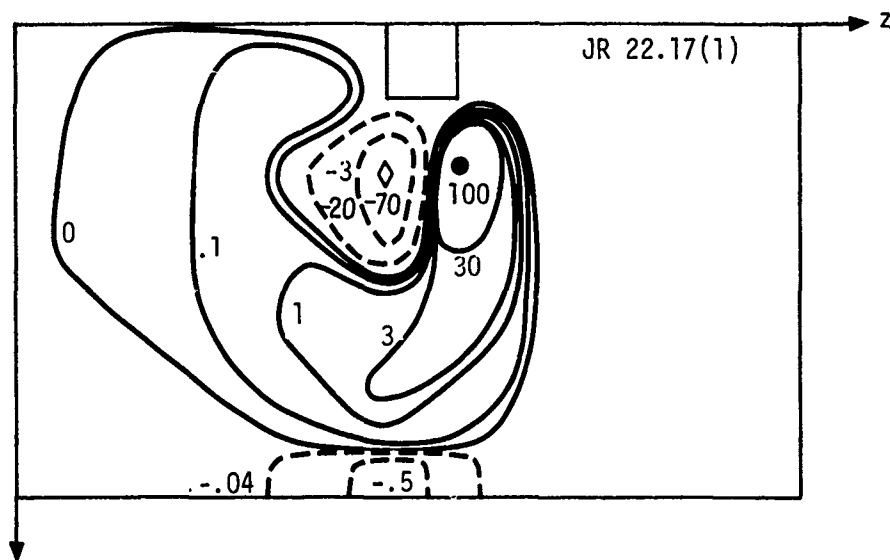


Figure 13a. Approximate contours of constant  $E_x$  at  $T = 5.0E-9$  sec. (Ambient boundary condition,  $\theta = 0^\circ$ ,  $Y = Y_{MAX}$ ).

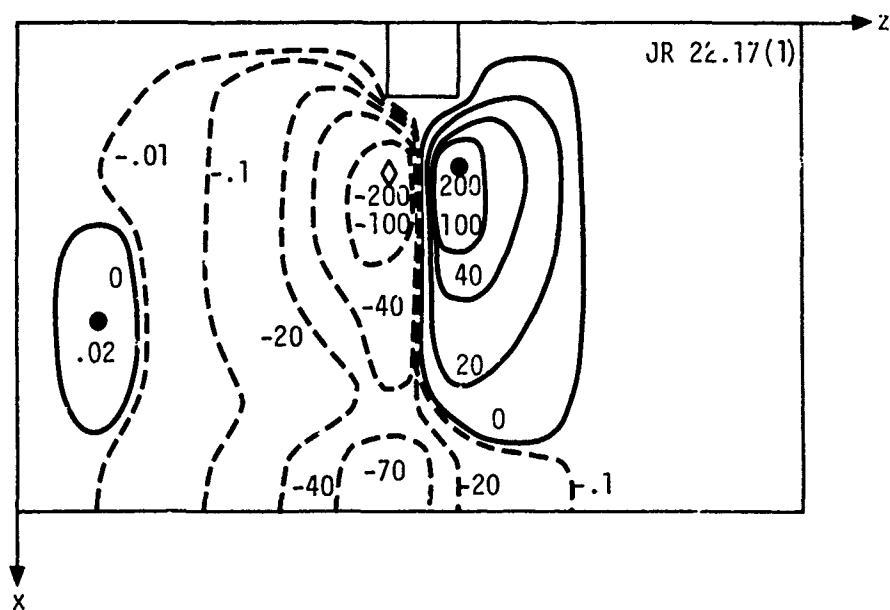


Figure 13b. Approximate contours of constant  $E_x$  at  $T = 5.8E-9$  sec. (Ambient boundary condition,  $\theta = 0^\circ$ ,  $Y = Y_{MAX}$ ).

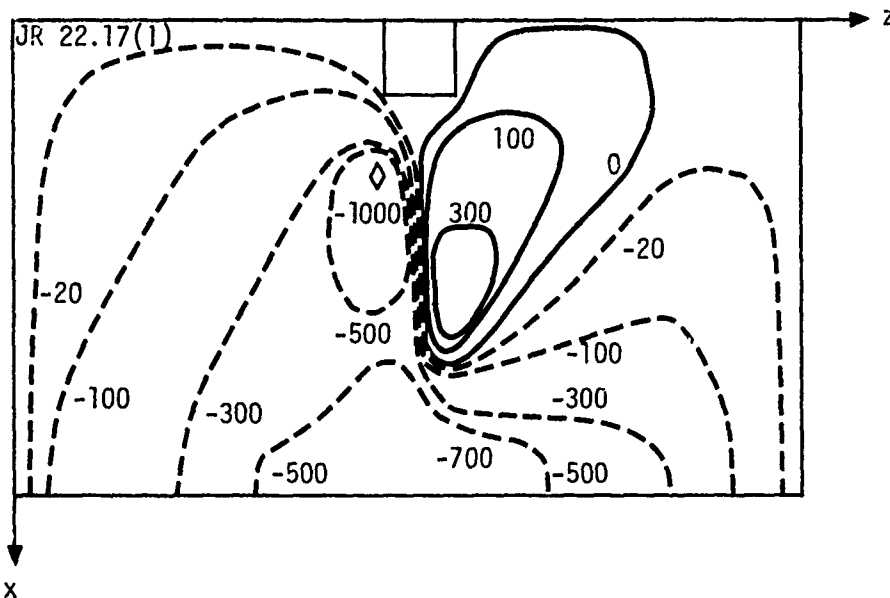


Figure 13c. Approximate contours of constant  $E_x$  at  $T = 9.8E-9$  sec.  
(Ambient boundary condition,  $\theta = 0^\circ$ ,  $Y = Y_{MAX}$ ).

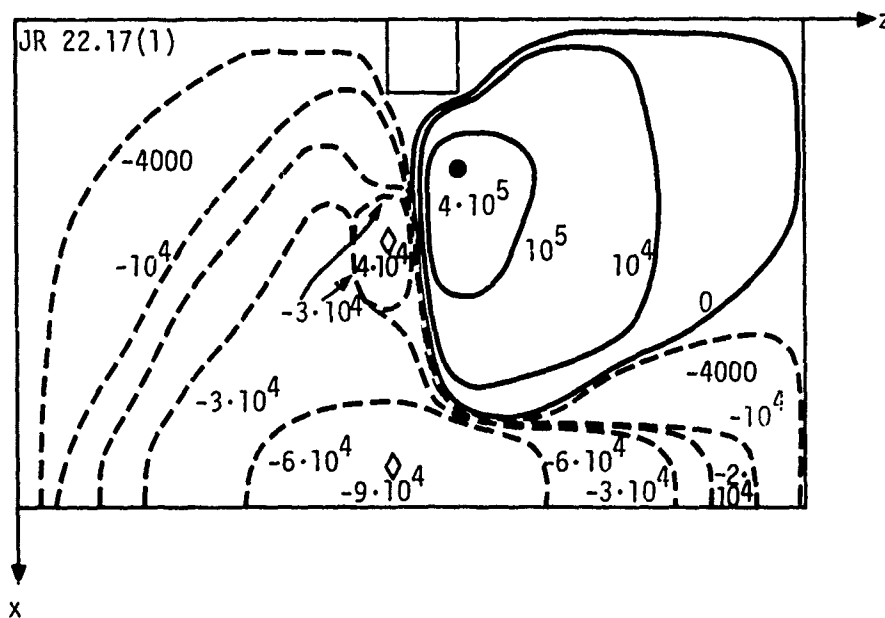


Figure 13d. Approximate contours of constant  $E_x$  at  $T = 2.9E-8$  sec  
(Ambient boundary condition,  $\theta = 0^\circ$ ,  $Y = Y_{MAX}$ ).

the contours are labeled in units of volts/meter. The numbers in the upper corners, i.e., JR22.17(1) in this case, denote the computer run number so that we can refer to it in the future. At later times (Figure 13c,d), the negative fields generated near the outer x boundary begin to influence the fields near the pole. The influence is not great enough to seriously alter the calculation of currents on the pole. Another effect becomes perceptible. The distribution shifts to the left indicating the influence of a net charge accumulation near the ground.

In Figure 14, we show the fields generated when the gammas are incident at an angle of  $20^\circ$ . Figures 14 a and 14b are at the same times as Figures 13c and 13d. In this case, the presence of a charge on the pole, caused by a net vertical flow of current, is quite obvious. The positive field contours are barely influenced by the outer boundary and are shifted "downstream" by the added contribution due to the current flowing around the circumference. The "downstream shift" is even more obvious when the pole is gamma thick (opaque to gamma rays), as is seen in Figure 15.

The effect of using perfectly conducting walls, instead of the "ambient" boundary condition is shown in Figure 16. The positive fields generated by the pole are now confined to a small region near the pole. The influence on the pole currents is not as strong as might be indicated by the  $E_x$  contours, but is still significant with the boundaries this close. The variation of  $H_x$  in the z-direction, under the influence of both the ambient and conducting boundary conditions is shown in Figure 17.

Figure 18 shows the  $E_x$  contours which are generated by DAVEJR in the absence of a pole, for comparison with the previous figures. In the region of the pole location, the fields are generally negligible.  $E_x$  should not exist at all. Closer inspection of the computer data shows that it is generated mainly by the poor outer boundary condition in the ground; it

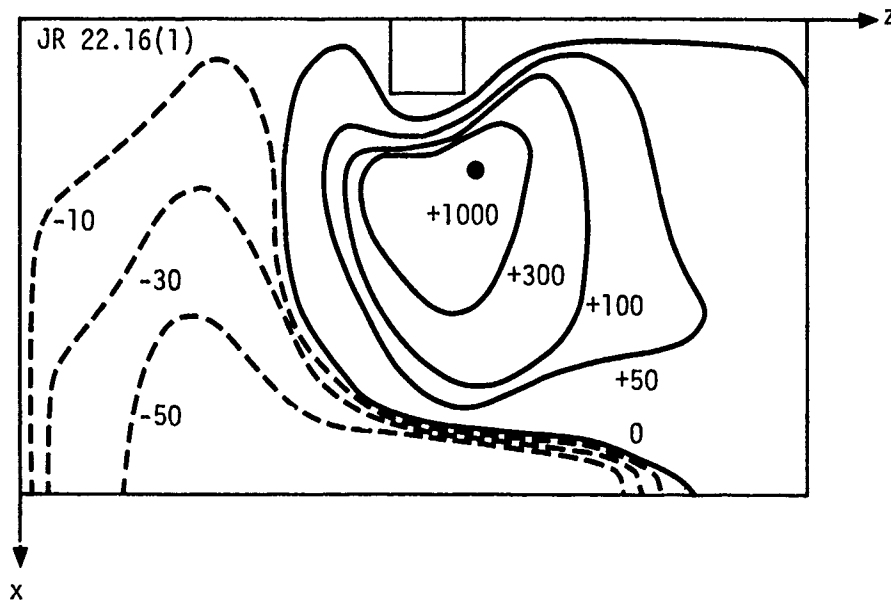


Figure 14a. Approximate contours of constant  $E_x$  at  $T = 9.8E-9$  sec.  
(Ambient boundary condition,  $\theta = 20^\circ$ ,  $Y = Y_{MAX}$ ).

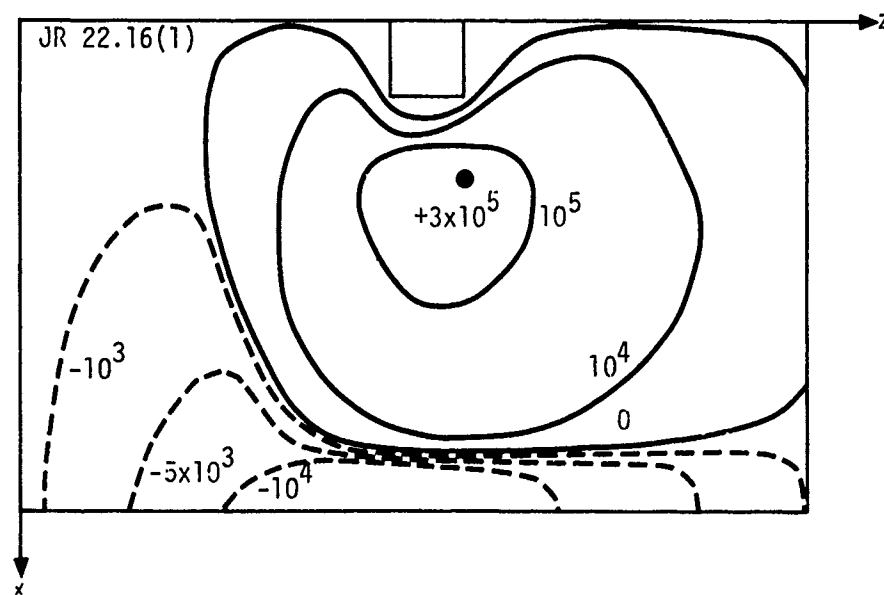


Figure 14b. Approximate contours of constant  $E_x$  at  $T = 2.90E-8$  sec.  
(Ambient boundary condition,  $\theta = 20^\circ$ ,  $Y = Y_{MAX}$ ).

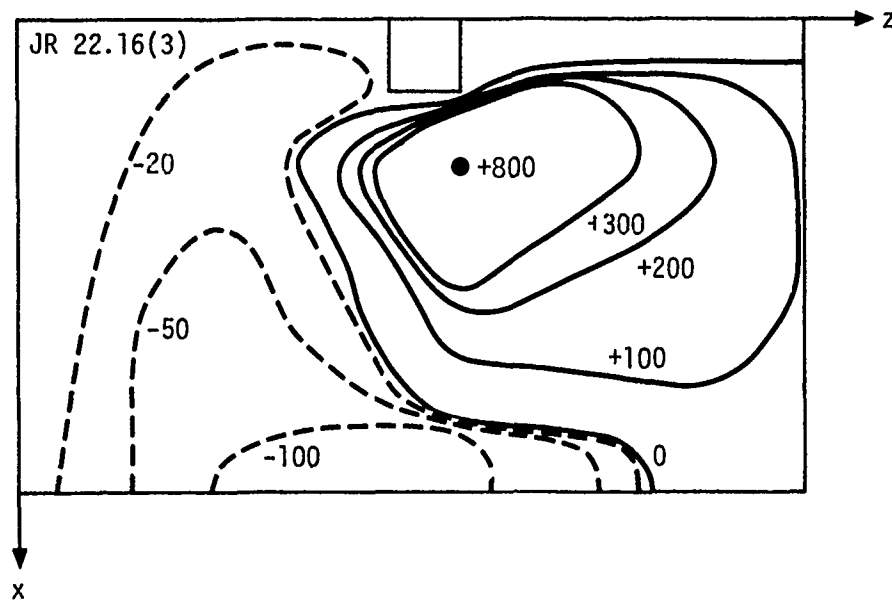


Figure 15a. Approximate contours of constant  $E_x$  at  $T = 9.8E-9$  sec. (Ambient boundary with shadow,  $\theta = 20^\circ$ ,  $Y = Y_{MAX}$ ).

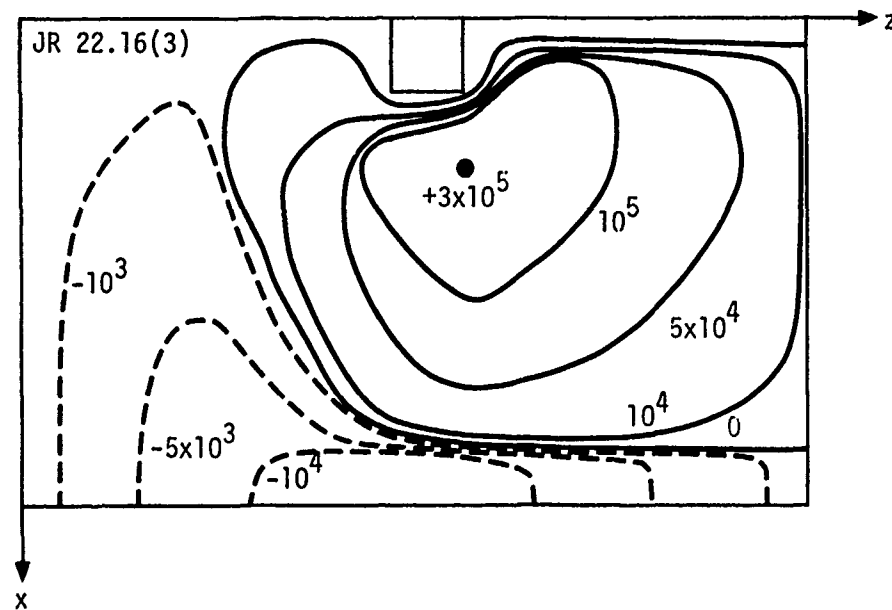


Figure 15b. Approximate contours of constant  $E_x$  at  $T = 2.9E-8$  sec. (Ambient boundary, with shadow,  $\theta = 20^\circ$ ,  $Y = Y_{MAX}$ ).

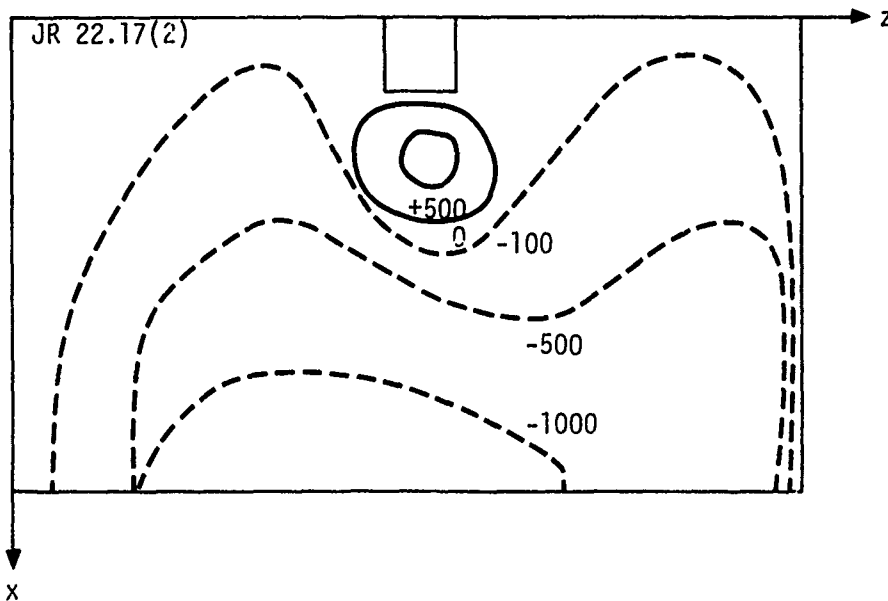


Figure 16a. Approximate contours of constant  $E_x$  at  $T = 9.8E-9$  sec.  
(Perfect conductor boundary condition,  $\theta = 20^\circ$ ,  $Y = Y_{MAX}$ ).

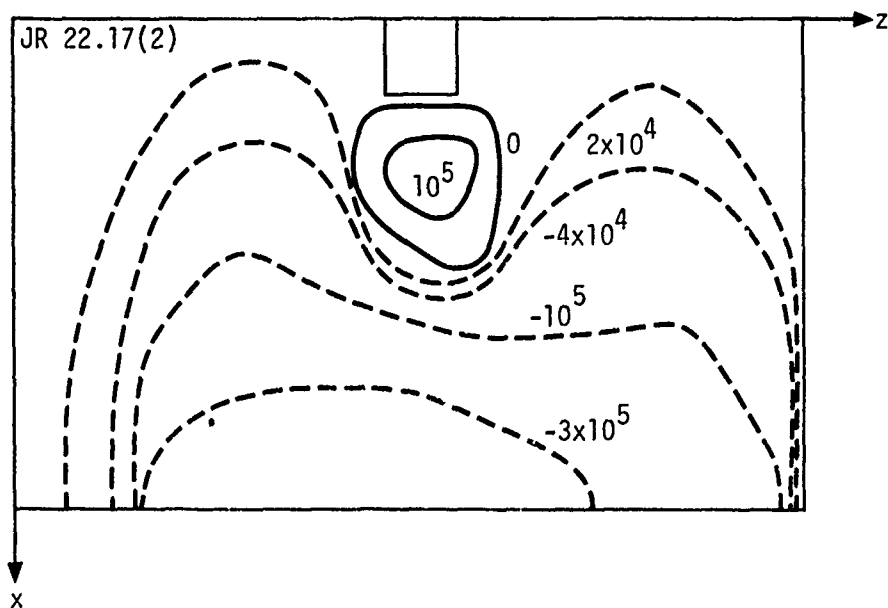


Figure 16b. Approximate contours of constant  $E_x$  at  $T = 2.90E-3$  sec.  
(Perfect conductor boundary condition,  $\theta = 20^\circ$ ,  $Y = Y_{MAX}$ ).

decreases as we look higher in the air. In fact, very large TE fields are generated deep in the ground. These are still small compared to the TM fields, but influence them in a non-negligible manner. More work should be done on improving the ambient boundary condition in the ground.

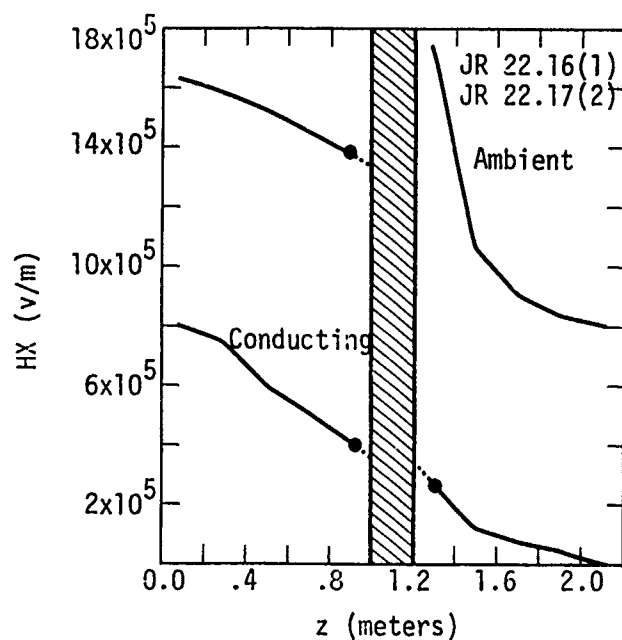


Figure 17. Variation of HX in the vicinity of the pole, comparing the field seen with the ambient boundary condition and the perfectly conducting boundary condition. The variation is along a line 0.1m above the ground and passing through the pole in the z-direction.

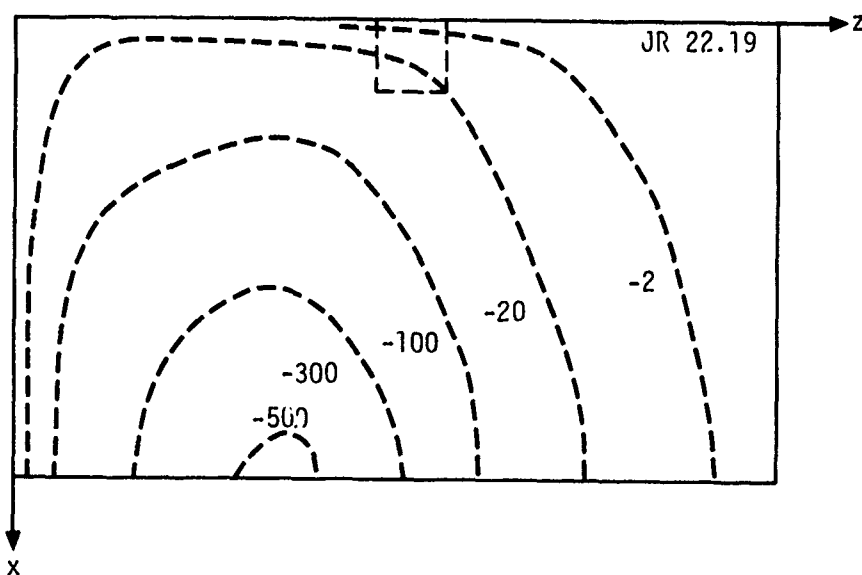


Figure 18a. Approximate contours of constant  $E_x$  at  $T = 9.8E-9$  sec.  
(Ambient boundary condition,  $\theta = 20^\circ$ ,  $Y = Y_{MAX}$ , no pole).

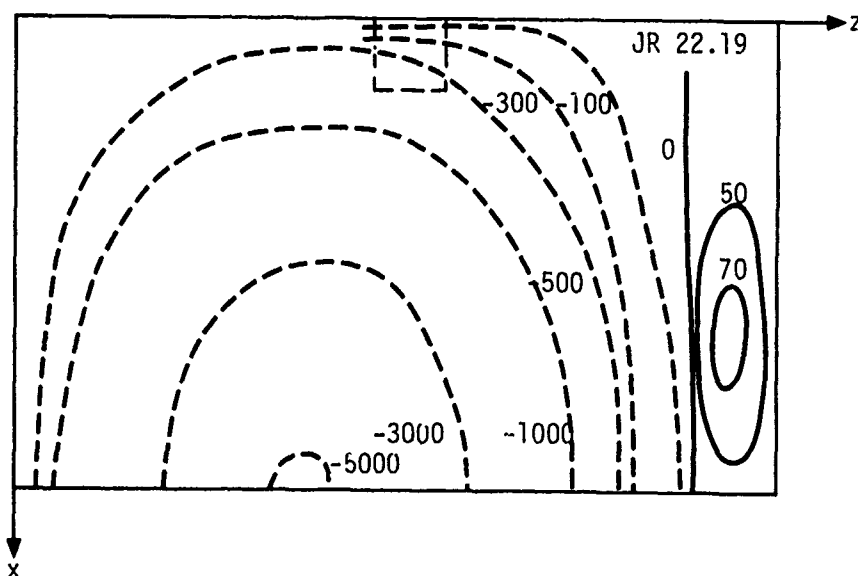


Figure 18b. Approximate contours of constant  $E_x$  at  $T = 2.9E-8$  sec.  
(Ambient boundary condition,  $\theta = 20^\circ$ ,  $Y = Y_{MAX}$ , no pole).

## 4.2 GLANC/DAVID COMPARISON

In order to make sure that DAVID was behaving in a reasonable manner, we made a comparison between DAVID, without an object, and the one-dimensional close-in coupling code, GLANC<sup>2</sup>. There are several ways in which we could have performed this experiment. We chose to make the GLANC calculation as close as possible to the DAVID calculation, i.e., the same vertical step size, etc. In this way we can see if DAVID gives as reasonable an answer as GLANC does under the same circumstances; however, because the grid sizes are larger than would normally be considered practical in a pure environment calculation, we will not be comparing the DAVID prediction to the "real" environment.

The question of spatial resolution is one which must be addressed at some point. Just exactly how much resolution is required to do the calculation properly? The DAVID geometry used in this comparison is the same as in the previous (EX) study. Therefore, each cell is 20 cm high (DY)\*, 20 cm long (DZ), and 10 cm wide (DX). Now, there is a significant amount of field variation occurring within 20 cm of the ground in a close-in environment calculation. The same would be true near the surface of an object. It is important to know whether we are simply losing space and time resolution or whether the large cell sizes are causing us to calculate a totally incorrect answer. Our studies indicate that we are simply losing resolution. There have not been enough tests to fully confirm that fact however. Assuming that our problem is basically one of resolution, what is the impact?

DAVID is intended to calculate voltages and currents on objects within the deposition region. The object is going to be resolved to the same degree as the fields that we are coupling to it. The fact that we may not be resolving the short wavelength components of the fields is, at least, consistent

---

\* 10 cm in the ground.

with the fact that we could not calculate the response of the object to those wavelengths anyway. Therefore, there seems to be little reason to worry about them.

A few words about 1-D calculations are also appropriate. Consider a plane wave of gamma rays sweeping across the surface of the earth in the y-z direction with an angle of incidence  $\theta$  (see Figure 6). In the absence of an object, there is no variation of flux or fields in the x-direction. Also, if the attenuation of the gamma rays can be ignored in the z-direction, over a distance which is important to the solution of the problem (limited by air conductivity), the physics observed at any point in the z-direction will be the same as at any other point, except that the time history will be delayed by the amount of time that it takes light to reach the observer from the burst. Therefore, derivatives with respect to z are related to the time derivative through the speed of light and the cosine of the angle of incidence. In the absence of a ground plane, the same would be true of a derivative with respect to y, except that it is proportional to  $\sin\theta$ . The introduction of a ground plane introduces additional contributions to the y-derivative.

Under these circumstances, one can calculate the fields using only the y-derivatives, i.e., the problem can be solved by differencing along a vertical line. This is a realistic thing to do when calculating fields in the close-in region at times when the conductivity is high enough to limit the distance over which an observer can see to those which are small compared to a gamma mean free path ( $\sim 100$  m). The GLANC code is based on this principle.

We will now briefly derive a set of 1-D equations for the purpose of (1) illuminating the principles involved and (2) deriving a set of equations which will help to interpret and check the numerical calculations made with GLANC and DAVID. The equations we will derive are not in the same form as used by GLANC, but that will be of no consequence.

We start with the field equations in our units ( $\vec{h} = z_0 \vec{H}$ ,  $\vec{j} = z_0 \vec{J}$ ,  $z_0 = 120\pi$  ohms, see Section 2.2)

$$\nabla \times \vec{h} = \frac{1}{c} \left( \frac{\partial \vec{E}}{\partial t} + \frac{\sigma}{\epsilon} \vec{E} \right) + \vec{j} \quad (60a)$$

$$\nabla \times \vec{E} = - \frac{1}{c} \frac{\partial \vec{h}}{\partial t} . \quad (60b)$$

Only the TM mode will be excited by the currents which are in the y-z direction. Therefore, only the  $h_x$ ,  $E_y$ , and  $E_z$  fields need be considered. Remembering that derivatives with respect to x are zero, we have three scalar equations

$$\frac{\partial h_x}{\partial z} = \frac{1}{c} \left( \frac{\partial E_y}{\partial t} + \frac{\sigma}{\epsilon} E_y \right) + j_y , \quad (61a)$$

$$- \frac{\partial h_x}{\partial y} = \frac{1}{c} \left( \frac{\partial E_z}{\partial t} + \frac{\sigma}{\epsilon} E_z \right) + j_z , \quad (61b)$$

$$\frac{\partial E_z}{\partial y} - \frac{\partial E_y}{\partial z} = - \frac{1}{c} \frac{\partial h_x}{\partial t} . \quad (61c)$$

The z-derivative is simply

$$\frac{\partial}{\partial z} \leftarrow - \frac{\cos\theta}{c} \frac{\partial}{\partial t} . \quad (62a)$$

The y-derivative has an extra term, since variations in the y-direction are caused by both the time phasing and a discontinuity of the medium, i.e.,

$$\frac{\partial}{\partial y} \leftarrow \frac{\partial}{\partial y'} - \frac{\sin\theta}{c} \frac{\partial}{\partial t} . \quad (62b)$$

The primed variable ( $y'$ ) reminds us that we have removed the time phasing effect.

Equations 61 become, after rearrangement,

$$\frac{\partial E_y}{\partial t} + \frac{\sigma}{\epsilon} E_y = - \left( c j_y + \cos\theta \frac{\partial h_x}{\partial t} \right) , \quad (63a)$$

$$\frac{\partial E_z}{\partial t} + \frac{\sigma}{\epsilon} E_z = -c j_z + \sin\theta \frac{\partial h_x}{\partial t} - c \frac{\partial h_x}{\partial y'}, \quad (63b)$$

$$h_x - (\sin\theta E_z - \cos\theta E_y) = -c \int_{-\infty}^t \frac{\partial E_z}{\partial y'} dt' . \quad (63c)$$

These are equivalent to those used in GLANC. Under conditions of high conductivity when displacement current is much less than the conduction current ( $\partial E/\partial t \ll \frac{\sigma}{\epsilon_0} E$ ), the first two can be written

$$E_y = - \left[ \frac{J_y}{\sigma} + \left( \frac{\epsilon}{\sigma} \right) \cos\theta \frac{\partial h_x}{\partial t} \right], \quad (63d)$$

$$E_z = - \frac{J_z}{\sigma} + \left( \frac{\epsilon}{\sigma} \right) \sin\theta \frac{\partial h_x}{\partial t} - \frac{1}{Z_0 \sigma} \frac{\partial h_x}{\partial y'}. \quad (63e)$$

Note that we have returned to the true current density  $\vec{J}$  rather than the normalized current density  $\vec{j} = Z_0 \vec{J}$ .

Equation 63d will be useful in checking the numerical calculations\*. It states that the vertical E-field is generated by both the vertical current and the time derivative of the magnetic field. There is no explicit spatial derivative. The horizontal field equation does contain a  $y'$ -derivative and is therefore more difficult to use in checking numerical results.

It will also be useful to understand the relation between the electric and magnetic fields at early times, when the conduction current is negligible compared to the displacement current. Under these circumstances, Equations 63a,b reduce to

---

\* A peak  $\dot{\gamma}$  of  $10^{13}$  rad/sec is used, as in the  $E_x$  study. Therefore, much of the calculation will be for times when this approximation is valid.

$$E_y = -\frac{1}{\epsilon_0} \int_{-\infty}^t J_y dt' - \cos\theta h_x, \quad (63f)$$

$$E_z = -\frac{1}{\epsilon_0} \int_{-\infty}^t J_z dt' + \sin\theta h_x - c \int_{-\infty}^t \frac{\partial h_x}{\partial y'} dt'. \quad (63g)$$

The GLANC/DAVID comparisons are shown in Figures 19 through 23. It was found to be more practical to make side-by-side comparisons rather than overlays. Since  $t = 0$  is defined differently in the two codes, we have drawn a dashed line in each graph which shows the time that the  $\dot{\gamma}$  time history peaks. Note that the GLANC calculations extend 20 nsec past the  $\dot{\gamma}$  peak, while the DAVID calculations extend only 5 nsec.

The fields represent those which would be seen 10 cm above the ground.  $H_x$ ,  $E_y$ , and the sources are actually calculated at that height. GLANC interpolates  $E_z$  to get it there, while in DAVID we simply output the quantities corresponding to the first cell above the ground.  $E_z$  is therefore the value calculated at 20 cm, as is  $E_x$ .  $H_y$  is calculated at 20 cm, also, while  $H_z$  is computed at 10 cm. The latter three field components should ideally be zero. They are not, of course, and their amplitude relative to the TM mode fields is an indication of when the calculation is starting to deteriorate. We reiterate the fact that the presence of an object within the grid will greatly control the behavior of the TE mode fields. Therefore, the fact that relatively large spurious TE fields develop in this calculation, after the gamma peak does not mean that the problem will develop on the same time scale when an object is present.

GLANC and DAVID predict about the same ionization rate at the time of the  $\dot{\gamma}$  peak (Figure 19), but this is not representative of the overall agreement. There is more structure in the DAVID curve so that it is sometimes greater than the GLANC prediction and sometimes less. The peak ionization rate predicted by DAVID is 1.5 times greater than GLANC while at 10 nsec

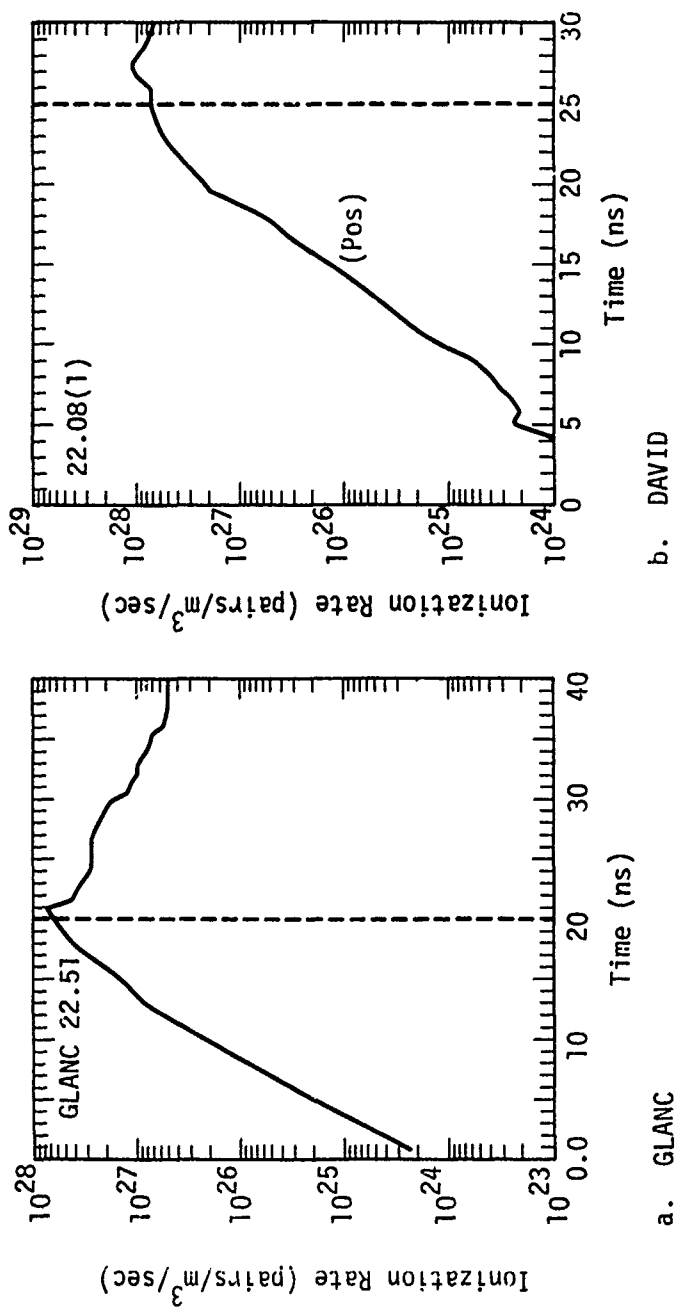


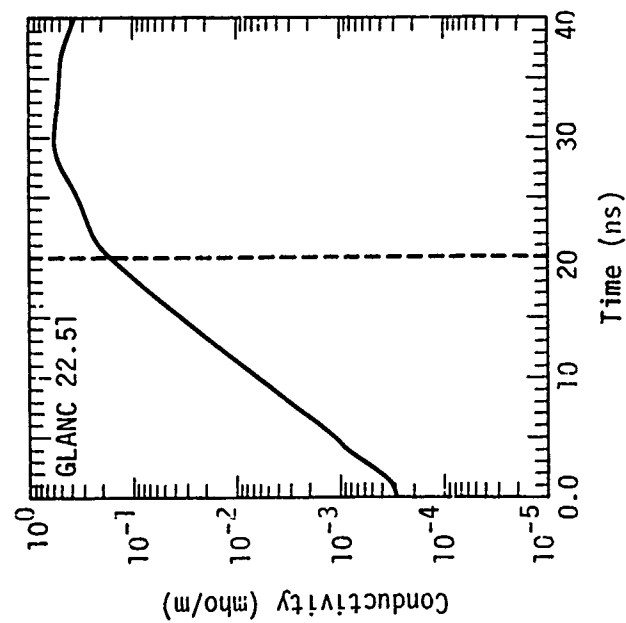
Figure 19. Comparison between the ionization rate time histories predicted by the GLANC and DAVID codes.

before the  $\dot{\gamma}$  peak, it is 1.5 times less. Both codes injected particles every time step for this comparison. Normally, we inject DAVID every other time step in order to reduce the number of particles. At very early times (about two orders of magnitude down from the peak) the sources calculated with injection every other time step can be as much as 40 percent off those calculated with injection every time step. However, as the number of particles builds up and the rise rate of the  $\dot{\gamma}$  curve decreases, the two sources agree much better. We ran this same DAVID calculation with alternate cycle injection and found 5 percent agreement at the source peak.

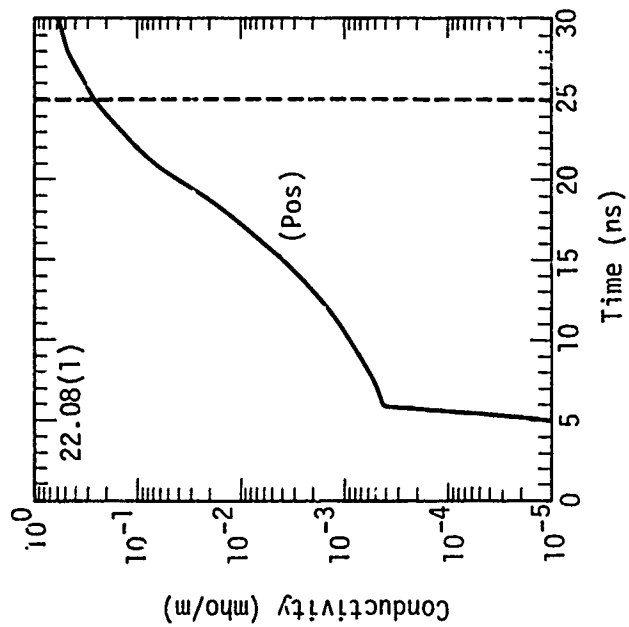
The conductivity (Figure 20) predicted by DAVID at the  $\dot{\gamma}$  peak is 1.5 times greater than that seen in GLANC. Ten nanoseconds before this it is 1.7 times lower. The DAVID calculation did not go late enough in time to compare the peak conductivities.

DAVID will give lower source strengths during the  $\dot{\gamma}$  rise for observers in the first cell above the ground because the spatial averaging scheme (Section 3.3) does not account for the fact that the cell in the ground does not contribute its share to the sources in the cell just above the ground. This can easily be fixed, but was not considered to be an important enough problem to warrant the more complicated logic that would be required in the initial version of the code.

In the Compton current comparisons (Figure 21) we start to see some interesting differences, which are fortunately explainable. The horizontal currents agree to the same degree as the ionization rate, but GLANC shows a vertical current with far more fine structure 5 to 10 nsec before the  $\dot{\gamma}$  peak. The GLANC current actually changes sign for a short time. This is not a physically real effect and would not ordinarily be predicted by the code. It is caused by the fact that we forced GLANC to inject particles parallel to the gamma path. Since they are all traveling in the same direction, the effect of magnetic turning is overemphasized. Normally, GLANC would inject a distribution of particles at angles about the ray. The center of mass of these particles would not react as strongly to the magnetic

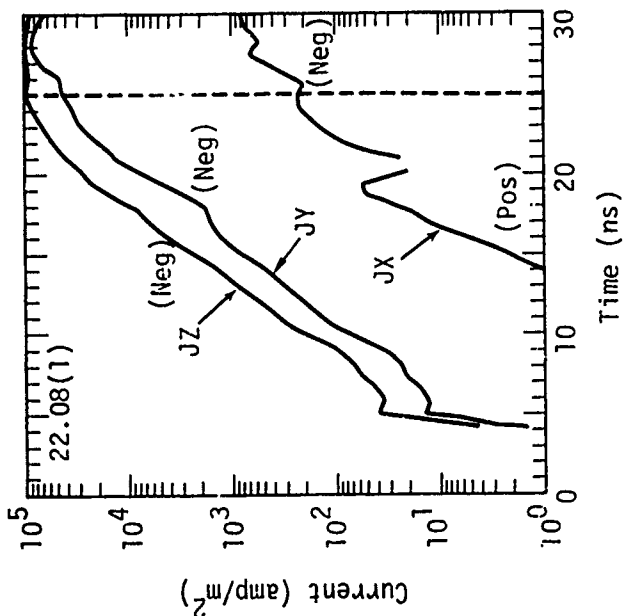


a. GLANC

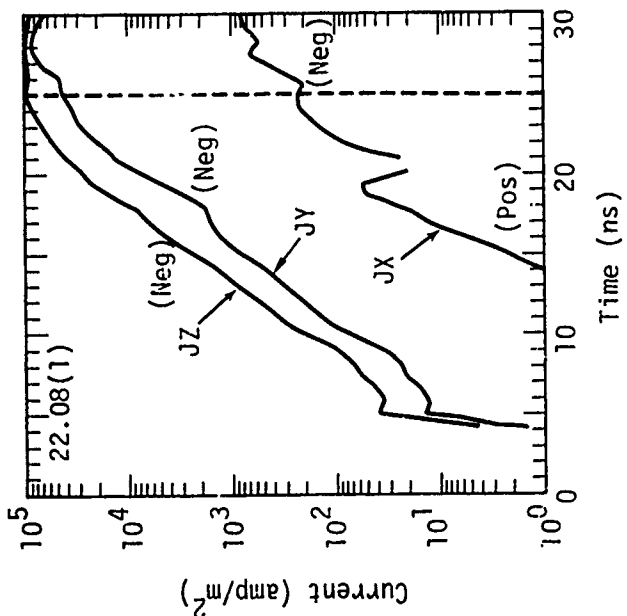


b. DAVID

Figure 20. Comparison between the conductivity time histories predicted by the GLANC and DAVID codes.



a. GLANC



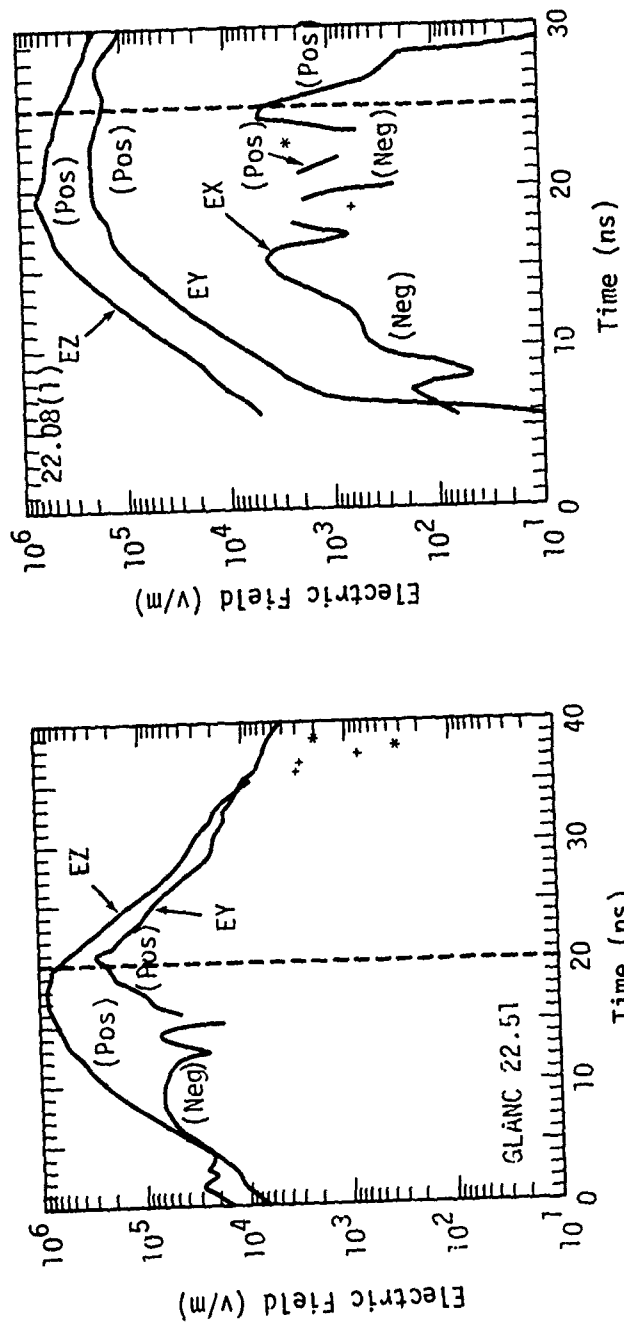
b. DAVID

Figure 21. Comparison between the Compton current time histories predicted by the GLANC and DAVID codes.

forces as the individual particles themselves. In DAVID the spatial averaging also acts as a time averaging scheme. Half of the current scored in a given cell is contributed by the particles within the cell. The other half is contributed by the particles in the six adjacent cells (the contribution from one cell is missing at the boundaries). Since the particles in the adjacent cells are at different phases, there is a time averaging effect. Note that  $J_x$  is two orders of magnitude lower than  $J_y$  and  $J_z$ , so it is not a significant perturbation.

The horizontal electric fields ( $E_z$ ) predicted by the two codes (Figure 22) agree well, within a factor of 1.5. The early time vertical fields do not. In fact, they have the opposite sign until 5 nsec before the  $\gamma$  peak. The DAVID fields maintain the same sign throughout the time history. GLANC starts out with the opposite sign and then changes it to agree with DAVID. The peak vertical fields agree to within a factor of 1.5

The early time discrepancy in the vertical fields is undoubtedly due to the way in which the propagated field is handled in each code. Neither code does very well, actually, during this low conductivity phase of the problem. DAVID tends to underestimate the propagated part of the signal because the sources and fields are built up over a relatively short distance from the front boundary. GLANC assumes that the sources are the same, as a function of local time all the way back to  $z = -\infty$ . This would tend to give a larger propagated signal than DAVID. The 1-D approximation is not as bad here as one might first expect. The fact that the sources are assumed to be the same back to  $z = -\infty$  is really not important when the burst is off the ground because the gamma wave front arrives faster than the electric field, which is generated along the air/ground interface. Therefore, conductivity is allowed to build up and absorb the propagated field. The field would not grow large in any case, because it loses phase with the Compton current. Also, the longer integration distance partially compensates for the fact that the sources are stronger near ground zero. The 1-D approximation becomes worse as



a. GLANC

b. DAVID

Figure 22. Comparison between the electric fields predicted by the GLANC and DAVID codes.

the angle of incidence approaches zero. In our problem the GLANC prediction is probably reasonable. We will return to this point after discussing the magnetic field predictions.

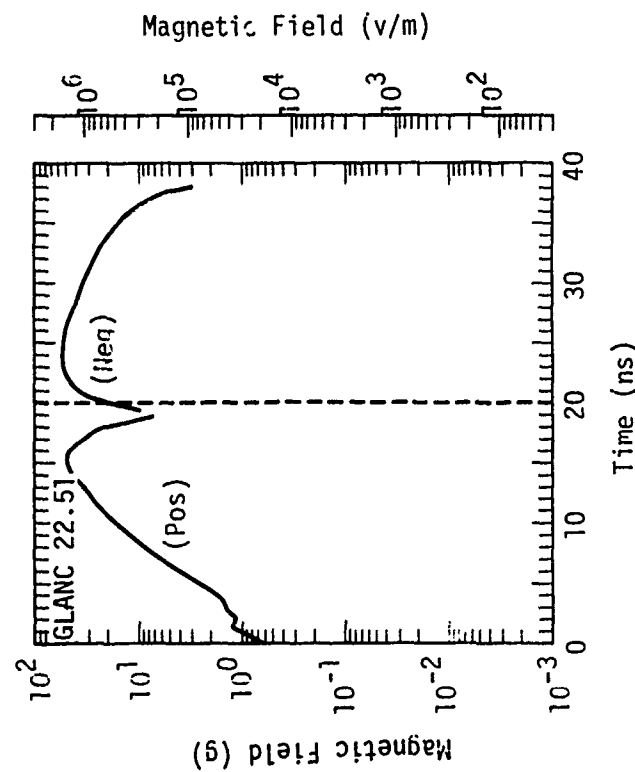
The magnetic fields are shown in Figure 23. GLANC outputs its magnetic fields in units of gauss, so an extra volts/meter scale has been added to facilitate comparison with DAVID\*. The GLANC predictions are a factor of three larger than the DAVID predictions. An inspection of the spatial plots revealed that the problem was caused by not having the grid large enough. One could see the H-field building up in the +z direction, even on the rise of the pulse when the field should be decreasing as a function of increasing z.

This brings out a very important point, which should be remembered when performing 3-D calculations. Magnetic fields are not nearly as intimidated by conductivity as electric fields. The skin depth arguments which are commonly used to claim that the conductivity is high enough to isolate an object from its surroundings do not apply so well when magnetic field coupling is involved. This is emphasized by the later time DAVID calculations which show  $H_y$  and  $H_z$  growing substantially and  $H_x$  falling rapidly because of this boundary problem. The conductivity at this time is very high ( $\sim 0.5$  mho/m).

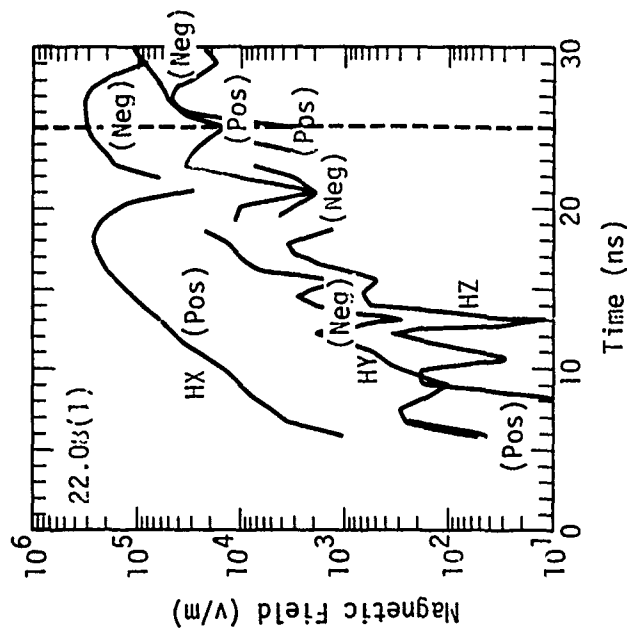
We considered this problem before doing the pole calculations in the next section. The grid was enlarged in the z- and y-directions. It isn't that critical, however, as the spatial plots will show. After the conductivity builds up and starts to control the current running on the vertical pole, the magnetic field generated by the ground is seen to be dominated by that caused by the current running on the pole. The pole coupling in this case is more electric than magnetic.

---

\*  $H(\text{volts/meter}) = 3 \times 10^4 B(\text{gauss})$ .



a. GLANC



b. DAVID

Figure 23. Comparison between the magnetic fields predicted by the GLANC and DAVID codes. Note the extra v/m scale on the GLANC curve  $H(\text{volts/meter}) = 3 \times 10^4 \text{ B(gauss)}$ .

We now return the effect of the propagated field on the early time  $E_y$  prediction. We know that this ( $E_y$ ) field is composed of two parts: the vertical component of the local radial field and the part that has propagated along the earth. In order to give the Poynting vector ( $\vec{E} \times \vec{H}$ ) the right direction (+z), the propagated  $E_y$  component must be negative and this will then oppose the locally generated component. This is shown by Equations 63f and 63g, which are zero conductivity approximations.

If there were no propagated fields, both  $E_y$  and  $E_z$  would be positive in our coordinate system. The magnetic field, which is positive during these times, would therefore decrease  $E_y$  and increase  $E_z$  (remember that if there was no discontinuity to generate  $H_x$ , there would also be no propagated signal). A little work shows that both the DAVID and GLANC calculations satisfy these equations at early times (the  $y'$ -derivative term in  $E_z$  can be ignored as a first approximation). The propagated field contribution is simply much larger in GLANC, causing a sign reversal at early times, until the conductivity is large enough to make Equation 65d valid. At times near and after the peak, the electric fields are behaving as  $J/\sigma$  in both calculations and therefore agree much better.

### 4.3 POLE STUDY

Having gained confidence in DAVID through the GLANC comparison described in the previous section, and feeling that we understood most of the code's problems and limitations, calculations were performed for the problem of a vertical pole passing through the earth and exposed to a peak  $\dot{\gamma}$  of  $10^{13}$  rad/sec. An angle of incidence of  $20^\circ$  was chosen because a few experimental data points were available to tell us whether the current induced on the pole was a reasonable prediction. The problem geometry is shown in Figure 24.

Several parameters were varied, including the width of the pole in the x-direction. The data had been taken for a pole with a circular cross

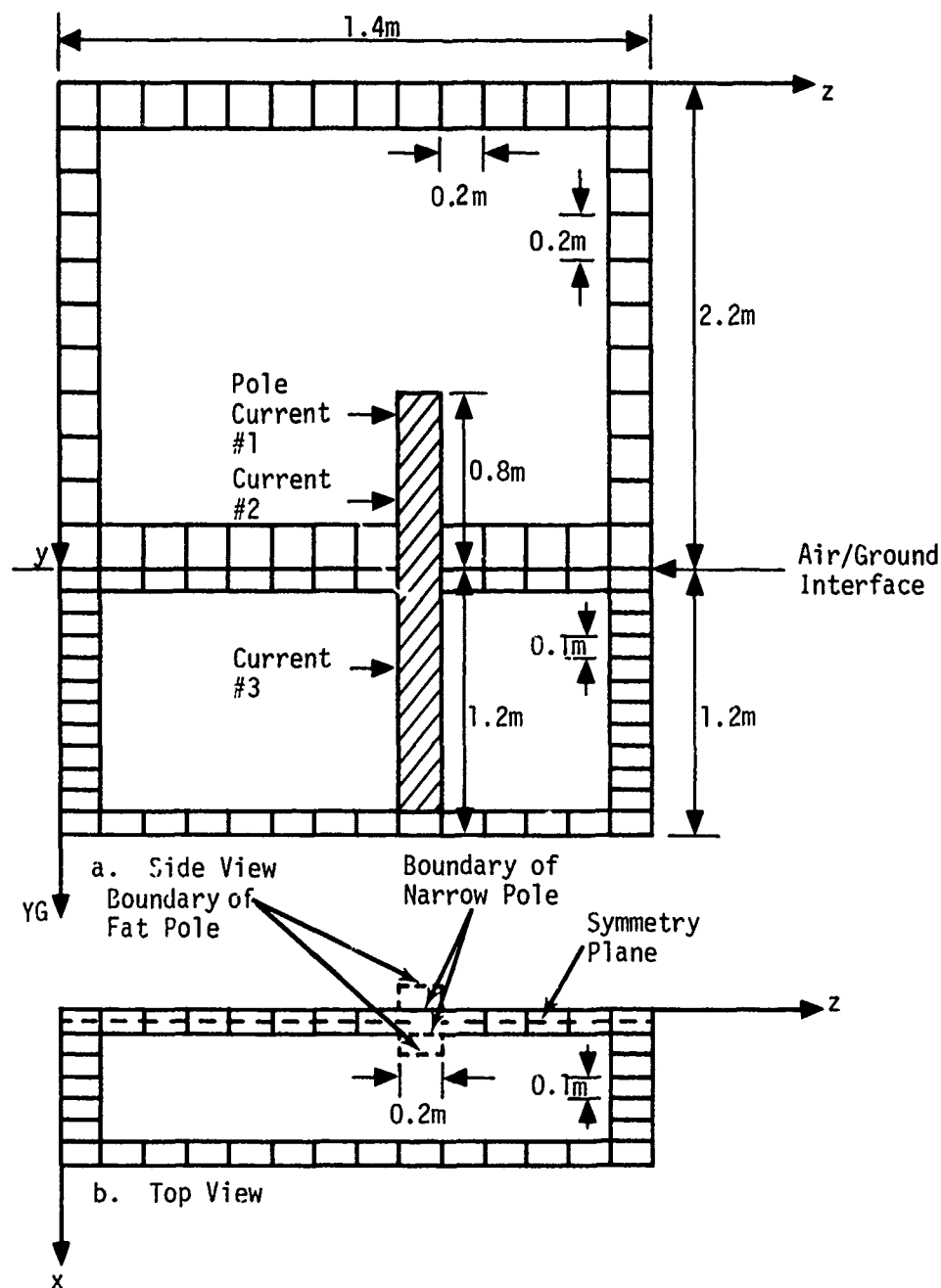


Figure 24. Geometry used in the pole current calculation. Note the use of two pole sizes. The fat pole has a width ( $\Delta x$ ) of 30 cm and a circumference of 100 cm. The narrow pole has a width of 10 cm and a circumference of 60 cm. The dimensions include the image half of the pole on the other side of the symmetry plane. Cells are shown only near the boundaries.

section and a diameter of 10 cm. With our constant spatial step sizes, we could not calculate a pole that narrow and still maintain a grid large enough to keep the outer boundary a sufficient distance away. We felt, however, that during the highly conducting portion of the signal, that we could scale the pole's surface currents by its circumference. Therefore we ran parameter variations using two pole sizes: 100 cm circumference and 60 cm circumference. The 10 cm circular pole has a circumference of 31.4 cm. After scaling the net currents by the ratio of the pole circumference to 31.4 cm, we found that the answers agreed quite well in the air. The pole current at a depth of -45 cm was found to be fairly insensitive to pole size. These studies will be shown shortly.

The scaling in the air was expected to work because the poles were fairly close in size and their cross sectional shapes were not extremely different. The near fields of the pole should vary logarithmically with effective pole radius. As we shall see, the currents running on each face of the pole can vary significantly. It would have been better to scale each component separately before summing, instead of scaling the net current. However, the latter method worked well enough for our purposes.

The reasons for the insensitivity of the pole currents below ground to pole size will be discussed later. Most of the calculations were performed using ground drivers\*, which fell off exponentially with the slant range into the ground. Ground conductivity enhancement was sometimes used. The enhanced conductivity was assumed to be proportional to the local gamma flux, with the constant of proportionality being  $10^{-14}$  mho/m/rad/sec. Thus, with a peak gamma flux of  $10^{13}$  rad/sec, the maximum enhancement at the surface would be 0.1 mho/m. The ambient ground conductivity was set at  $10^{-2}$  mho/m. The dielectric constant was 10.

---

\* When viewing the curves, it can be assumed that ground currents are present unless otherwise stated.

Three steps are required to calculate the pole current: (1) the tangential magnetic fields are extrapolated to the pole surface, (2) the surface current density at that point is computed, and (3) the current density is integrated around the pole. Since DAVID is a general purpose code, intended to handle many geometries, it was felt that it would be most efficient to use a separate current calculation algorithm for each type of object rather than build in a general one, which would require a great deal of computer logic. Since the code requires the user to supply his own algorithm, we will go into more detail on how we did it for the pole than would normally be considered prudent. There are several peculiarities of the code that may not be obvious at first.

A two step extrapolation is required because the tangential magnetic fields are computed on the cell walls and not at the cell center (see Figure 8). In Figure 25, we show a cross section of the "fat" pole and the surrounding cells which are needed for the extrapolation. The pole is located

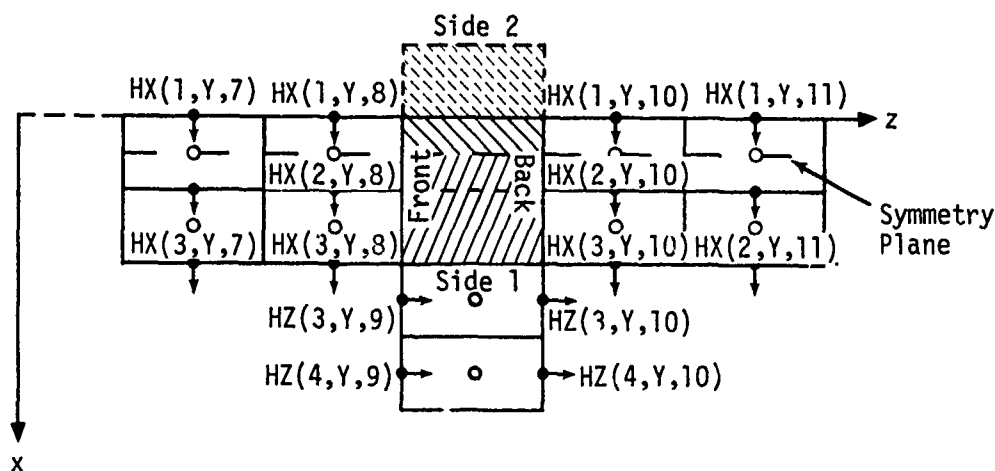


Figure 25. Geometry used to compute current running on the "fat" pole (3 cells wide in x-direction, including image).

at  $K = 9$ , i.e., the pole is centered at  $z = 1.7$  m from the front boundary. In the x-direction, the pole extends over  $I = 1, 2$ . However, the symmetry plane runs through the center of the  $I = 1$  cells, so half the width of that cell is associated with the image half of the pole. The locations of the fields that we need for the pole current calculation are shown by arrows. The first step is to interpolate in order to estimate the values of the field at the cell center (designated by the open circles in the figure). At the symmetry plane, we have  $H_X(1, J, K) = H_X(2, J, K)$ , so no interpolation is required as long as we only use linear interpolations. Then, an extrapolation is required to estimate the tangential field at the pole surface. For these calculations, we used a linear extrapolation\*.

Having obtained values of  $H_X$  and  $H_Z$  at the centers of the cell faces which define the pole, the components must be summed in the proper sense to calculate the net current. At some point, the magnetic fields calculated by the code must be divided by  $Z_0 \approx 120\pi$  to obtain units of amp/m. Then, the net current is given by

$$I = \oint \mathbf{H} \cdot d\mathbf{\ell}$$

We define positive current as the flow of positive charge in the +y-direction (electron flow upward). Therefore, the net current is

$$I = \sum_{\text{BACK}} \Delta X \cdot H_X - \sum_{\text{SIDE1}} \Delta Z \cdot H_Z - \sum_{\text{FRONT}} \Delta X \cdot H_X + \sum_{\text{SIDE2}} \Delta Z \cdot H_Z \quad (65)$$

where these are the sums of the renormalized H-fields on each side. By symmetry,

$$H_Z|_{\text{SIDE2}} = - H_Z|_{\text{SIDE1}} .$$

---

\* Extrapolating the product of H and the cylindrical radius from the pole works better in this case, because of the pole shape. We chose to extrapolate the H-field along because of the more general applicability of the procedure and because it seemed to work well enough.

The reader should be able to fill in the details.

Figure 26 shows the currents calculated on the "fat" pole by DAVEJR (prescribed current and ionization rate). We also show the conductivity time history near the pole for the 30 cm observer. No enhanced conductivity is used in this calculation. The numbers in parentheses near the waveform peaks show the value of the current (in kiloamps) normalized by the circumference of the 10 cm diameter circular pole. We will state the measured peak values after completing the theoretical parameter study. The pole used in this and the following calculations is transparent to gamma rays.

The first notable feature of Figure 26 is the way in which the currents at +30 cm and +70 cm follow the conductivity. Also, they are very close in magnitude even though one observer is near the ground and the other is near the end of the pole. Actually, the +30 cm observer is not that close to the ground in as much as it is isolated by the air conductivity. However, this isolation is not as great as one might guess at first. What is happening is that the boundary condition provided by the pole is so strong that it controls the fields in the poles vicinity, even near the ground. One would probably get similar answers for the current running on the pole in the air without including the ground plane at all\*. Later studies will show that this is not true for grazing incidence angles because of the importance of the propagated field generated at the surface. Note the slight negative excursion at early times. This will be seen to be a scattered field response. It is not very important in this case, being a factor of 430 below the peak, but it is of theoretical interest. We will watch its behavior later as we vary the flux and angle of incidence. This

---

\* It would not be surprising to find that with this incidence angle (or greater) one can obtain reasonable answers using an infinite cylinder in air.

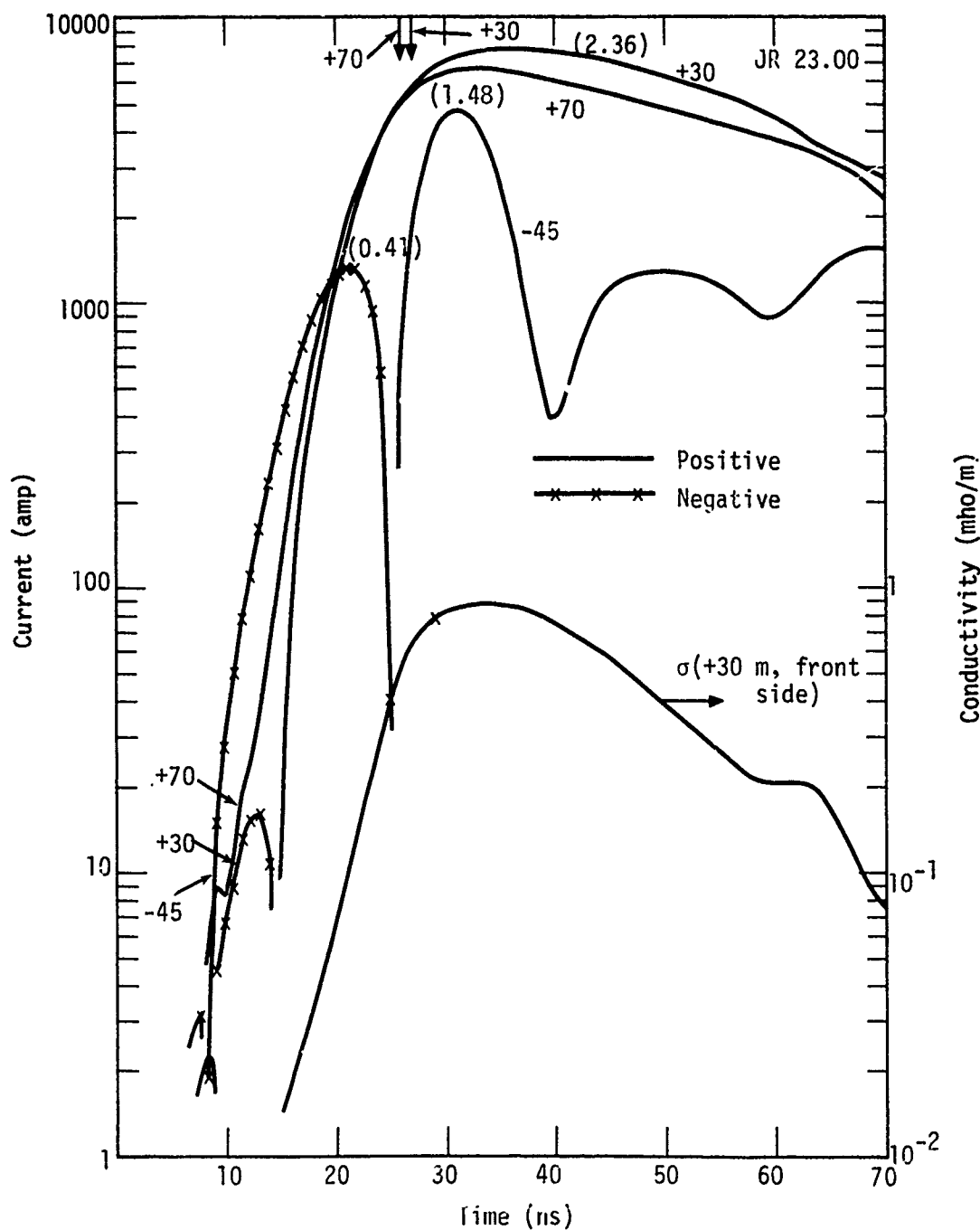


Figure 26. Currents generated on fat pole without ground conductivity enhancement. Numbers in parentheses are peak scaled currents (kamps). Air conductivity is also shown. Analytic sources.

part of the response is more significant for observers below the ground.

The current at +70 cm leads that at +30 cm at early times by the difference in time required by the gamma wave front to reach the two observers ( $\sim 1$  nsec with this  $20^\circ$  incidence angle). The vertical arrows at the top of the figure show the times at which the  $\gamma$  pulse peaks at the two observers. The current at +70 cm is limited to a value less than that at +30 cm, probably because there is some charge build-up at the top, despite the high conductivity.

The current seen at -45 cm has a much different character than that seen at positions in the air. It will also prove to be much more sensitive to various physical factors, e.g., ground drivers and conductivity enhancement. The current starts out with a negative swing, which is the scattered field response (the electric field in the ground is negative during almost the entire time frame plotted). It then swings positive, rises to a peak and oscillates. The oscillation is riding on a rising base. It is possible that this late time rising is a numerical problem caused by the outer boundary in the ground. However, it is not unreasonable to expect the current to try and make a more uniform distribution over the pole at late times, matching the current on the pole in the air, and that is what it appears to be doing. We will look at how different physical effects influence the current at -45 cm later.

Figure 27 shows the same calculations for the "narrow" pole (60 cm circumference instead of 100 cm). Qualitatively, they are the same. When the air observer currents are scaled, the peak currents are seen to be nearly the same as the scaled fat pole currents. That, of course, is the point we are trying to prove. The same is not true at the ground observer. As a matter of fact, the positive current becomes larger rather than smaller. The negative swing is smaller, as one might expect from a scattered field response. The negative peak is probably controlled more by the rise of the positive component than by the inductance of the pole, however. The

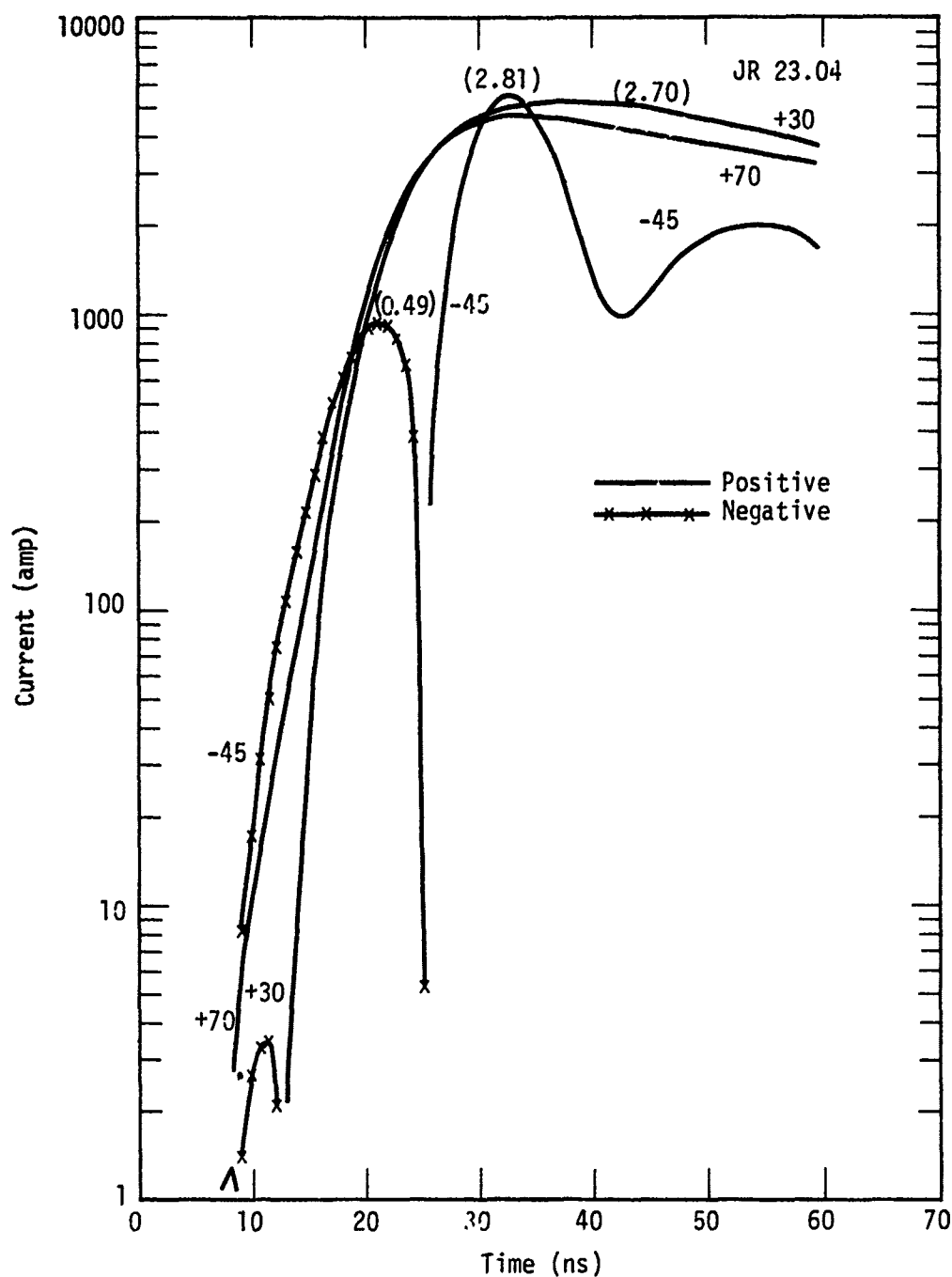


Figure 27. Currents generated on narrow pole without ground conductivity enhancement. Analytic sources.

positive current corresponds to electrons running up the pole. This current is driven by the voltages which are trying to pull electrons back out of the ground. The pole offers itself as a convenient path and, in addition, "amplifies" the voltage. A narrower pole causes a greater radial field concentration in the air and a larger current to the surface. The current leaves the pole just above the surface because of the high air conductivity and the currents on the pole higher up do not see any difference.

The effect of introducing ground conductivity enhancement is shown in Figure 28. The currents running on the pole in the air are not changed and are therefore not plotted. Only the currents seen at -45 cm on the narrow pole are shown. The scattered field response is not altered because the enhanced conductivity has not risen high enough yet. It is not clear that it would be anyway, since the layer of significant enhancement lies above a depth of 20 cm and the fields that excite the pole at this time can propagate down from that layer faster than the conductivity could change them. The main effect of the enhancement is to dampen the positive part of the current time history. The positive peak is lowered and the oscillations die away faster.

Until now, we have only looked at prescribed current calculations (DAVEJR). Figure 29 shows that the particle calculations (DAVID) are not significantly different. Here we compare the current predicted at +30 cm and -45 cm. The biggest difference is in the air, where the currents build up faster with the prescribed currents. The prescribed current formulation assumes that the electron current is in equilibrium with gamma flux. In sea level air, the lifetime of the Compton electron is on the order of  $10^{-8}$  second. This is at least comparable to the time over which the gamma pulse changes significantly. In this case, it can be considered much greater than that time. Therefore, an equilibrium condition does not exist and electrons born during an early part of the gamma pulse exist at the same time as those born at a later time. During the rise of the gamma pulse,

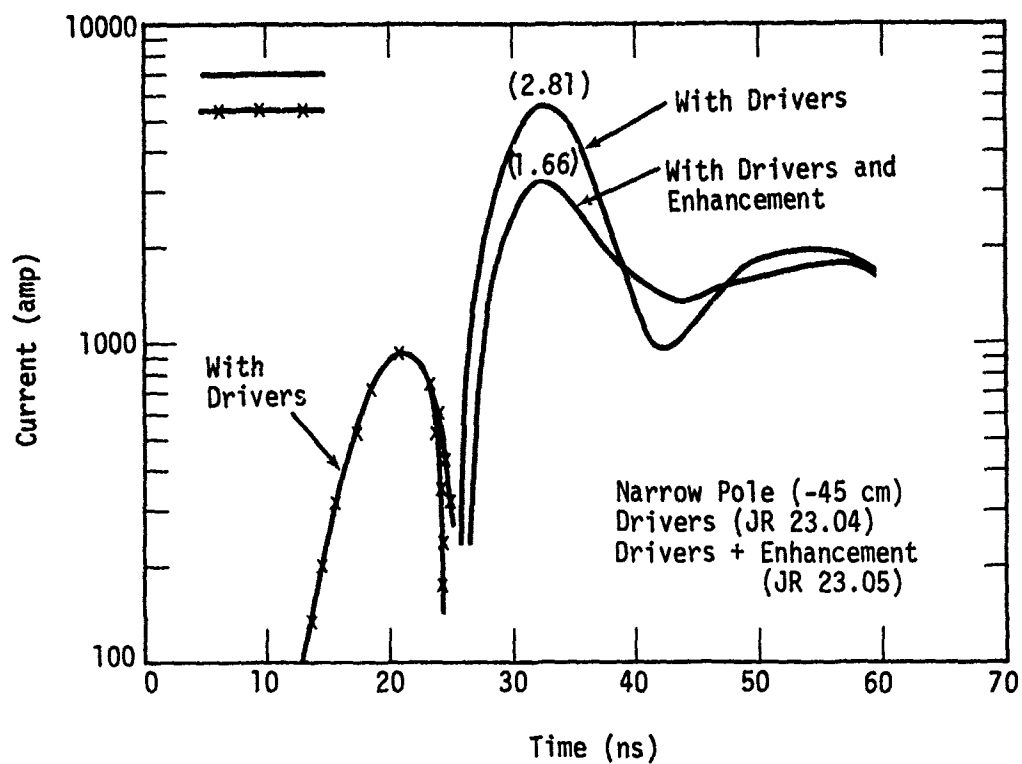


Figure 28. Current induced on narrow pole (-45 cm) with and without ground conductivity enhancement. Ground drivers are used in each case.

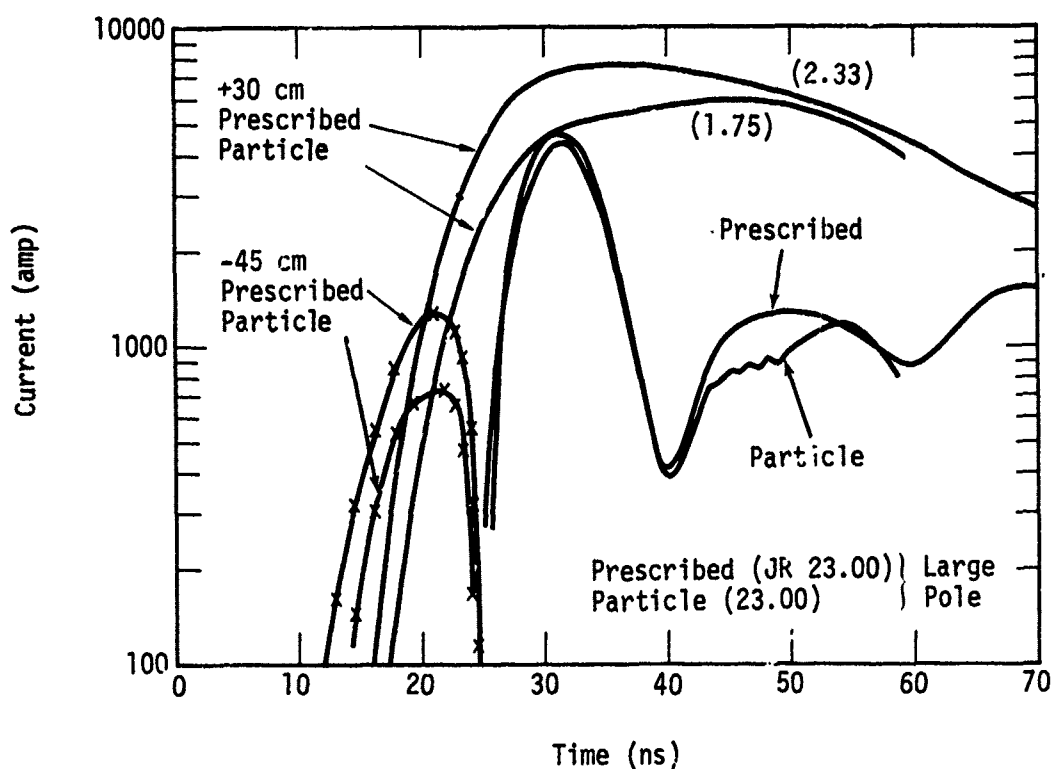


Figure 29. Comparison between pole currents predicted with non-self-consistent prescribed sources and self-consistent particle sources. Ground drivers are considered, but not ground conductivity enhancement.

when it is behaving exponentially, this deviation from equilibrium manifests itself as a simple delay in the current. After the peak, when the flux varies more slowly, the two predictions agree better. If we had put a proper delay into the prescribed sources, the comparison would have been better.

The effect of the delay is also seen in the early time current induced on the pole at -45 cm. The current at this time is driven by the vertical electric field, which is created by the gradient of the magnetic field, which has diffused downward from the surface. No such delay is seen in the positive part of the current. This portion is highly influenced by the ground drivers which are prescribed in both the particle code and the prescribed current code. Prescribed ground currents without a delay are valid in the ground because of its high density and the correspondingly smaller electron lifetime (shorter by a factor of  $10^3$ ). Conductivity enhancement was not used in these calculations.

The effect of ground drivers is shown in the comparison of Figure 30. The calculations shown here are for a fat pole with enhancement (particle sources). Unfortunately, there was an error in the enhancement such that it was a factor of 1.5 times greater in the calculation without drivers than in the one with drivers. Our previous results show that this fact will not substantially alter the comparison however. The currents seen at +30 cm, which were not altered by the presence of enhancement at all, show a slight decrease when drivers are removed. The current calculated at +70 cm showed no change at all, and the comparison is not shown. In the ground, we see that the large positive peak was due entirely to the ground drivers. Without them, we have a dominant negative peak followed by a gradual flow of electrons back up to the surface.

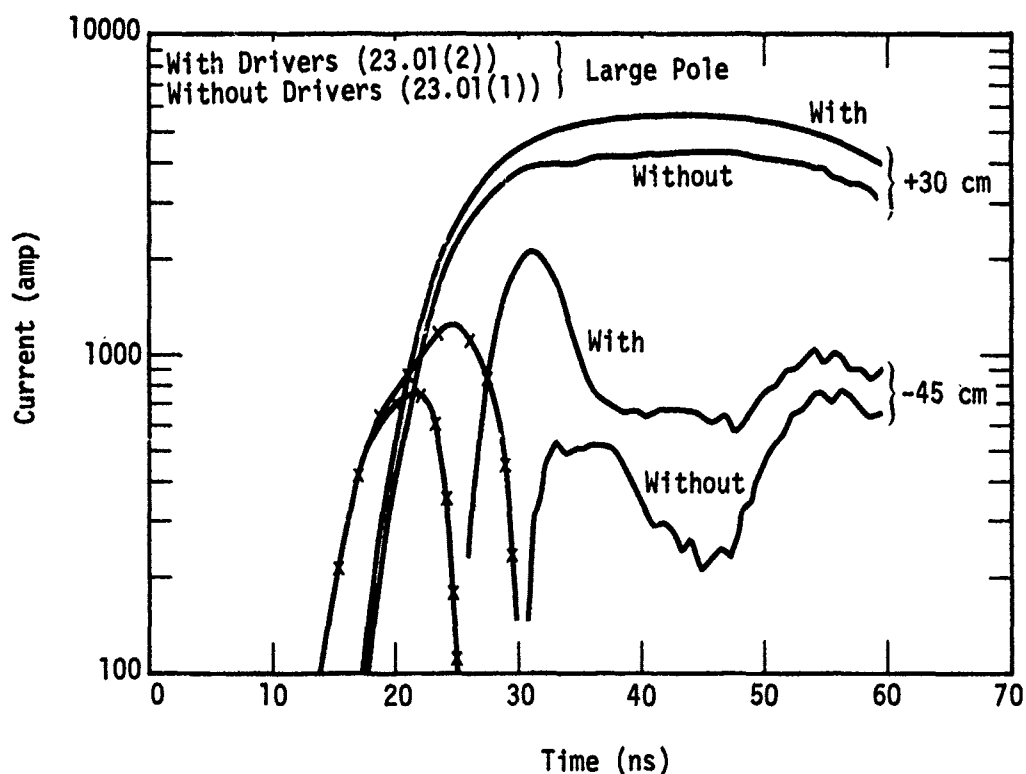


Figure 30. Comparison between pole currents predicted with and without ground currents. Enhancement in problem without currents is 1.5 times greater than in problem with ground currents, explaining difference in late time pole currents below surface. There was no difference in pole current observed at +70 cm. This calculation used particle sources in the air.

The part of the current identified with the ground drivers is very insensitive to the pole size, in the two cases considered here. This is true whether or not ground conductivity enhancement is considered. A comparison of Figures 26 and 27 shows that this is true without enhancement and the comparison of Figure 31 shows that this is true with enhancement. This insensitivity is consistent with the idea that current is being drawn from an area of ground with a radius on the order of a skin depth. The differences in current would be due to the relative areas occupied by the pole and the radial electric fields developed around the pole. The current seen at -45 cm is not due to any Compton charge generated at the same depth, but is the reaction to fields generated by the radial ground conduction currents.

As mentioned above, a pole transparent to gamma rays was used in these calculations. Similar calculations were made for an opaque pole, but no significant differences were seen. This may be due in part to the pole size. However, there is good reason to believe that the actual pole response is insensitive to pole opacity at these incidence angles and gamma fluxes. However, the fields in space around the pole are sensitive as was seen in the  $E_x$  study (Section 4.2).

The pole response due to the direct interaction of the gamma rays with the pole obviously become reduced as the incidence angle increases and the horizontal component of the flux decreases. There is an additional reason for direct interaction effects to be reduced as the incidence angle increases in the presence of a large gamma pulse with its correspondingly high air conductivity. A gamma wave front striking the pole produces either a new increase or decrease of charge on it depending on several factors which include the opacity of the pole. The charge can be neutralized by currents running on the pole and by conduction currents in the  $\epsilon$ . If the neutralization is produced by currents running along the length of the pole, the signature

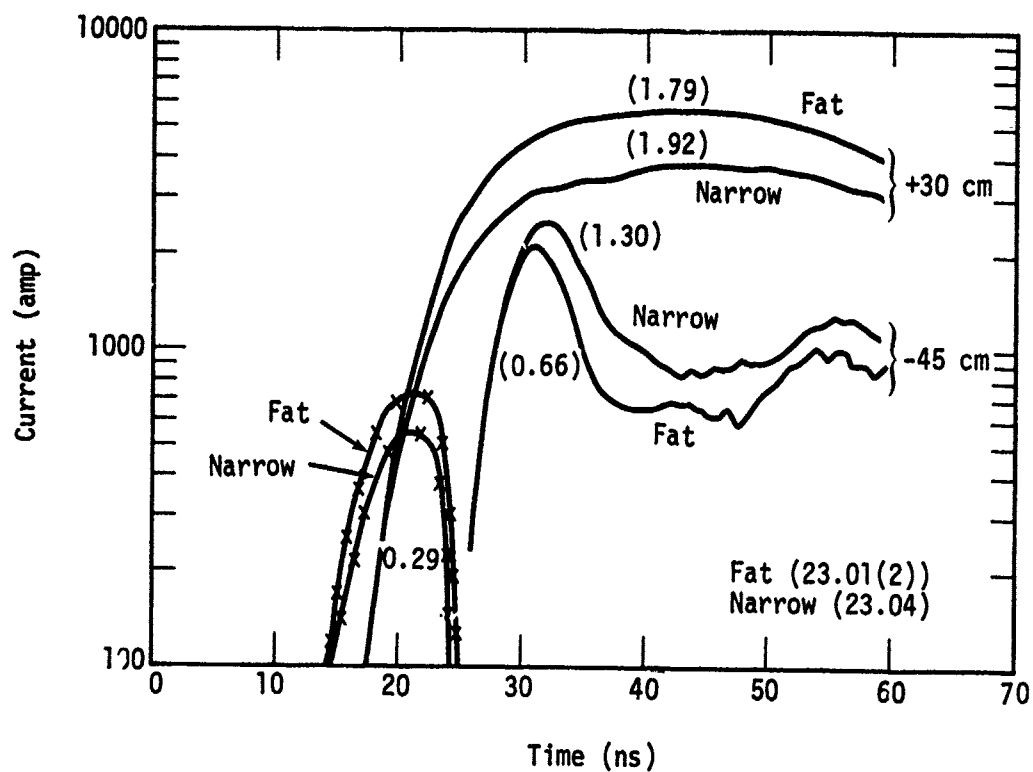


Figure 31. Comparison of currents calculated on the fat and narrow poles by DAVID (particle sources). Both calculations include ground conductivity enhancement.

of the net current will indicate the pole opacity. If air conduction currents dominate, they can reduce any longitudinal pole currents due to the direct interaction mechanism. The fluxes used in this study produce a high conductivity very early in the pulse. The direct interaction signal is wiped out before it has a chance to be seen (actually, there was a factor of two increase in the tiny scattered field response of the fat pole at +30 cm). When the angle of incidence is small, the direct interaction occurs simultaneously along the pole. There is no resulting longitudinal current at a given point until such time as a pulse could travel from some discontinuity such as the end of the pole or the air/ground interface. If the conductivity builds up in this time frame, the propagated longitudinal current pulse will never reach the observer. This shallow incidence angle effect was probably another factor in the loss of an opacity signature in these calculations. For a given peak flux, there should be a incidence angle which maximizes direct interaction effects, as seen in the longitudinal current.

Figure 32 is our estimate of the net longitudinal currents that would be seen at +30 cm and -45 cm on a 10 cm diameter pole. It is obtained from the particle calculation for the narrow pole, considering both ground drivers and ground conductivity enhancement. The following types of scaling were performed: (1) the +30 cm current was scaled by the ratio of the pole circumferences (0.523), (2) the negative scattered field response at -45 cm was scaled by the same factor, and (3) the positive (ground driver) response at -45 cm was not scaled at all.

Experimental results indicate a peak response in the air (+20 cm) of 2000 amps and in the ground (-50 cm) of 1900 amps, with the peak of the ground signal occurring about 10 ns earlier than the air peak. Our predictions (at somewhat different positions) indicate peaks of 1800 amp and 2500 amp respectively with the difference in peak times being about 15 ns. Given the physical and numerical uncertainties involved, this agreement must be considered fortuitous, especially in the ground. The currents in the air, at this incidence angle, are relatively insensitive and should have been easier to estimate.

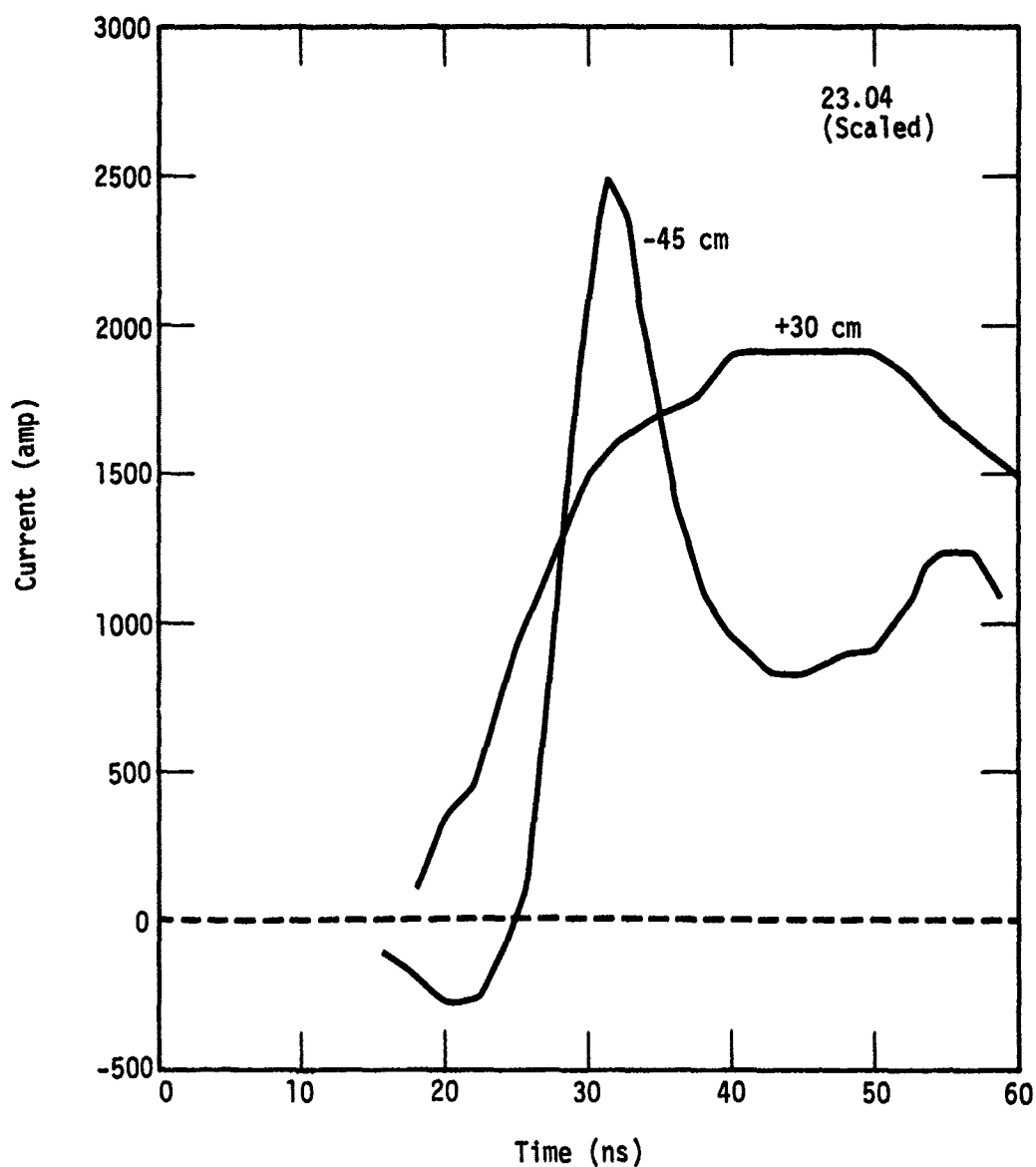


Figure 32. Currents predicted for a 10 cm diameter gamma transparent pole at +30 cm and -45 cm. Calculations include effects of ground drivers and ground conductivity enhancement with a  $10^{13}$  rad/sec peak flux. Self-consistent particle sources are used in the air.

Figures 33 through 35 show the unscaled currents running on each side of the narrow pole. These can be quite different and it is good to remember this when we speak of the net longitudinal current. There is also a strong current running around the side of the pole in the z-direction. We did not calculate it explicitly, but its existence can be seen from the fact that  $H_y$  is the same magnitude as  $H_z$  at a position  $\Delta x/2$  away from side 1. To obtain the net longitudinal current, add the components labeled "front," "back," and "side" with the indicated sign and multiply by two. The values plotted are for the half of the pole on one side of the symmetry plane. When comparing the current components, remember that the width of pole over which the side current density is integrated is four times greater than the width of pole that the front and back currents were integrated.

Figures 36a - 36d compare the spatial variations of  $E_y$  and  $H_x$  in the z-direction with and without the small pole. The comparisons are at 10.2 and 20.2 nsec. The variation is along a line 30 cm above the ground and in the symmetry plane. Particle sources are used. The pole calculation is the same computer run that generated the currents shown in Figures 32-35.

Our final parameter study is intended to show the importance of the scattered field response for small incidence angles and low fluxes. We do not claim that the predictions of the 3-D code are correct here, since it does not calculate the propagated signal well, but it should certainly show the proper trends. The analytic source code (DAVEJR) was used for these studies.

Figure 37 shows the narrow pole currents calculated with a peak dose of  $10^{13}$  rad/sec and an incidence angle of  $20^\circ$ . Ground drivers and conductivity enhancement are included. In Figure 38, we show the early time

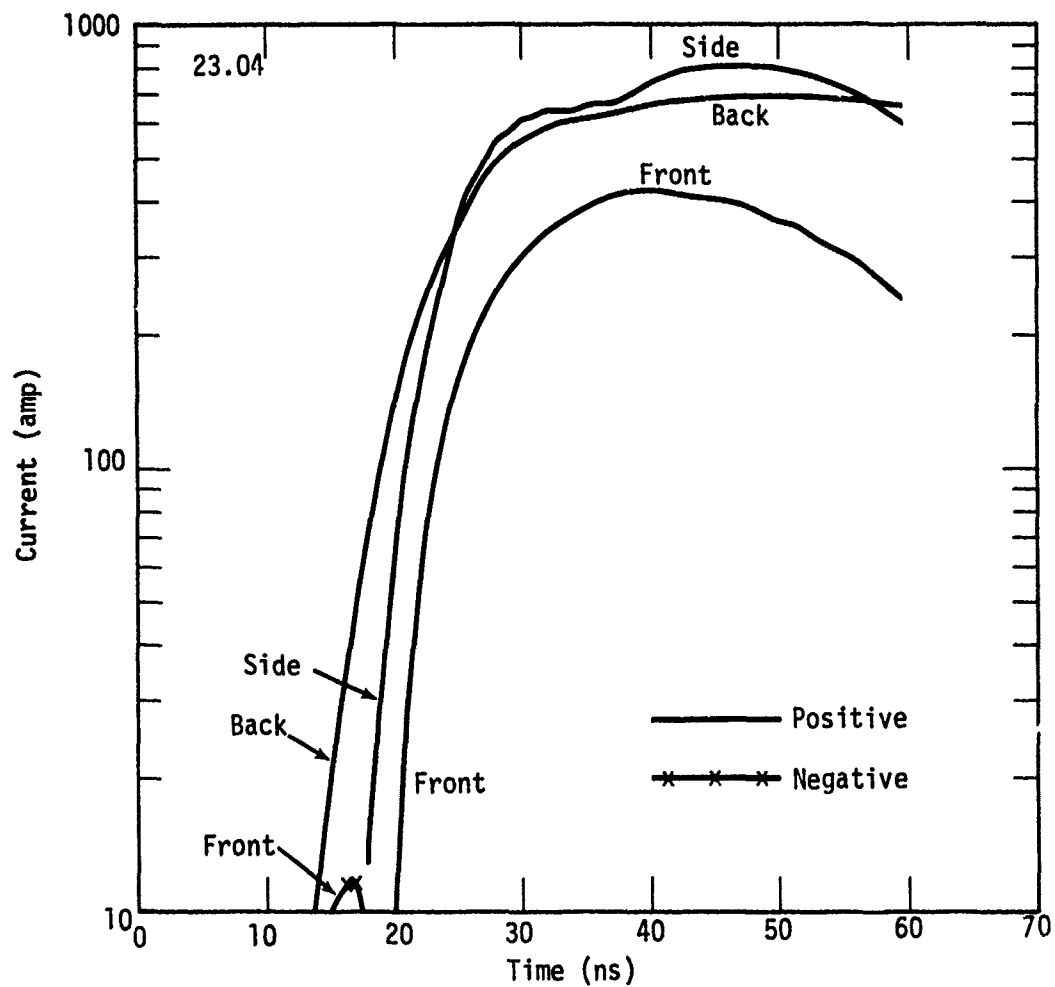


Figure 33. Components of current running along sides of the "narrow" pole at +30 cm.

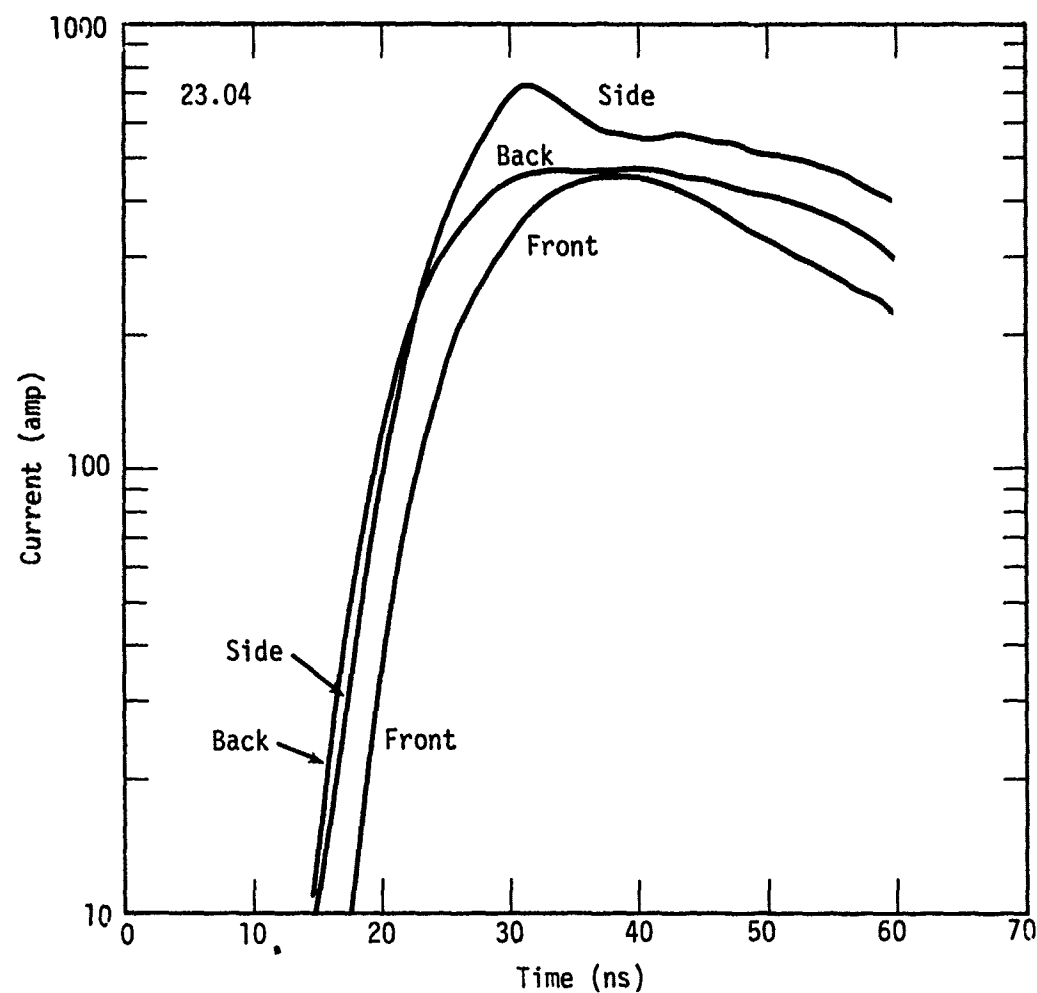


Figure 34. Components of current running along sides of the "narrow" pole at +70 cm.

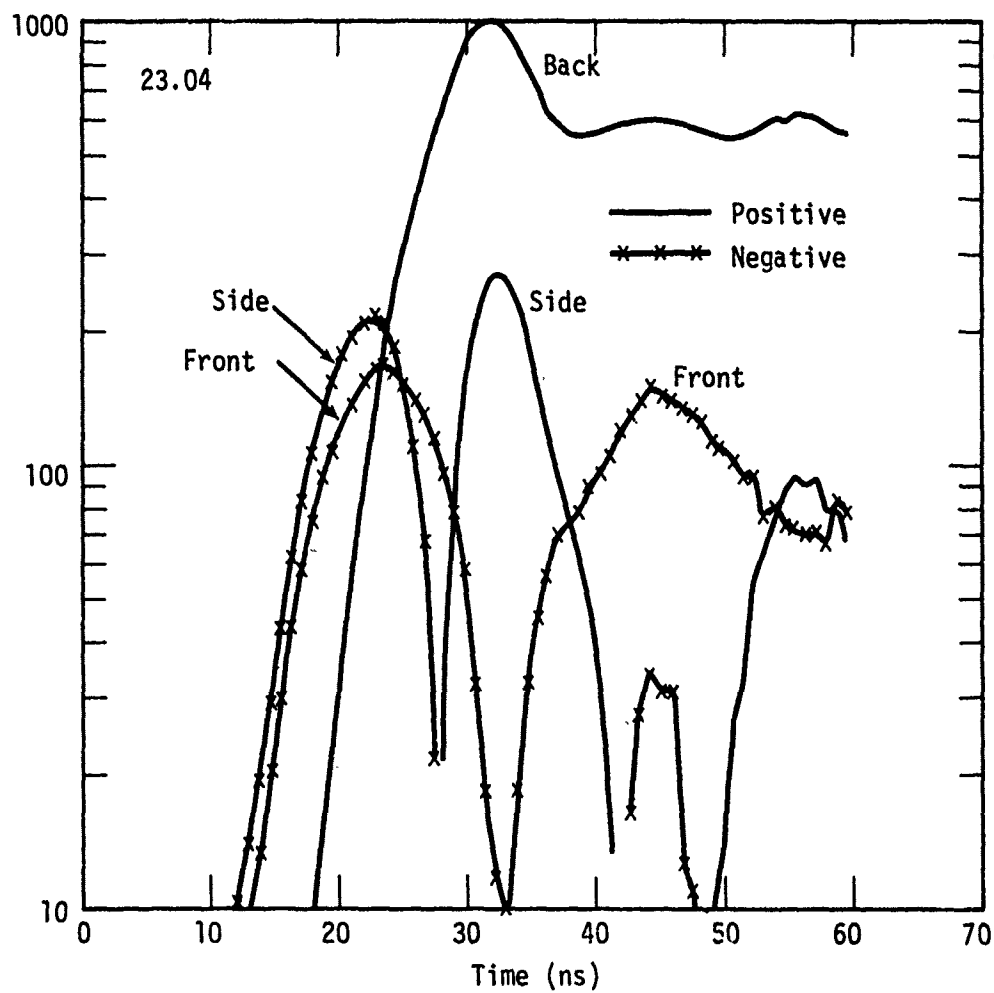


Figure 35. Components of current running along sides of the "narrow pole at -45 cm.

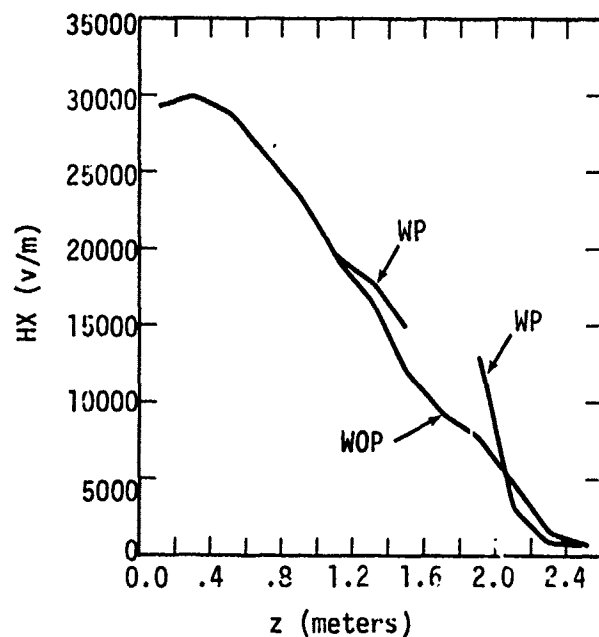


Figure 36a. Variation of magnetic field in z-direction with pole (WP) and without pole (WOP) along a line at +30 cm height on symmetry plane. Particle sources,  $T = 10.2$  ns. 1 gauss - 30,000 v/m.

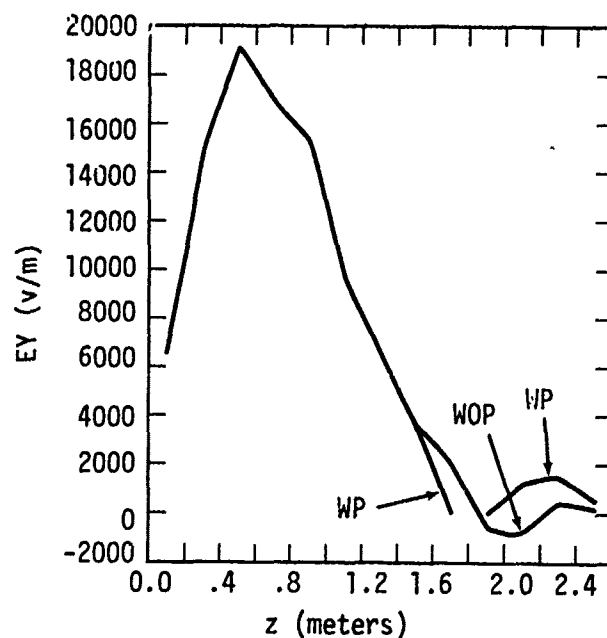


Figure 36b. Variation of vertical electric field in z-direction with pole (WP) and without pole (WOP) along a line at +30 cm height on symmetry plane. Particle sources,  $T = 10.2$  ns.

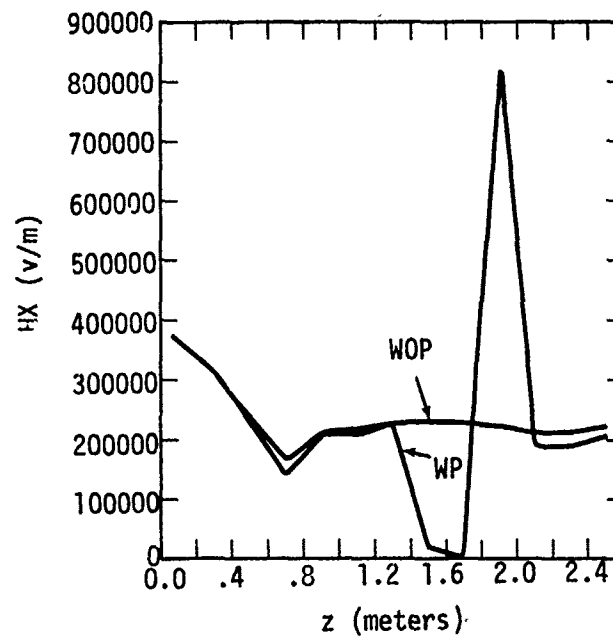


Figure 36c. Variation of magnetic field in z-direction with pole (WP) and without pole (WOP) along a line at +30 cm height on symmetry plane. Particle sources,  $T = 20.2$  ns.

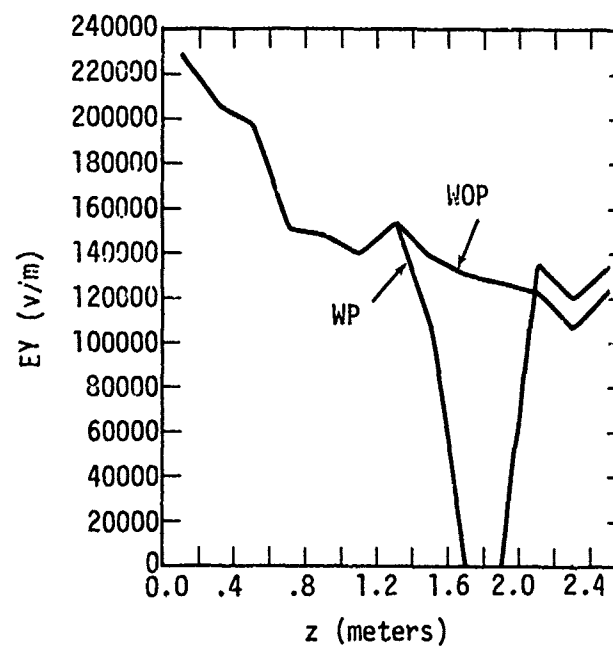


Figure 36d. Variation of vertical electric field in z-direction with pole (WP) and without pole (WOP) along a line at +30 cm height on symmetry plane. Particle sources,  $T = 20.2$  ns.

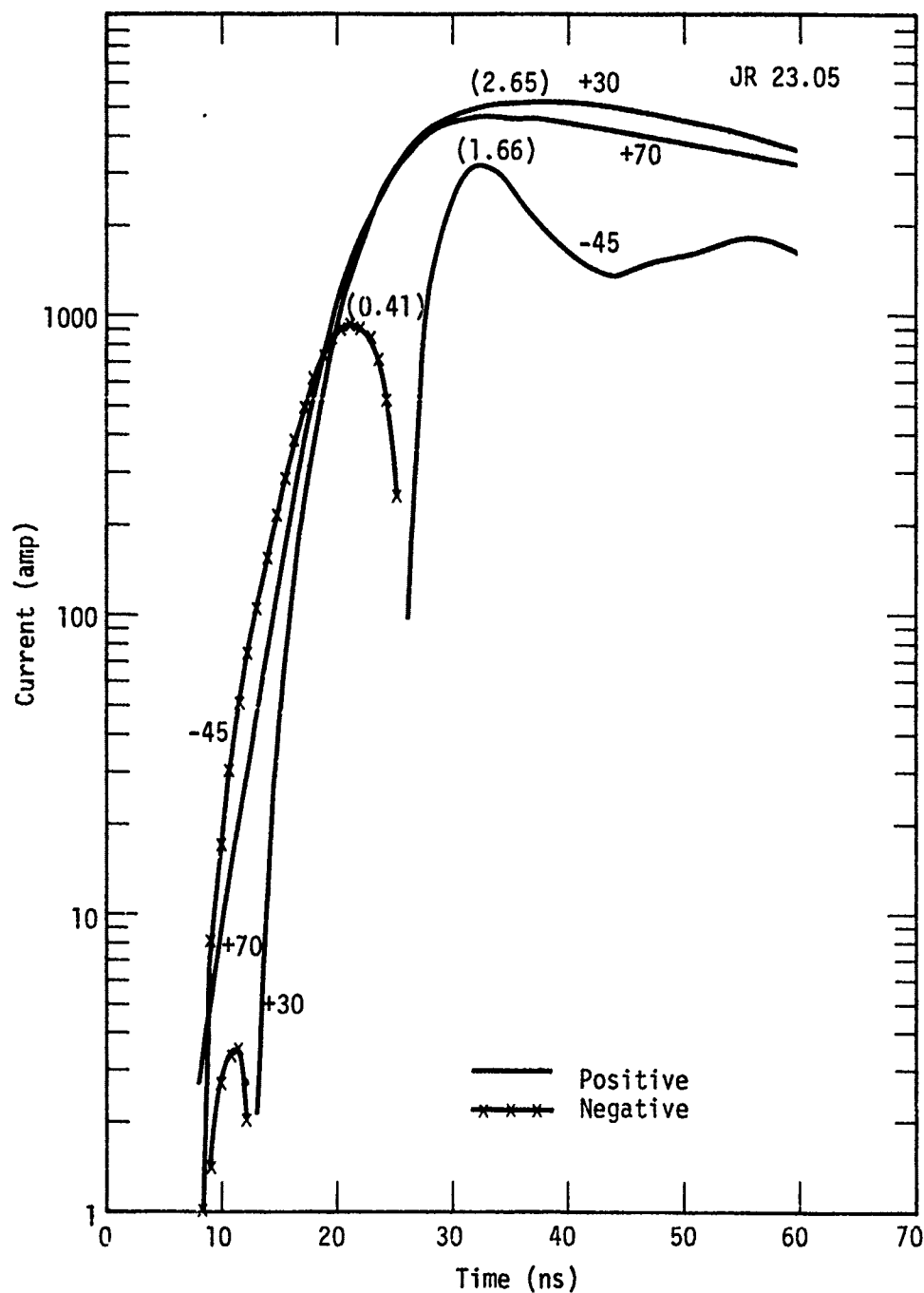


Figure 37. Narrow pole currents generated with a peak flux of  $10^{13}$  rad/sec at  $20^\circ$ .

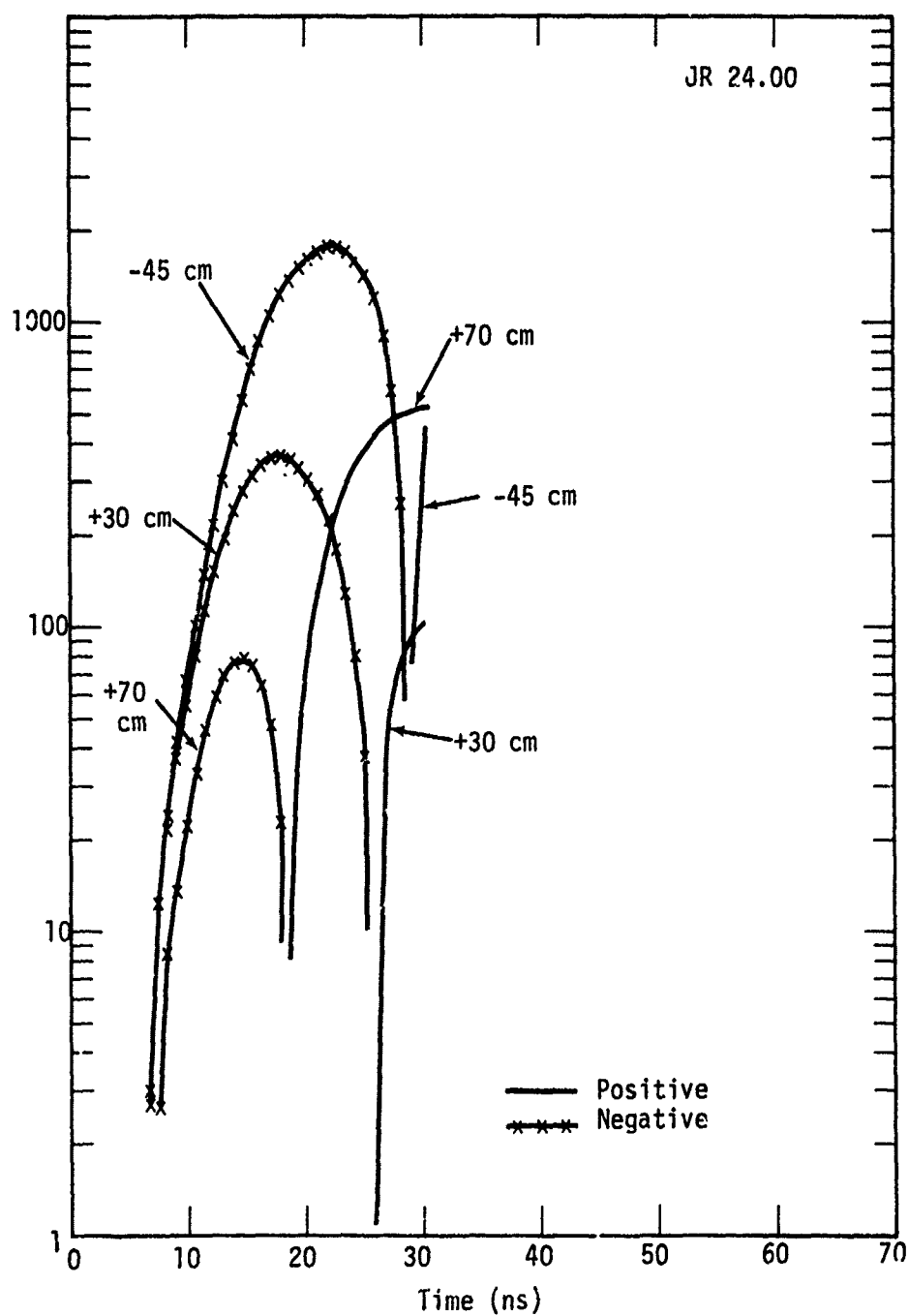


Figure 38. Narrow pole currents generated with a peak flux of  $10^{13}$  rad/sec at  $3^\circ$ .

portion of the pulse when the incidence angle is reduced to  $3^\circ$ . Note the prominence of the negative scattered field response, even at these dose rates. In Figures 39 and 40 we maintain the same angle ( $3^\circ$ ) but reduce the flux to  $10^{12}$  rad/sec and  $4 \cdot 10^{11}$  rad/sec respectively. Even though the calculations were only taken out to 30 nsec, one can see that the scattered field response has become totally dominant (except at +70 cm).

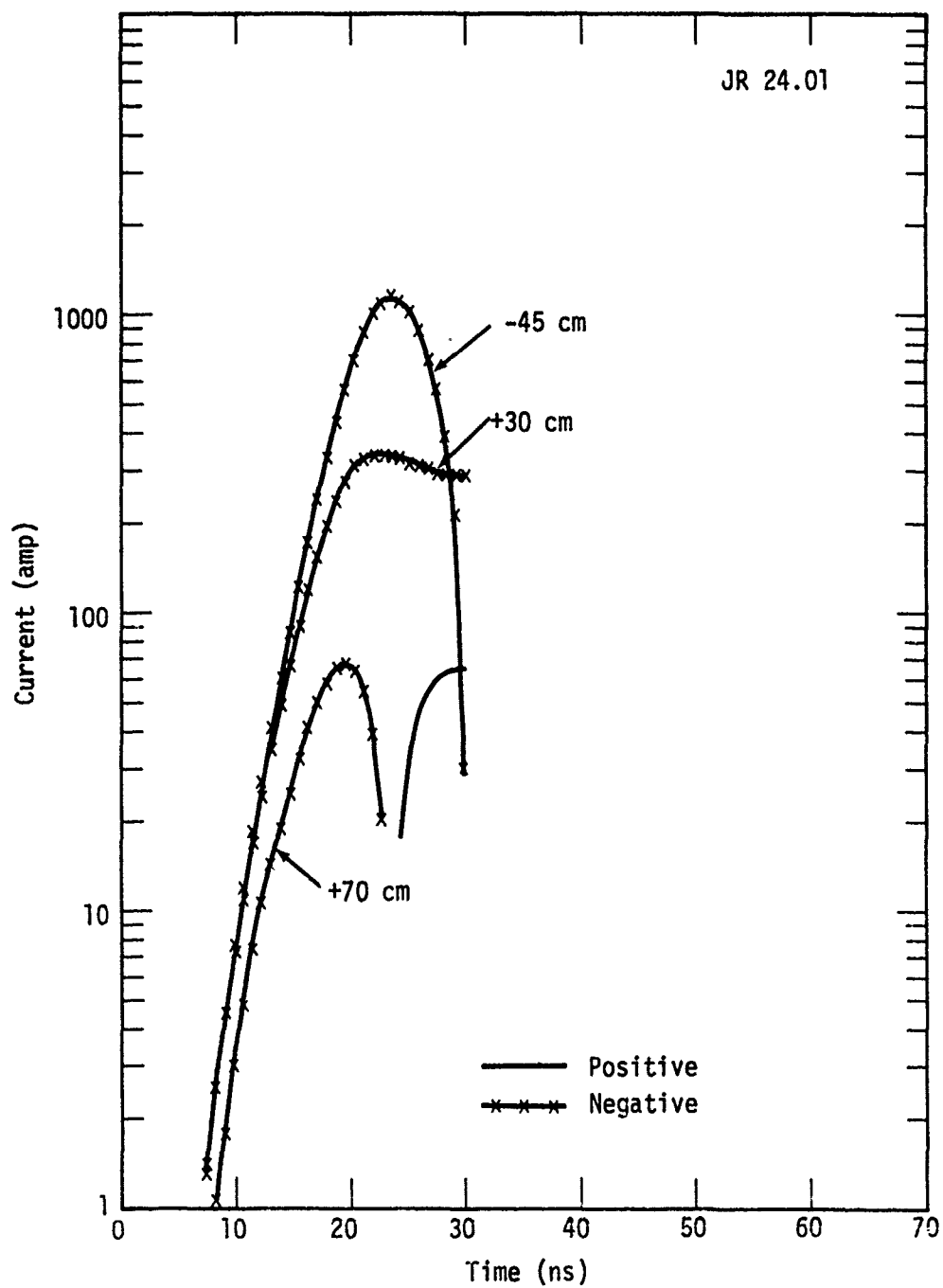


Figure 39. Narrow pole currents generated with a peak flux of  $10^{12}$  rad/sec at  $3^\circ$ .

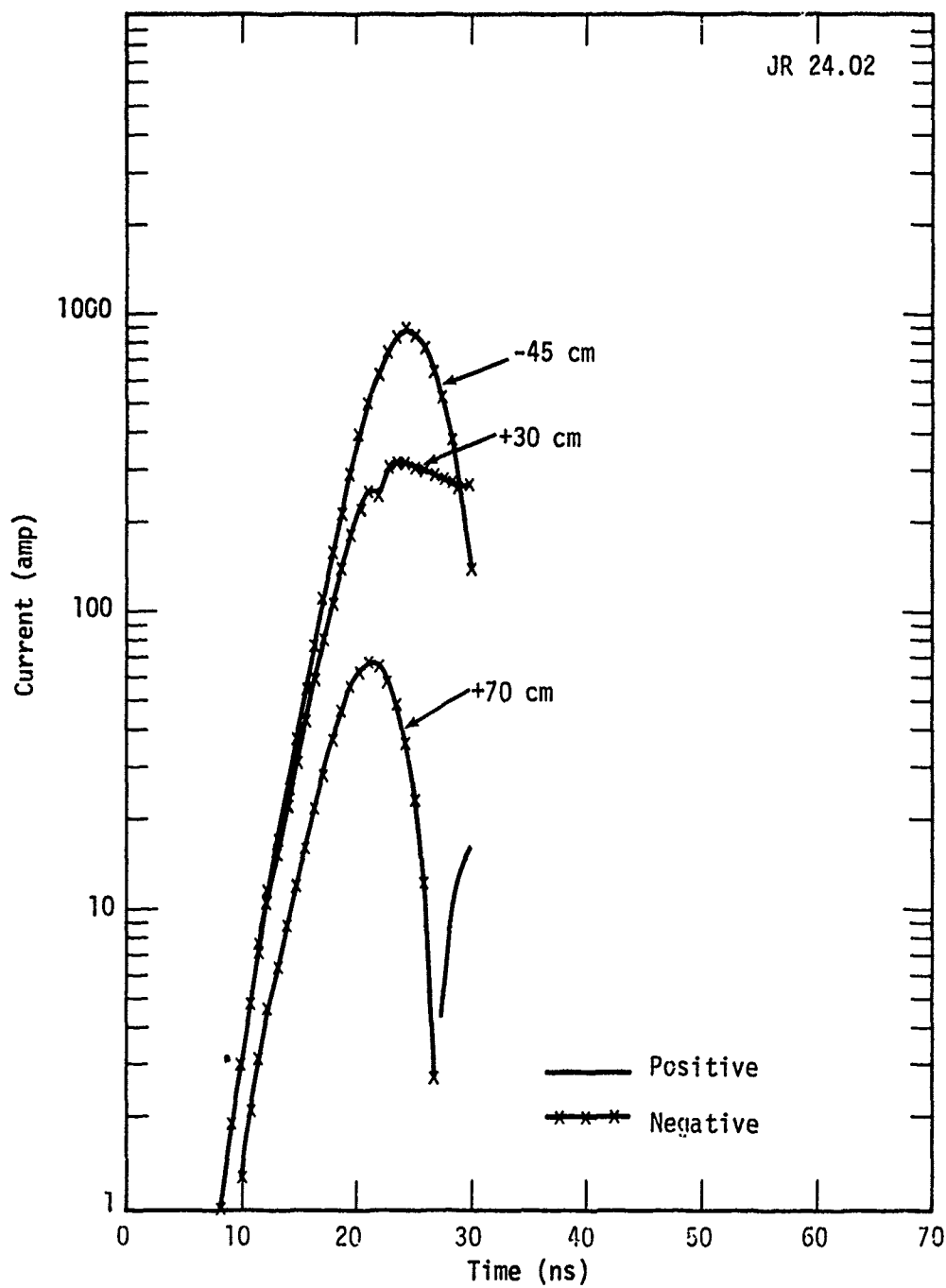


Figure 40. Narrow pole currents generated with a peak flux of  $4 \times 10^{11}$  rad/sec at  $3^\circ$ .

## SECTION 5

### CONCLUSIONS AND RECOMMENDATIONS

We have described a three-dimensional close-in coupling code constructed for the purpose of estimating the voltages and currents induced on arbitrarily shaped objects. The code comes in two versions: a particle following self-consistent version (DAVID), and a simpler one which uses prescribed currents in the air (DAVEJR). The two versions are identical except for the source routines. Since DAVEJR does not store particle information or solve the equations of motion, it is much faster and can be optimized to handle a much larger grid. It should be an extremely useful tool in the study of the tactical problem.

The philosophy used in writing DAVID and DAVEJR emphasized simplicity and usability. The codes could have been made more sophisticated, both in terms of the physics and the numerics. Instead, an attempt was made to produce a reliable code with well defined and tested limits of applicability; one which could easily be upgraded or modified by future users. This goal seems to have been accomplished. The codes give the right answers, within the limits built into them. The coding is relatively easy to follow and other users should have no great difficulty in adapting DAVID to their needs.

DAVID was tested against the GLANC 1-D close-in environment code. The results are reported in Section 4.2. GLANC was configured to match the DAVID calculation in terms of grid and time step size. In general, the agreement was quite good. The disagreements were explained. One result

of this comparison was to increase the working volume before we attempted the pole current calculations shown in Section 4.3. The results of the pole current parameter study were explained theoretically and gave insight into how one might construct models or use simpler techniques to calculate such problems in the future.

Recommendations for future work fall into two categories: (1) types of problems to be attacked and (2) code improvements. The types of improvements will depend, in part, on what problems are solved.

In many ways, 3-D close-in coupling codes are very powerful. They are also very limited. They include a great deal of physics, but lack spatial resolution, are limited to fairly high conducting regions, and are expensive to use. The 3-D code is but one weapon in the arsenal we have at our disposal to attack the close-in coupling problem. The other weapons include analytic calculations, lumped and distributed parameter models, and 2-D codes. DAVID can best be utilized in (1) calculating currents and voltages on arbitrarily shaped objects, within the constraints of the code, (2) isolating the important parts of the physics so that other (simpler) techniques can be developed, and (3) aiding in the development of methods for building lumped and distributed parameter models of complicated systems and their interaction with the environment. All too often, codes of this nature are considered ends in themselves. They become crutches and an excuse to stop thinking. The state-of-the-art is not nearly advanced enough to build black box type codes.

In the immediate future, DAVID (and DAVEJR) should be used to continue the theoretical study of the pole problem begun in Section 4-3. This should lead into the low flux "tactical" problem. It would be very useful to introduce variously shaped objects and to look at the effect one nearby object has on another. One could look at two poles in different relative positions and even connect them to form loops with a magnetic field response.

The pole calculation pointed out an important factor that must be considered when going to tactical problems. That factor is the importance of the scattered field response of the pole to the propagated vertical electric field and the vertical component of the local radial (from the burst) electric field. This response is very important below the ground even with high fluxes, and in the air when the angle of gamma incidence is small and/or the flux is small. The three-dimensional codes do not calculate this part of the response well because a long distance is required to build up the proper propagated field\*. One could put in a more complicated boundary condition using a 2-D environment code calculation, but a wiser move would probably be to do the response problem in two steps. The early time, low conductivity, part of the response can be done using other methods, while the later, high conductivity part of the calculation can be done using a full 3-D calculation.

The low conductivity scattered field response could be obtained in one of several ways. Analytic calculations might be appropriate. On the other hand, if the pole is thin compared to interesting wavelengths, a 2-D code might be used in which minus the incident vertical electric field is used as the pole boundary condition and the pole is allowed to radiate into a time dependent conductivity, which is obtained from an environment code calculation. Codes of this nature already exist and are easily constructed in any case. For more complicated structures, a 3-D code can be easily and cheaply constructed using the same principle\*\*. Such a 3-D code could

---

\* Cylindrical geometry codes do even more poorly because the grid points do not line up along the wave front and because the cells become so large near the outer boundary.

\*\* The appropriate parts of DAVID or DAVEJR could be used to greatly reduce the effort required to build a new code.

have a very large grid and would be useful for doing scattering problems even in the absence of any conductivity. DAVID's field equations are differenced in such a way as to allow zero conductivity even now. They could be written to remove the conductivity term and thus be even faster.

General improvements which could be made in DAVID and DAVEJR at this time involve the outer boundary condition and the grid spacing. It would be useful to provide layers of smaller sized cells above and below the ground plane and in the immediate vicinity of the object. Large cells can be used away from those two regions. The outer boundary condition involves both the particles and the electromagnetic field. A 1-D environment calculation could be used to supply the fields and a particle distribution. Only the field boundary condition would be required in DAVEJR, where prescribed sources are used. The present boundary condition, which uses the radial electric field, is described in Section 3.2. As mentioned above, one could use a 2-D environment calculation at the front boundary to include the propagated field, but then one would also have to worry about the scattered field from the object. Other methods should be pursued first.

A carefully considered treatment of electrons emitted from the pole and backscattered from the soil should be implemented. It is very important that such a treatment be consistent with the level of the physics already included so that the proper ratio of currents is maintained.

The DAVID concept should also be used to calculate system responses in the high-altitude burst close-in region, or, to some degree, in the investigation of 3-D effects in the SGEMP problem. There are several problems inherent in the last application which involve the definition of currents near the satellite and the relatively small struts which support the solar panels. It would be very useful to build a simple code which used non-self-consistent prescribed currents or prescribed currents with an approximation for self-consistency.

A listing of DAVID, DAVEJR, and the time waveform output code DAVEOUT can be obtained by qualified users through the Defense Nuclear Agency.

## REFERENCES

1. Hill, J. R., and R. Holland, "POST3D: A Three-Dimensional Self-Consistent Close-In EMP Coupling Code," Mission Research Corporation, Albuquerque, New Mexico, AMRC-R-40, March 1975.
2. Longley, H. J., and C. L. Longmire, "Development of GLANC EMP Code," Los Alamos Nuclear Corporation, Los Alamos, New Mexico, LANC-R-7, DNA 3221T, January 1971.
3. Longmire, C. L., and H. J. Longley, "Improvements in the Treatment of Compton Current and Air Conductivity in EMP Problems," Mission Research Corporation, MRC-N-2, DNA 3192T, October 1975.
4. Evans, R. D., The Atomic Nucleus, McGraw-Hill Book Company, New York, 1955.
5. Longmire, C. L., "Theory of EMP from Nuclear Surface Bursts," Los Alamos Nuclear Corporation, January 1970 (Draft).

## APPENDIX A

### AN APPROXIMATION FOR INCLUDING MAGNETIC TURNING EFFECTS IN PRESCRIBED ELECTRON CURRENTS

Efforts are now being made to perform three-dimensional close-in EMP calculations. In the regions of interest, the electric and magnetic fields are great enough to influence the motion of the Compton electrons, which originally created them. Self-consistent particle following schemes are the best way to calculate these driving currents. However, particle calculations require considerable computer storage and time. This time and storage can often be put to better use, e.g., proving a more accurate system model or generating more detailed parameter studies. A prescribed current calculation can be used to generate a current description at low altitudes. Using this technique, the current is given by the gamma flux times a constant (Reference A-1). The same is true of the ionization rate. It seems reasonable to expect that an approximation should be available which would give a first order correction to the prescribed current to account for the effects of magnetic turning and the electric field drag force. One such technique (Reference A-2), which we will call the "DX-DY" approximation, already exists. It is a good approximation. There is a simpler way to obtain useful estimates, however, a method which can easily be made more accurate after a few parameter studies using particle pushing codes have been made.

The most important self-consistent effect for fields near a surface at sea level is the magnetic turning effect. Compton electrons traveling initially parallel to the ground are turned upward, driving a significant electric field which couples rather efficiently into objects poking

up out of the earth. The normal drag forces more-or-less mask the electric field drag. Therefore, electric field effects will be ignored here, although they could be included with no difficulty. Actually, only one magnetic field component will be considered: the one parallel to the ground and the incident wave front (the x-direction in Figure A-1). This is the component which would exist in the absence of an object and which is normal to the path of the incoming electrons. The current running on a vertical pole will generate an azimuthal field which adds to the ambient field on one side and subtracts from it on the other.

We start with the equation of motion of an electron in a magnetic field, with collisions:

$$\frac{dP_z}{dt} + vP_z = \omega_H P_y, \quad (A-1)$$

$$\frac{dP_y}{dt} + vP_y = -\omega_H P_z, \quad (A-2)$$

where

$$\omega_H = \frac{eB_x}{m\sqrt{1 + (P/mc)^2}}, \quad (A-3)$$

$$v = \frac{A}{P}, \quad (A-4)$$

$$A = \frac{e \times 10^8 \rho}{312} \frac{(E_e + 0.3)^2}{E_e(E_e + 0.6)}, \quad (A-5)$$

$$P = \sqrt{P_y^2 + P_z^2}, \text{ magnitude of momentum}$$

$E_e$  = electron kinetic energy (MeV)

$e$  = electron charge ( $1.602 \times 10^{-19}$  coulomb)

$\rho$  = air density ( $1.23 \text{ kg/m}^3$  at sea level)

$m$  = electron mass ( $9.108 \times 10^{-31} \text{ kg}$ )

$B_x$  = magnetic field intensity (Tesla)

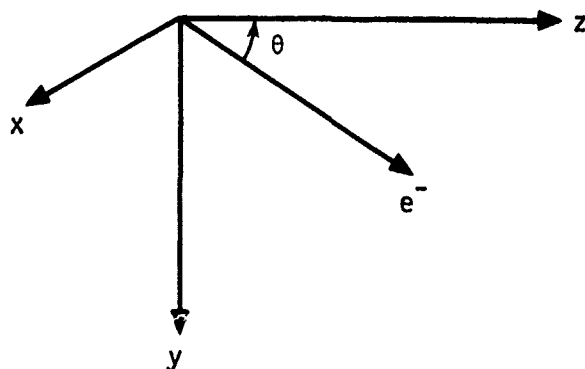


Figure A-1. Problem geometry. Gamma wave front is parallel to x-axis. Wave normal makes angle  $\theta$ , measured from the horizontal.

The quantities  $\nu$  and  $\omega_H$  will be treated as constants. Representative values of  $P$  and  $E_e$  must be used to calculate them directly. They will actually be found from comparison with more accurate calculations as a function of gamma energy.

We define the complex quantity

$$P = P_z + iP_y . \quad (A-6)$$

Equations A-1 and A-2 combine to yield

$$\frac{dP}{dt} + (\nu - i\omega_H)P = 0 , \quad (A-7)$$

which has the solution

$$P = P_0 e^{-\gamma t} , \quad (A-8)$$

where  $\gamma = \nu - i\omega_H$  and  $P_0 = P_{0z} + iP_{0y}$ , the initial momenta. The average value of  $P$  over the time interval  $\Delta t$  is

$$P_A = \frac{P_0}{\gamma \Delta t} (1 - e^{-\gamma \Delta t}) . \quad (A-9)$$

We will be interested in how the average momentum with turning compares to the average momentum without turning, since this will indicate how the currents compare. First, assume that  $\nu \Delta t$  is large, which rids us of the damped oscillation contained within the parentheses. Then, the real and imaginary parts of the modified equation yield

$$P_{az} = \frac{\nu P_{z0} - \omega_H P_{y0}}{(\nu^2 + \omega_H^2) \Delta t} , \quad (A-10)$$

$$P_{ay} = \frac{\nu P_{y0} + \omega_H P_{z0}}{(\nu^2 + \omega_H^2) \Delta t} , \quad (A-11)$$

where  $P_{az}$  and  $P_{ay}$  are the average momentum components. Without turning, these components would be

$$P'_{az} = \frac{P_{z0}}{\nu \Delta t} , \quad (A-12)$$

$$P'_{ay} = \frac{P_{0y}}{\nu \Delta t} . \quad (A-13)$$

Then, in terms of the non-turning momentum,

$$P_{az} = \frac{P'_{az} - \left( \frac{\omega_H}{\nu} \right) P'_{ay}}{1 + \left( \frac{\omega_H}{\nu} \right)^2} , \quad (A-14)$$

$$P_{ay} = \frac{P'_{ay} + \left( \frac{\omega_H}{\nu} \right) P'_{az}}{1 + \left( \frac{\omega_H}{\nu} \right)^2} . \quad (A-15)$$

We now assume for curve-fitting purposes that the primed and unprimed momenta correspond to the standard prescribed current and the modified current. Let  $\vec{J}$  be the prescribed current that would be calculated without a magnetic field, and let  $\vec{J}^{sc}$  be the current calculated with a magnetic field. Then, we propose that they are related in the following manner:

$$J_z^{sc} = \frac{J_z - \left(\frac{\omega_H}{v}\right) J_y}{1 + \left(\frac{\omega_H}{v}\right)^2}, \quad (A-16)$$

$$J_y^{sc} = \frac{J_y + \left(\frac{\omega_H}{v}\right) J_z}{1 + \left(\frac{\omega_H}{v}\right)^2}. \quad (A-17)$$

Note that the self-consistent current depends upon only the ratio  $(\omega_H/v)$ , which can be written as  $(B_x/B_A)$ , i.e.,

$$\frac{\omega_H}{v} \equiv \frac{B_x}{B_A}, \quad (A-18)$$

where  $B_A$  is a function of the electron energy and is proportional to the air density. It has units of magnetic field intensity. It will be fitted as a function of the gamma ray energy.

To simplify the equations, rotate the coordinate axis such that the z-axis is parallel to the direction of the gamma rays. We can then refer to the original prescribed current as  $J$  (it being parallel to the z-axis). The component of the self-consistent current in this direction will be called  $J_p$  and the component turned normal to  $J$  will be called  $J_N$ . Then,

$$\frac{J_p}{J} = \frac{1}{1 + \left(\frac{B_x}{B_A}\right)^2}, \quad (A-19)$$

$$\frac{J_N}{J} = \frac{\left(\frac{B_x}{B_A}\right)}{1 + \left(\frac{B_x}{B_A}\right)^2}, \quad (A-20)$$

$$\frac{J_N}{J_R} = \frac{B_x}{B_A}. \quad (A-21)$$

These ratios were calculated as a function of gamma ray energy (assuming that the Compton electron's initial energy was half the gamma energy) and  $B_x$ . The initial momentum was calculated through

$$P_0 = (mc) \left[ \left( 1 + \frac{E_e}{mc^2} \right)^2 - 1 \right]^{1/2}. \quad (A-22)$$

The drag and turning constants (lumped into  $B_A$ ) were calculated using the initial value of momentum and energy. This leads to smaller values of  $v$  (and  $B_A$ ) than are realistic, but the ratios will still be reasonable. The ratios are shown in Figures A-2, A-3, and A-4 as a function of  $B_x$  and the gamma ray energy. They are compared with the same ratios computed from the DX-DY data published in Reference A-2\*. The agreement is within a factor of two over most of the parameter range. The new results are much smoother, however. This is not an indication that they reflect physical reality any better. Both methods become increasingly inaccurate as the magnetic field increases. The smoother curves generated by the new technique aid in the numerical integration of Maxwell's equations, however.

In order to improve the approximation, we decided to calculate  $B_A$  using Longley's (Reference A-2) DX-DY data, rather than trying to choose an average value of electron momentum or some other such thing. The DX-DY predictions are most accurate at low magnetic fields. Since only one

---

\* Reference A-2 contains data for a wide range of gamma energies, electric fields, and magnetic fields.

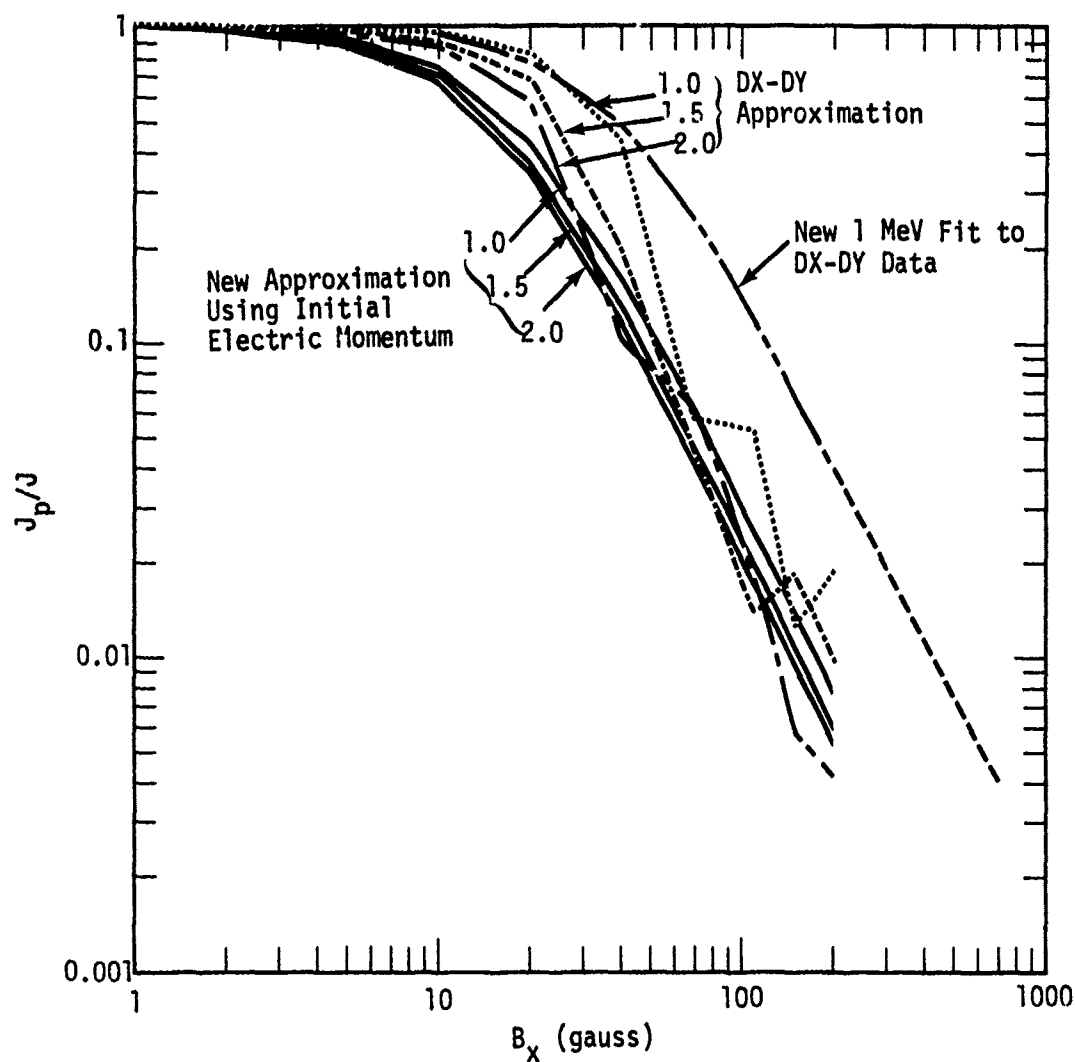


Figure A-2. Ratio  $J_p/J$  as a function of magnetic field intensity for three gamma ray energies (1.0, 1.5, 2.0 MeV). Curves are shown for the DX-DY approximation, the new approximation, and the new approximation fitted to the DX-DY predictions (1 MeV).

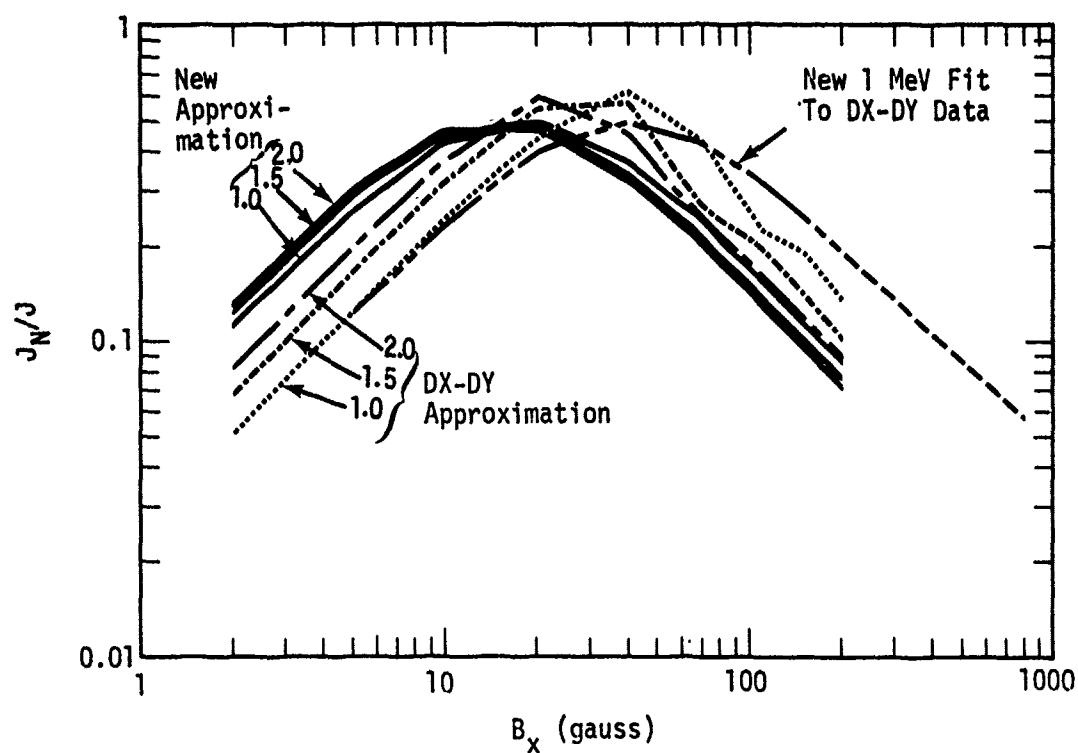


Figure A-3. Ratio  $J_N/J$  as a function of magnetic field intensity and gamma ray energy (1.0, 1.5, and 2.0 MeV). Curves are shown for the DX-DY approximation, the new approximation, and the new approximation fitted to the DX-DY predictions (1 MeV).

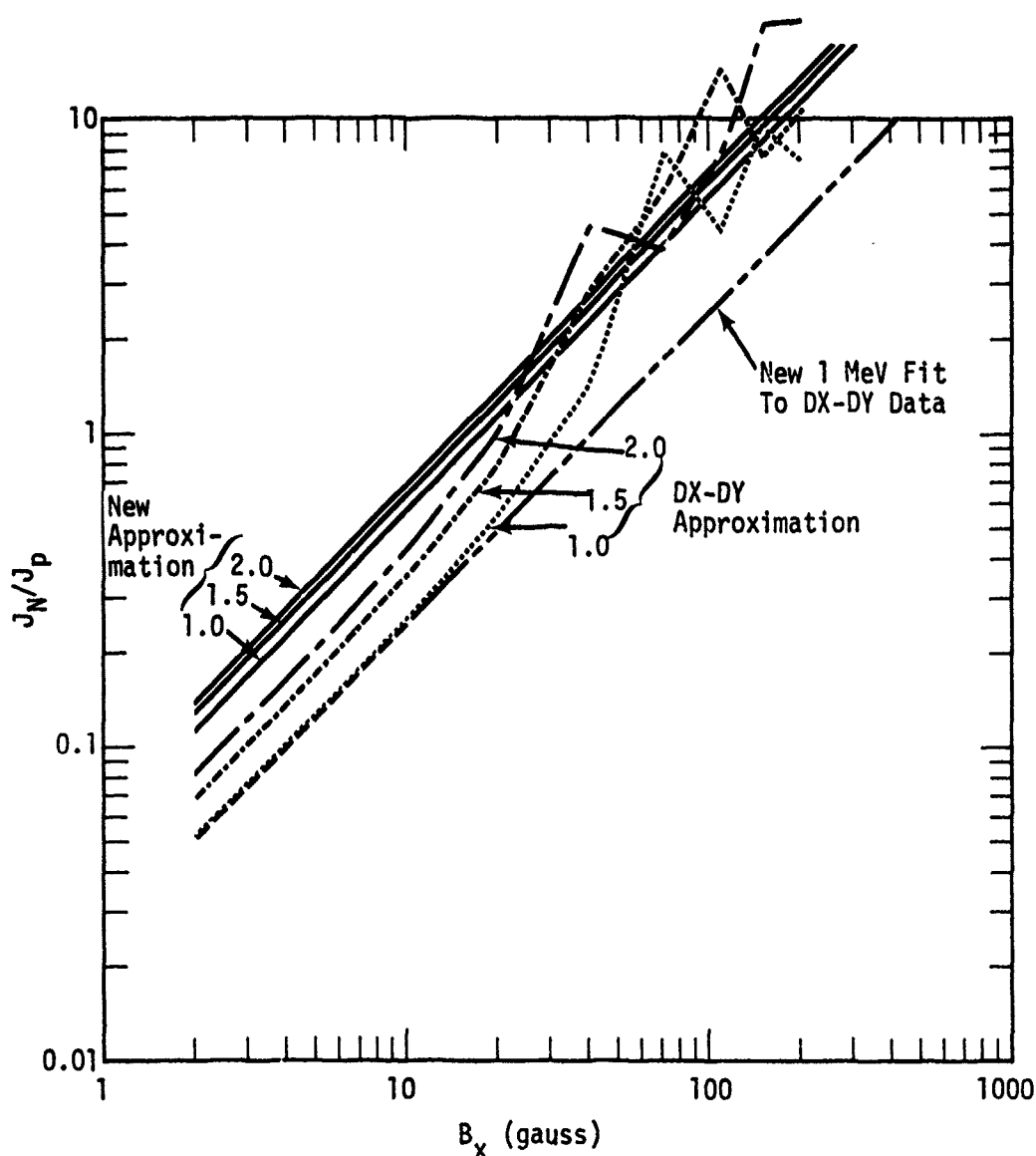


Figure A-4. Ratio  $J_N/J_p$  as a function of magnetic field intensity for three gamma energies (1.0, 1.5, 2.0 MeV). Curves are shown for the DX-DY approximation, the new approximation, and the new approximation fitted to the DX-DY predictions (1 MeV).

parameter,  $B_A$ , is used in the new approximation, it was easy to compute it from the ratios published in Reference A-2 for zero electric field.  $B_A$  is given by Equation A-21. The ratio corresponding to  $J_N/J_P$  in Reference A-2 is  $DY/DX$ . Table A-1 shows the fitted values of  $B_A$  (in gauss) as a function of incident gamma energy,  $E_\gamma$ .  $E_\gamma$  is between 0.5 MeV and 6.0 MeV. Fortunately, a rather simple curve-fit of this data exists. It is

$$B_A(E_\gamma) = \frac{B_0}{\ln(E/E_0)} , \quad 0.5 \leq E_\gamma \leq 6 \text{ MeV} , \quad (\text{A-23})$$

where

$$B_0 = 44.27 \rho_r \text{ (gauss)}$$

$$E_0 = 0.3322 \text{ (MeV)}$$

$$\rho_r = \text{air density, relative to sea level}$$

$$E_\gamma = \text{gamma energy (MeV)}$$

An example of the new fitted calculation is also shown in Figures A-2 through A-4. The example is that of a 1 MeV gamma ray.

In DAVEJR,  $J_N$  and  $J_P$  are calculated using Equations A-19 and A-20 and a coordinate system rotation, when the parameter ISELF is set equal to 1. When ISELF = 0, no self-consistent effects are considered. There is also a smearing of the H-field (HX), which is explained later.

The prescribed current formulation assumes that the electron current is in equilibrium with the gamma flux, i.e., the average Compton collision frequency is high enough to erase any of the electrons memory of previous changes in the gamma flux time history over its lifetime. With turning being added to the current description in the way that it was done here, that assumption is modified by the assumption that the lifetime of the electron is short compared to the time that the magnetic field changes significantly.

Table A-1.  $B_A$  as a function of gamma energy ( $E_\gamma$ ).  
These values are calculated using the  
DX-DY data published in Reference A-2.

$E_\gamma$ (MeV)	$B_A$ (gauss)
0.5	84.00
1.0	40.17
1.5	29.47
2.0	24.66
3.0	20.15
4.0	17.97
5.0	16.65
6.0	15.80

A word of caution must be expressed. When calculating currents near a surface, one must remember that the surface will prevent the complete turning of the electrons and hence will reduce the influence of the magnetic field in changing the prescribed current. The surface effect will increase for increasing incidence angles, but will decrease for increasing magnetic field strengths, since the turning radius of the electron decreases and one can get closer to the surface before electrons collide (see Figure A-5). Obviously, the range of the electron is also important in determining the height at which the ground influence will be felt. To a lesser degree, the angular distribution of the Compton electrons is of interest. At near grasing angles, the fact that Compton electrons are ejected in a cone about the direction of gamma incidence contributes to a small net vertical current. None of these effects have been considered here. A relatively simple height dependence can probably be built into the "constant"  $B_A$  to obtain an estimate of the importance of the surface interaction (which also includes backscattered electrons, another effect that we have ignored).

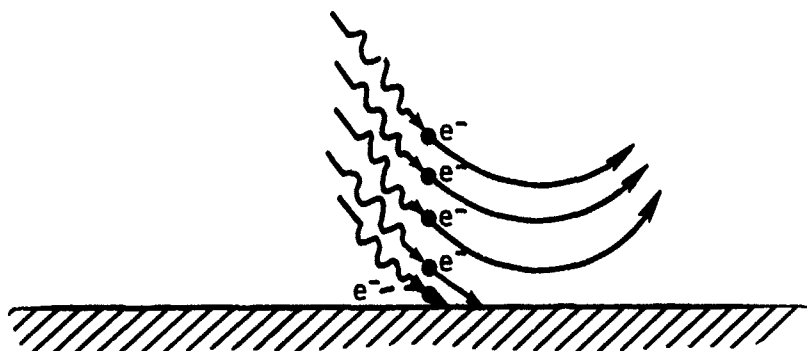


Figure A-5. Effect of a surface on the current components generated by magnetic turning.

A second problem occurs with the use of modified prescribed sources. The approximations assume that the electron sees a constant magnetic field (and electric field, when used) over its lifetime. In sea level air, that time is about 1 shake. Thus, an electron born near the beginning of the pulse can experience a wide range of field strengths over its lifetime.

In DAVEJR, we multiply the HX field by a time-dependent quantity which reduces the effective H-field during the rise of the pulse. At late times, when the magnetic field is presumably varying slowly, the function approaches unity and the prescribed current then reacts to the instantaneous field. The function is called HSMR (H-smear) and is

$$\text{HSMR} = \frac{1 - \text{EXP}(-\text{ATSMR})}{\text{ATSMR}}, \quad (\text{A-24})$$

where

$$\text{ATSMR} = \frac{1}{2} [1 - \text{TANH}(\text{ALPHA} \cdot \text{TSMR})] (\text{ALPHA} \cdot \text{DTSMR}) + 10^{-4}$$

ALPHA = rise e-fold rate of pulse

DTSMR = time over which the magnetic field is to be smeared

TSMR = TS-TPK

TPK = time at which gamma pulse peaks

TS = local time at which source is being calculated.

This is not a true "smearing" of the magnetic field, which would involve a convolution with a memory function or a weighted average. Such techniques involve storing past values or functions of the field. With a three-dimensional code, this requires significant storage. In order to avoid the use of this storage, the method using Equation A-24 was devised.

## REFERENCES

- A-1. Hill, J. R., and R. Holland, "POST3D: A Three-Dimensional Self-Consistent Close-In EMP Coupling Code," Mission Research Corporation, Albuquerque, New Mexico, AMRC-R-40, March 1975.
- A-2. Longley, H. J., and C. L. Longmire, "Development of GLANC EMP Code," Los Alamos Nuclear Corporation, Los Alamos, New Mexico, LANC-R-7, DNA 3221T, January 1971.

## DISTRIBUTION LIST

### DEPARTMENT OF DEFENSE

Director  
Defense Advanced Research Proj. Agency  
ATTN: Technical Library

Defense Documentation Center  
12 cy ATTN: TC

Director  
Defense Nuclear Agency  
ATTN: RAAE  
2 cy ATTN: STTL, Tech. Lib.  
ATTN: STSI, Archives  
ATTN: DDST  
ATTN: RAEV

Commander  
Field Command  
Defense Nuclear Agency  
ATTN: FCPR

Chief  
Livermore Division, Field Command, DNA  
Lawrence Livermore Laboratory  
ATTN: FCPRL

### DEPARTMENT OF THE ARMY

Commander  
Harry Diamond Laboratories  
ATTN: AMXDO-RCC, John E. Thompson  
ATTN: AMXDO-TI, Tech. Lib.  
ATTN: AMXDO-EM, William T. Wyatt, Jr.  
ATTN: AMXDO-EM, John Bombardt

### DEPARTMENT OF THE NAVY

Superintendent  
Naval Postgraduate School  
ATTN: Code 2124, Tech. Reports Librarian

Director  
Naval Research Laboratory  
ATTN: Code 2027, Tech. Lib.

Commander  
Naval Surface Weapons Center  
ATTN: Code WA50, John H. Malloy  
ATTN: Code 223, L. Libello

### DEPARTMENT OF THE AIR FORCE

AF Weapons Laboratory, AFSC  
ATTN: ELP, Carl E. Baum  
ATTN: ELP, William Page  
ATTN: SUL  
ATTN: EL, Lib.

### ENERGY RESEARCH & DEVELOPMENT ADMINISTRATION

University of California  
Lawrence Berkeley Laboratory  
ATTN: Library, Bldg. 50, Rm. 134  
ATTN: Kenneth M. Watson

### ENERGY RESEARCH & DEVELOPMENT ADMINISTRATION (Continued)

University of California  
Lawrence Livermore Laboratory  
ATTN: Terry R. Donich, L-96  
ATTN: Tech. Info. Dept. L-3  
ATTN: Hans Kruger, L-96  
ATTN: Louis F. Wouters, L-48

Los Alamos Scientific Laboratory  
ATTN: Doc. Con. for John S. Malik  
ATTN: Doc. Con. for Reports Lib.

Sandia Laboratories  
ATTN: Doc. Con. for Charles N. Vittitoe

### DEPARTMENT OF DEFENSE CONTRACTORS

Brown Engineering Company, Inc.  
ATTN: John M. McSwain, M.S. 18  
ATTN: Tech. Lib., M.S. 12, P. Shelton

The Dikewood Corporation  
ATTN: Tech. Lib.

General Electric Company  
TEMPO-Center for Advanced Studies  
ATTN: DASIAC

General Research Corporation  
ATTN: Tech. Info. Office

Intelcom Rad Tech  
ATTN: Tech. Lib.

Kaman Sciences Corporation  
ATTN: Lib.  
ATTN: W. Foster Rich  
ATTN: Walter E. Ware

Mission Research Corporation  
ATTN: William C. Hart  
5 cy ATTN: Tech. Lib.  
ATTN: Conrad L. Longmire  
ATTN: Daniel F. Higgins  
ATTN: Michael A. Messier  
ATTN: Robert M. Hamilton  
ATTN: Kenneth S. Smith

Mission Research Corporation  
ATTN: Tech. Lib.

R & D Associates  
ATTN: Gerald K. Schlegel  
ATTN: Richard R. Schaefer  
ATTN: William J. Karzas  
ATTN: Leonard Schlessinger  
ATTN: Tech. Lib.  
ATTN: Charles Mo

The Rand Corporation  
ATTN: Tech. Lib.

DEPARTMENT OF DEFENSE CONTRACTORS (Continued)

Science Applications, Inc.

ATTN: R. Parkinson

ATTN: Richard L. Knight

ATTN: J. Roger Hill

Systems, Science and Software, Inc.

ATTN: Andrew R. Wilson

ATTN: Technical Library

DEPARTMENT OF DEFENSE CONTRACTORS (Continued)

TRW Systems Group

ATTN: Fred N. Holmquist, M.S. R1-2028

Vector Research Associates

ATTN: W. A. Radasky